**University of Bath**

**PHD**

# Simulations of dye-sensitized solar cells

Maluta, Eric

*Award date:*
2010

*Awarding institution:*
University of Bath

Link to publication

## Alternative formats
If you require this document in an alternative format, please contact:
openaccess@bath.ac.uk

Copyright of this thesis rests with the author. Access is subject to the above licence, if given. If no licence is specified above, original content in this thesis is licensed under the terms of the Creative Commons Attribution-NonCommercial 4.0 International (CC BY-NC-ND 4.0) Licence (https://creativecommons.org/licenses/by-nc-nd/4.0/). Any third-party copyright material present remains the property of its respective owner(s) and is licensed under its existing terms.

**Take down policy**
If you consider content within Bath's Research Portal to be in breach of UK law, please contact: openaccess@bath.ac.uk with the details. Your claim will be investigated and, where appropriate, the item will be removed from public view as soon as possible.

Download date: 05. May. 2023

# SIMULATIONS OF DYE-SENSITIZED SOLAR CELLS

Submitted by Eric N. Maluta
for the degree of
Doctor of Philosophy
University of Bath
Department of Physics
December 2010

COPYRIGHT

Attention is drawn to the fact that copyright of this thesis rests with its author. This copy of the thesis has been supplied on condition that anyone who consults it is understood to recognise that its copyright rests with its author and no information derived from it may be published without the prior written consent of the author.

This thesis may be made available for consultation within the University library and may be photocopied or lent to other libraries for the purposes of consultation.

**Abstract**

Dye sensitized solar cells (DSSCs) are a novel design of solar cell which could be used as power producing windows or skylights. These nanocrystalline solar cells are currently the subject of intense research in the field of renewable energy as a low-cost photovoltaic device. The light adsorption occurs in dye molecules adsorbed on a highly porous structure of $TiO_2$ porous film. The photo-conversion efficiencies of the DSSCs have been recently reported to reach 11%.

Despite the progress in the efficiency and stability of these solar cells there are many fundamental aspects of their operation that are still unknown. One process, for which there is limited information, is the time taken to upload the dye on the $TiO_2$ nanoporous film. Dye is adsorbed onto a $TiO_2$ working electrode by dipping it into the dye solution for periods of several hours to several days. However, such long dipping times are not economic for industrial production of DSSCs. It has been shown recently that the time taken for dye uptake on the solar cell has an impact on its efficiency. The factors controlling this process are not yet fully understood. We develop a model based on the Langmuir isotherms to study and understand the diffusion and adsorption of the dye molecules in $TiO_2$ nanotube films and compare our theoretical results to the experimental results. Our modelling results show that the adsorption of dye into the $TiO_2$ nanotubes is controlled by the diffusion coefficient, the adsorption-desorption ratio and the initial dye concentration.

The competition between the electron transport to the anode and the electron transfer to $I_3^-$ ions in the electrolyte determines the efficiency of the collection of photoinjected electrons. The important parameter in this process is the electron diffusion length $L_n$, which is determined by the effective electron diffusion coefficient and life time. Efficient cells are characterized by a value of $L_n$ that considerably exceeds the $TiO_2$ film thickness. We introduce a new reliable and efficient approach to estimate the electron diffusion length in dye sensitized solar cells. This approach is based on the multiple trapping model which involves calculating the effective electron diffusion coefficient $D_n$ and life time $\tau_n$ at the same quasi Fermi level. We show that in this context $L_n = \sqrt{D_n \tau_n} = L_0$, where $L_n$ and $L_0$ are the effective and free electron diffusion length respectively. $D_n$ and $\tau_n$ are used to interpret the experimental intensity modulated photocurrent and photovoltage spectroscopic data. The good agreement between theory and experiment demonstrates that our model provides a powerful approach to estimate the diffusion length in terms of realistic devices.

The microwave technique is now a well established tool for contactless measurements of charge carriers in semiconductors. A 3D simulation model was developed for the study of photogenerated charge carriers by microwave reflectance techniques in DSSCs. This model is able to reproduce several features of the experimental results, and suggests that the microwave technique is a good measure of photoconductivity.

**Acknowledgments**

I would like to thank my supervisor, Professor Alison Walker, for her guidance over the last three years. The project would not have been possible without her patience, broad knowledge and willingness to answer questions. Special thanks to Laurie Peter for useful discussions concerning experimental issues.

I would also like to thank the rest of the Device Modelling group, past and present, for their help, support and friendship. Special thanks to Theodoros Papadopoulos and Stephen Bingham for interesting scientific discussions on different aspects of physics and Jonny Williams for the introduction sessions to Comsol software. Without the efforts of Adrian Hooper to get the the Comsol software working appropriately even when I used to crash the server, this work was not going to be possible. Collaborators in this work are members of DSSCs group under Laurie Peter, Department of Chemistry, University of Bath. Special thanks to the following group members, Halina Dunn, Hongxia Wang and Alberto Fatori, who have performed the experiments.

Financial support from Ford Foundation International Fellowship Program is highly appreciated.

I am grateful to my parents (Malindi and Phophi) and the rest of Maluta Family, for their moral support throughout my studies and above all thank to the Almighty God for making me to reach this far.

Finally I would like to appreciate the help from Stephen Bingham and Douglas Ashton for proof reading my thesis manuscript.

**Declaration of the input of work done by others**

All of the work described in this thesis was carried out by the author apart from the following:

The chapter reported as electron diffusion length in DSSCs, has been approached using the Fortran program developed by Alison Walker, who has done almost all the coding as it has been developed for some time in the group and I have done a little of the coding for the present results calculations.

The other two chapters have been approached using the Comsol Multiphysics software package, which is an available modeling tool in our device modeling group. A manual was developed by Jonny Williams, which described some of the model settings.

The study of photo-generated charge carriers density in DSSCs work was done with the help of Stephen Bingham, who provided advice on waveguide modelling, which was used as a stepping stone for the development of 2D and 3D Comsol model.

All the experimental results were supplied by Laurie Peter, DSSCs group, Chemistry, University of Bath.

# Contents

# Chapter 1

# Introduction

## 1.1 Introduction to Photovoltaics

Fossil fuels are running out and are held responsible for the increased concentration of carbon dioxide in the earth's atmosphere. Hence, developing environmentally friendly, renewable energy is one of the challenges to society in the 21st century. One of the renewable energy technologies is photovoltaics (PV), the technology that directly converts light into electricity [1]. PV is one of the fastest growing of all the renewable energy technologies, in fact, it is one of the fastest growing industries at present.

The sun, our own star, is responsible for most physical and biological processes of earth. Thus energy from the sun reaching the earth drives almost every known physical and biological cycle in the earth's system. The sun is the source of energy needed for photosynthesis and hence, all forms of life. The energy given off by the sun reaches the earth in the form of electromagnetic radiation, all of which can be collected to produce power [2, 3]. Thus all renewable energy is powered by a steady flux of energy from the sun [4].

Currently the conventional p-n junction based silicon solar cells are expensive for reasons such as highly expensive materials and production methods. Less expensive types of solar cells are at the cutting edge of green energy research. One particular type of these cells is dye sensitized solar cells (DSSCs), which work on the separation processes of light absorption and charge separation. Dye-sensitized solar cells are currently subjects of intense research in renewable energy technologies. They are attracting attention as a promising approach towards energy crisis due to their low-cost compared to traditional silicon solar cells. The device consists of a porous nanocrystalline ti-

tanium dioxide ($TiO_2$) film onto which a photoactive dye is adsorbed. The added advantage of these cells is the availability and non toxicity of the main components, i.e., $TiO_2$, which is used in paints, cosmetic and health care products [5]. The structure of the nanoporous $TiO_2$ film yields a high surface area which can accommodate a large amount of sensitizing dye and in turn increase photocurrent generation [6].

In the 1990s a major photoelectrochemical solar cell development was obtained with the introduction of thin film dye sensitized solar cells devised by Grätzel and O'Regan [7]. For the first time a solar energy device operating on a molecular level showed the stability and the efficiency required for potential practical applications [8]. Although the general principles of dye sensitization of wide band-gap semiconductors were already well established in the 1970s, progress in the application of such techniques to light energy conversion had been initially very slow due to the limited light absorption shown by monolayers of dyes on electrodes of low surface roughness. Substantial advances in conversion efficiencies, obtained with sensitized semiconductor electrodes, started with the development of high surface area nanocrystalline semiconductors and of suitable molecular sensitizers [8].

Until recently, photovoltaic devices were predominantly made from silicon (Si) crystalline element requiring high purity and high temperatures in fabrication. However in the last 20 years there has been increased interest in organic solar cells like dye sensitized solar cells (DSSC), polymer solar cells, etc. This work is concerned with the modelling of the dye sensitized solar cells. The models are solved using a Finite Element method based on Comsol Multiphysics software, which solves the relevant continuity equations, subject to appropriate boundary conditions.

## 1.2 Photovoltaics

Photovoltaics is the process of converting light into electricity [1]. When sunlight is absorbed by a solar cell, the solar energy knocks electrons from its ground state to an excited state, allowing the electrons to flow through the solar cell to produce electricity [2, 3, 9, 10]. A functional photovoltaic scheme should implement at least the following steps:

1. Light harvesting: Light is absorbed and its energy is used to excite electrons
2. Selective charge transport or extraction: Electrons/holes are transported to the terminals of the device, where the high energy electrons are selectively extracted at one terminal, while the holes are replenished from the other terminal.

## 1.3 Environmental impacts of using Photovoltaics

Every energy generation and transmission method affects the environment. Conventional generating options can damage air, climate, water, land and wildlife, landscape, as well as raise the levels of harmful radiation. On a global scale this will cause a build-up of greenhouse gases like, carbon monoxide, in the atmosphere, and increase the danger of climate change and global warming. The environmental damage by energy production has been known for sometime and the assessment of this damage is becoming an issue of ever-increasing importance [10]. It is therefore essential that environmental aspects of solar technologies be considered. Renewable technologies are substantially safer offering a solution to many environmental and social problems associated with fossil and nuclear fuels. Solar energy technologies (SETs) provide obvious environmental advantages in comparison to the conventional energy sources, thus contributing to the sustainable development of human activities [11, 12]. Not counting the depletion of the exhausted natural resources, their main advantage is related to the reduced $CO_2$ emissions and, normally, absence of any air emissions or waste products during their operation. Concerning the environment, the use of SETs has additional positive implications such as [11]:

1. Reduction of the emissions of greenhouse gases.
2. Reduction of the required transmission lines of the electricity grids
3. Improvement of the quality of water resources

In regards to socio-economic viewpoint, the benefits of exploitation of SETs comprises:

1. Increase of the regional/national energy independence
2. Provision of significant work opportunities.
3. Support of the deregulation of energy markets
4. Acceleration of the rural electrification in developing countries

### 1.3.1 Theoretical consideration of Photovoltaics

The basic property of semiconductors, which makes them suitable for photovoltaic applications, is their energy band structure. The valence band of any semiconductor

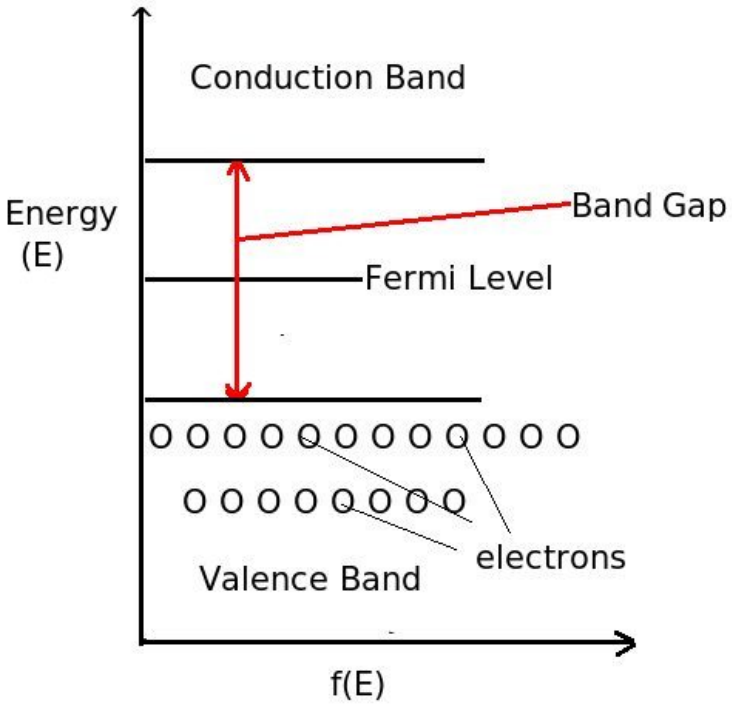


Figure 1.1: Illustrations of the Fermi level of the semiconductors.

is fully occupied at low temperature, while the conduction band is empty. The Fermi Level ($E_{Fn}$) relates the probable location of electrons in a band diagram. As illustrated in figure 1.1, semiconductors are unique because the Fermi Level lies in the band gap which cannot contain electrons. This does not prevent the statistical location of the Fermi Level lying in the band gap. However, at room temperature the thermal motion of electrons can excite some electrons to conduction band. The probability of occupation of the state of energy E is given by Fermi-Dirac distribution [2, 3, 9, 10]:

$$f(E) = \frac{1}{1 + e^{\frac{(E-E_F)}{k_B T}}} \approx \theta(E - E_F) \ , T \to 0 \tag{1.1}$$

where $f(E)$ is the occupation probability, $E_F$ is the Fermi-level energy, $k_B$ is Boltzmann constant, $T$ is the temperature and $\theta$ is a step function, i.e. $\theta = 1$ if $x > 0$, $\theta = 0$ if $x < 0$. At $T = 0$K, the probability of occupation is equal to one for energy less than the Fermi energy ($E < E_F$) and zero for $E > E_F$, as there is no occupation above the Fermi level, which is consistent with the Pauli exclusion principle, which states that no two electrons in a solid can have identical energy states. At $T > 0$, the occupation probability is reduced with increasing energy. The density of states $g(E)dE$ is the number of states per volume at energies $E$ to $E + dE$.

In semiconductors and insulators, electrons are confined to a number of bands of energy and forbidden from other regions. The term band gap refers to the energy difference

between the top of the valence band and the bottom of the conduction band; electrons are able to jump from one band to another. In order for an electron to jump from a valence band to a conduction band, it requires a specific amount of energy for the transition. Electrons can gain enough energy to jump to the conduction band by absorbing light energy [2, 9, 10].

The total electron concentration in a material can be calculated as,

$$n = \int_0^\infty f(E)g(E)dE \tag{1.2}$$

### 1.3.2 Solar cell characteristics

The performance of different solar cell's or module's power are characterized at the standard test conditions (STC). These conditions define performance at an incident sunlight of 1000 $\mathrm{Wm}^{-2}$, a cell temperature of 25 $^0$C and Air Mass (AM) of 1.5 spectrum [9, 13]. The air mass determines the radiation impact and the spectral combination of the light arriving on the earth's surface. In space the air mass reference spectrum is zero (AM 0) for the use by the aerospace community. This spectral irradiance is based on data from satellites, space shuttle missions, high altitude aircraft, etc. Near the equator the reference air mass is one (AM 1). The way in which photovoltaic current-voltage (I-V) characteristics are usually presented is seen in figure 1.2. This figure shows important factors affecting solar cell performance, such as the maximum power point, which is the point where the product of the current and voltage are maximum.

The work done by a solar cell per unit time is quantified as its output power (P), which is given by,

$$P = JV \tag{1.3}$$

where J is the current flowing out of the cell and V is the voltage across the cell.

The four most important factors used to characterize the solar cell are, open circuit voltage ($V_{oc}$), short circuit current density ($J_{sc}$), fill factor (FF) and the efficiency ($\eta$) [1, 2, 3, 9]. The $V_{oc}$ is defined as the voltage between the terminals when there is no current flowing (infinite load resistance) and the $J_{sc}$ is defined as the current when the terminals are connected to each other (zero load resistance). The fill factor is defined as,

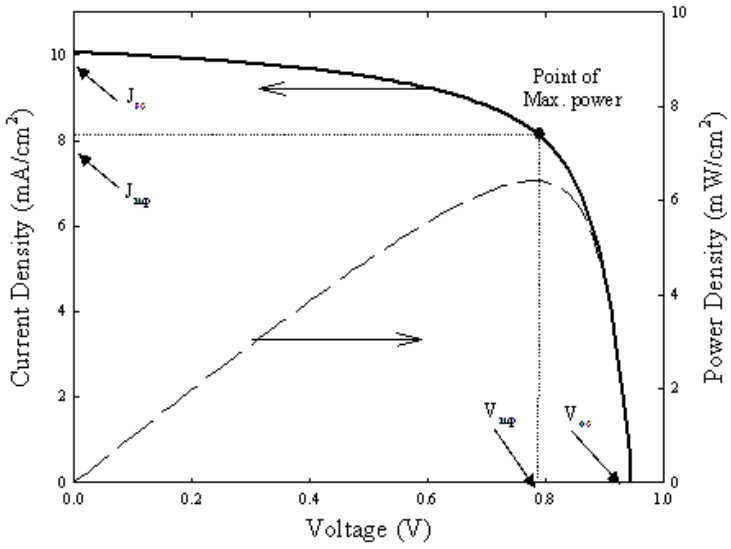


Figure 1.2: The current - voltage characteristics of a solar cell under illumination

$$FF = \frac{J_{mp}V_{mp}}{J_{sc}V_{oc}}, \tag{1.4}$$

where $J_m$ and $V_m$ are the current and voltage respectively, at the maximum power point ($P_m$) on the curve as shown on figure 1.2. The power efficiency, $\eta$ is defined as [2, 3, 9],

$$\eta = \frac{J_{sc}V_{oc}FF}{P_s}, \tag{1.5}$$

where $P_s$ is the incident light power density.

When a load is connected to a solar cell a potential difference develops between the terminals of the cell. A solar cell can be treated as a diode. For an ideal diode the dark current density ($J_{dark}$) is given by [1, 9],

$$J_{dark} = J_0(e^{\frac{qV}{k_BT}} - 1) \tag{1.6}$$

where $J_0$ is the reverse bias saturation current density, q is the electron charge and V is the voltage across the terminals.

The net current density (J) can be approximated by the difference between the short circuit current density ($J_{sc}$) and dark current density ($J_{dark}$) given by,

$$J = J_{sc} - J_{dark} = J_{sc} - J_0(e^{\frac{qV}{k_B T}} - 1) \tag{1.7}$$

At open circuit condition, $J_{dark} = J_{sc}$ so the open circuit voltage ($V_{oc}$) is given by,

$$V_{oc} = \frac{k_B T}{q} \ln(\frac{J_{sc}}{J_0} + 1) \tag{1.8}$$

Equation 1.8 shows that $V_{oc}$ increases logarithmically with the light intensity, assuming that $J_{sc}$ increases linearly with light intensity.

## 1.4 Conventional solar cells

The current status of PV is that it hardly contributes to the energy market, because it is too expensive. The large production costs for the silicon solar cells is one of the major obstacles. Even if the production costs could be reduced, large-scale production of the current silicon solar cells would be limited by the high technology needed. To ensure a sustainable technology path for PV, efforts to reduce the costs of the current silicon technology need to be balanced with measures to create and sustain variety in PV technology. It is clear that new solar cell technologies are necessary. In the field of inorganic thin-films, technologies based on cheaper production processes are currently under investigation.

The key to making a photovoltaic device is not only to absorb light of a suitable wavelength, but also to extract the promoted electrons, by building in some form of asymmetry. Silicon solar cells, which remain the most widespread photovoltaic devices, are made up of a thick (300$\mu$m) base layer of p-type silicon, and an emitter layer, 0.3 $\mu$m of n-type silicon. The emitter layer is created on the surface of the p-type base by doping with donor impurities (e.g.phosphorus). Doping is the process whereby a small number of impurity atoms replace some of the silicon atoms in the crystal [2]. For example the n-type and p-type semiconductor can be achieved by doping silicon with phosphorus and boron respectively. By adding the phosphorus with 5 valence electrons we achieve an electron donor, while by adding the boron with 3 valence electrons we achieve an electron acceptor as silicon has 4 valence electrons. When these two types of semiconductor are brought into contact, they form a p-n junction.

Upon illumination of the p-n junction photons are absorbed by excitation of electrons from the valence band to the conduction band leaving holes to the valence band. Due

to the high crystallinity of the semiconductor, which is essential for good operation, the electrons and holes are more or less free to move in the material by drift due to potential gradients and by diffusion due to concentration gradients.

The existence of the built-in electric field in the p-n junction region is the source of photovoltaic activity in the cell. Under illumination, a large number of electrons and holes are generated in the semiconductor material. Minority charge carriers generated in the depletion region of the p-n junction, or within their diffusion length from it, are swept to the opposite side of the junction by the built-in electric field of the junction. Under illumination, electrons are therefore accumulated in the n-type material and holes in the p-type material, generating voltage between the opposite sides of the p-n junction and electrical contacts attached to them, as well as current through an external load attached between the contacts.

## 1.5 Excitonic solar cells

Recently a new class of photovoltaics technologies has emerged in which the process of generating free charge carrier pairs is fundamentally different to that of the conventional p-n junction solar cells. These cells are called excitonic because the initial light absorption step leads to the generation of the bound electron-hole pairs, or excitons, rather than free charge carriers [13, 14]. The excitons must then dissociate at the interface before electrons and holes are free to be collected. This contrasts with conventional p-n junction cells where free carrier pairs are generated immediately upon light absorption because of electron-hole binding energies which are less than the thermal energy. The role of the heterojunction in a conventional solar cell is purely to separate free carriers rather than to dissociate bound charge pairs as it is in an excitonic cell. There are two main classes of excitonic cells currently being researched:

- Polymer or Blend solar cells
- Dye Sensitized solar cells

Polymer solar cells consist of a mixture of light-absorbing electron and hole conducting polymers. Upon light absorption excitons are generated through the bulk of one of the polymers and these excitons diffuse to the interface before being separated. It is important that the exciton lifetime is long enough so that it can reach the interface before recombination. It is convenient to define an exciton diffusion length which is a measure of how far an exciton can diffuse before recombining; a key requisite for

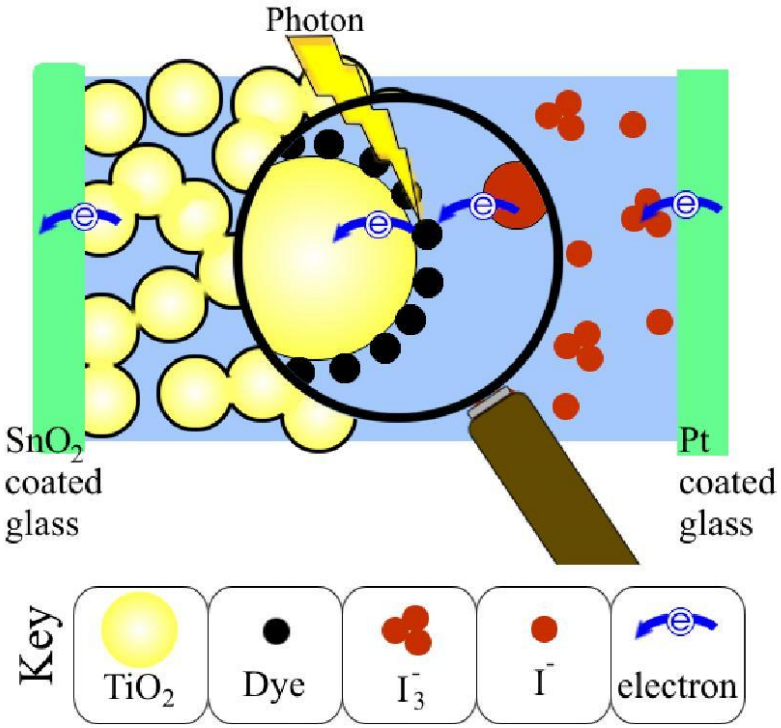


Figure 1.3: The arrangement of components of dye sensitized solar cell, image from [15]

an efficient polymer blend cell is that the exciton diffusion length is greater than the average distance an exciton must travel before finding an interface.

On the other hand the DSSCs are also based upon a large area heterojunction which usually consists of an n-type semiconductor titanium dioxide ($TiO_2$) and a redox electrolyte or organic hole conductor. The dye molecules are adsorbed on the surface of the $TiO_2$ film, which act as the light absorbing components of the cell. The dye molecules are at the interface between the two phases, the semiconductor $TiO_2$ as electron conductor and the organic hole conductor (electrolyte). In contrasts to polymer solar cells the exciton generation in dye sensitized solar cells occurs at the interfaces [14], as it is where the layer of the dye molecules is adsorbed. Upon light absorption by the dye molecules, an electron is injected into the $TiO_2$ layer. This injection is followed by the rapid regeneration of dye by the electrolyte or rapid hole transfer to the hole conductor. The concept of exciton diffusion length is not relevant as the exciton is generated within the interface, but the distance which the free electron travels before recombination is an important parameter to define the efficiency of the solar cells. This parameter is defined as the electron diffusion length, which is one of the main topics discussed in this work.

## 1.6 Dye sensitized solar cells

Dye sensitized solar cells are made up of numerous layers as shown in figure 1.3, a conductive support, a collector electrode ($TiO_2$ semiconductor), a sensitizing dye, an electrolyte solution and a catalyst coated counter electrode. The collector electrode in the cell comprises of nanocrystalline $TiO_2$ wide band-gap semiconductor. A ruthenium complex-dye is chemically adsorbed onto the semiconductor film. The counter electrode is made up of a catalyst (usually platinum) attached to another piece of conducting glass. A redox pair consisting of iodide ($I^-$) and tri-iodide ($I_3^-$) acts as an electrolyte in the cell. The light adsorbed by the dye produces a current through the cell, which then results in the production of electricity [5, 6, 16].

Even when the energy conversion efficiency of the cells has not yet reached the level of silicon solar cells, the dye sensitized solar cells are extremely promising because they are made of low-cost materials and do not need elaborate apparatus to manufacture [7, 17, 18]. If conversion efficiency and device durability can be engineered to meet the requirements for volume applications, these technologies may in the future be instrumental in bringing up the proportion of power generated by direct conversion from sunlight. The DSSCs have a simple structure that consists of two electrodes and an iodide-containing electrolyte. One electrode is dye-absorbed highly porous titanium dioxide ($TiO_2$) film deposited on a transparent electrically conducting substrate. The other is a transparent electrically conducting substrate only. The cells have been compared to photosynthesis because they use the redox reaction of the electrolyte [7].

### 1.6.1 Incident photon-to-current conversion efficiency in DSSCs

The incident photon-to-current conversion efficiency (IPCE) or quantum efficiency is defined as the ratio of the number of charge carriers collected by the solar cell to the number of photons of a given energy shining on the solar cell, that is,

$$IPCE = \frac{J_n}{I_0} \tag{1.9}$$

where $J_n$ is the flux of the electrons out of the device and $I_0$ is the flux of photons incident on the device. IPCE therefore relates the response of a solar cell to the various wavelengths in the spectrum of light shining on the cell. The IPCE measurements are critical to understand the conversion efficiency of the solar cell as a function of the wavelength of light striking on the cell. As illustrated in figure 1.4 the IPCE of the DSSCs can be defined as the product of the three processes happening during the light

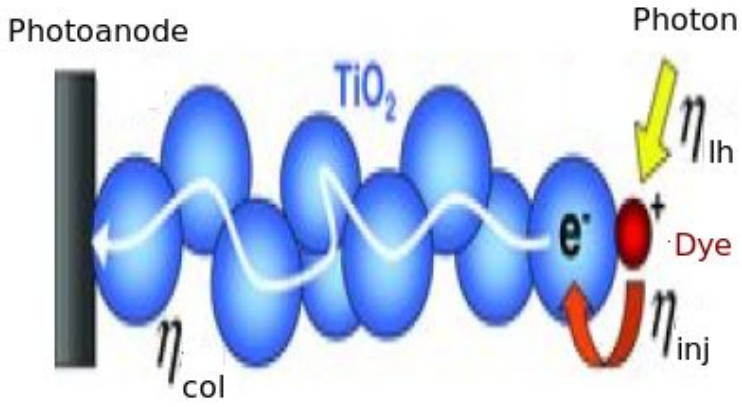


Figure 1.4: Illustrates the light harvesting efficiency ($\eta_{lh}$), electron injection efficiency ($\eta_{inj}$) and electron collection efficiency ($\eta_{col}$), image taken from [21].

absorption process given by [19, 20, 21],

$$IPCE(\lambda) = \eta_{lh}(\lambda)\eta_{inj}(\lambda)\eta_{col}(\lambda) \tag{1.10}$$

where $\eta_{lh}(\lambda)$ is the light harvesting efficiency of the sensitized $TiO_2$, $\eta_{inj}(\lambda)$ is the efficiency of the electron injection from the sensitizers into the $TiO_2$ and $\eta_{col}(\lambda)$ is the electron collection efficiency. $\eta_{lh}(\lambda)$ is determined by the $TiO_2$ layer thickness (d), the absorption coefficient ($\alpha(\lambda)$) of the sensitized $TiO_2$, which is especially determined by the dye molecules attached to the $TiO_2$ porous film.

The most efficient DSSCs typically have injection and collection efficiencies of close to unity and in this case the IPCE is simply equal to the light harvesting efficiency, which can be expressed as [20, 22],

$$\eta_{lh}(\lambda) = 1 - e^{(-\alpha(\lambda)d)} \tag{1.11}$$

The light harvesting efficiency now assumes Beer-Lambert law. While still an important quantity, the IPCE alone cannot be used to predict the overall efficiency of a device even if $\eta_{col}$ and $\eta_{inj}$ are known. This is because the current flowing out of the device is only one of the two parameters determining the power output. In order to understand the origin of the power output the voltage across the cell must also be considered.

### 1.6.2 Photosensitizer or Dye

Dye molecules adsorbed on the $TiO_2$ porous or nanotube film surface serve as the photon absorber in DSSCs, whose properties have a significant effect on the light harvesting efficiency and the overall photoelectric conversion efficiency. The ideal dye sensitizer should absorb all light below a threshold wavelength of about 920nm. In addition, it should be firmly grafted to the $TiO_2$ semiconductor surface and inject electrons to the conduction band [23, 24, 25, 26]. Its redox potential should be sufficiently high so that it can be regenerated rapidly via electron donation from the electrolyte or hole conductor. It should be stable enough to sustain at least $10^8$ redox turn overs under illumination corresponding to about 20 years of exposure to natural light. The best photovoltaic performance in terms of both conversion yield and long term stability has so far been achieved with polypyridyl complexes of ruthenium and osmium dye [24].

### 1.6.3 The electrolyte

The electrolyte is any substance that contains free ions, which behaves as an electrically conductive medium. The redox couple in the electrolyte is of crucial importance for stable operation of DSSCs, because it must carry the charge between the photoelectrode and the counter-electrode for regeneration of the dye. After electron injection, the electron donor in the electrolyte must reduce the oxidized dye to the ground state as rapidly as possible. Thus the choice of this charge mediator should take into account its redox potential, which must be suitable for regenerating the dye. The redox couple must be fully reversible and should not exhibit significant absorption of visible light. Another important requirement is related to the solvent, which should permit the rapid diffusion of charge carriers, while not causing the desorption of the dye from the $TiO_2$ film surface [27].

The record conversion efficiencies of 11% [24, 28] reported, are typically achieved with liquid electrolyte based on acetonitrile, a low viscosity volatile solvent and by using comparatively low iodine concentration. These high efficiency electrolytes are not at the same time optimized for achieving the best long-term stability characteristic, for which other electrolyte formulations with less volatile solvents or ionic liquids as well as higher iodine concentration are more appropriate [24, 27, 28]. The properties of the redox couple in the electrolyte can influence the reduction of the oxidized state of the dye as well as several other processes in the DSSCs, including electron transfer kinetics at the counter electrode and charge transport in the semiconductor film solution [28, 27].

## 1.7 Overview of the thesis

This thesis is concerned about the simulation of dye sensitized solar cells with respect to different processes, like dye uptake, electron transport, etc. The main aim is to understand those process towards the improvement of the efficiency. The thesis is divided into different chapters with different section as follows,

### 1.7.1 Chapter two

In this chapter, the work is based on the study of the dye adsorption on the $TiO_2$ nanotubes film. The factors controlling the dye uptake process are discussed. Our simulation results are compared to the experimental dye uptake results.

### 1.7.2 Chapter three

The focus of this chapter is to study the electron transport and hence to show that, in the multiple trapping model, the effective electron diffusion length is approximately equal to free electron diffusion length provided the difference between the open and short circuit quasi Fermi levels is taken into account. Electron transport at short circuit has been explained by the effective diffusion coefficient, and electron recombination at open circuit has been explained using the effective electron life time. To illustrate the importance of the transient time ($\tau_{tr}$) and the electron lifetime ($\tau_n$), the near infrared responses measured experimentally were reproduced theoretically to demonstrate that even when they are measured under the same incident light intensity they are different. A further step has been taken to discuss the dependence of electron diffusion length on the thickness of the cell. Our simulation results are validated by comparing them with the experimental results.

### 1.7.3 Chapter four

This chapter discuss the study of photo generated charge carriers in DSSCs by microwave reflectance techniques. The behaviour of photoconductivity is discussed, using the relationship between the photoconductivity and the photomodulated reflectivity. The simulation results of the reflection coefficient as a function of device structure and material properties are presented and the results of the photomodulated reflectivity are extracted by calculating the difference between the reflection coefficient in the

dark and under illumination. Ultimately our simulation results are compared to the experimental results.

### 1.7.4 Chapter five

The overview of all the chapters is given and future work from the findings of the above three chapters is discussed.

# Chapter 2

# Dye Uptake in Dye Sensitized $TiO_2$ Nanotube based Solar Cells

## 2.1 Introduction

In this chapter, Comsol Multiphysics software has been employed to study the dye uptake in dye sensitized $TiO_2$ nanotube based solar cells. The main aim is to understand the factor controlling the dye uptake processes, as currently the procedure followed for dye adsorption into the $TiO_2$ films is dipping it into the dye solution for several hours or days.

The light harvesting components in dye sensitized solar cells (DSSCs) are the dye molecules attached on the surface area of the $TiO_2$ film. The large surface area of the $TiO_2$ film is one of the factors which enables efficient light harvesting, maximizing the amount of photogenerated charge and allows the attachment of efficient dye molecules [29]. Currently $TiO_2$ nanotube films are taken into consideration as they offer an attractive alternative to porous films, because they combine high surface area with a well-defined pore geometry [29, 30, 31, 32]. The vertical pore geometry of the nanotubes appears to be more suitable than the $TiO_2$ film random pore network and it has been reported that nanotube films give a better electron transport and improved collection efficiencies compared to $TiO_2$ films of the same thickness [33]. The arrangement of the highly ordered titania nanotube array perpendicular to the surface permits directed charge transfer along the length of the nanotubes from solution to the conductive substrate, thereby reducing the losses incurred by charge hopping across the nanoparticle grain boundaries [30]. Easier access to the nanotube array surface, as well as better control of the interface makes this morphology desirable for DSSCs [34]. The

key improvement provided by different $TiO_2$ nanotube film is the higher dye loading per unit volume [32].

Despite progress in the efficiency and stability of the dye sensitized solar cells there are many fundamental aspects of the physics and chemistry of their operation that are still unknown. One process, for which there is limited information, is the time taken to upload the dye into the $TiO_2$ film. The dye as a sensitizer plays an important role on the DSSCs. It serves as the solar energy absorber, whose properties have a significant effect on the light harvesting efficiency and the overall photoelectric conversion efficiency [35]. The ideal sensitizer for DSSCs should absorb all light below the threshold wavelength of about 920 nm [5]. It must be firmly grafted to the semiconductor $TiO_2$ surface so that it can inject electrons to the conduction band [36].

As mentioned above the dye adsorbed on the $TiO_2$ semiconductor film plays an important role in light absorption, but there are two requirements which are related to its adsorption on the $TiO_2$ film for high efficiency. The first requirements is electron injection time scales; that is, electron injection must occur faster than relaxation of the excited dye to the ground state. Thus the relatively strong electron transfer between the excited dye and the semiconductor is needed and it can be achieved if the dye is attached directly to the semiconductor surface. The second requirement is that only a mono layer of dye molecules must be formed on the $TiO_2$ surface to act as efficient sensitizer, as the aggregation of the dye molecules reduces electron injection [37].

The general procedure applied for dye adsorption onto the $TiO_2$ porous or nanotube film, is dipping it into a solution of dye. The reported time for this procedure ranges from several hours to days depending on the structure of the dye [38, 39]. However, such long dipping times are not economic for industrial production of the dye sensitized solar cells [16]. Also the time during which the $TiO_2$ film is immersed in the dye concentration affects the efficiency of the cell [38], and thus an optimum time for the dye uptake should be obtained for efficient conversion of light to energy. Therefore the dye uptake time has to be reduced in order to produce solar cells on industrial scale. It is also expected in general that the incident photon-to-current conversion efficiency (IPCE) increases linearly with the dye coverage, because more adsorbed dye molecules will absorb more photons [20]. In the present work we describe a model for the time taken to upload the dye molecules on the $TiO_2$ pore surface, the amount of dye molecules adsorbed and to understand the main factors controlling this time.

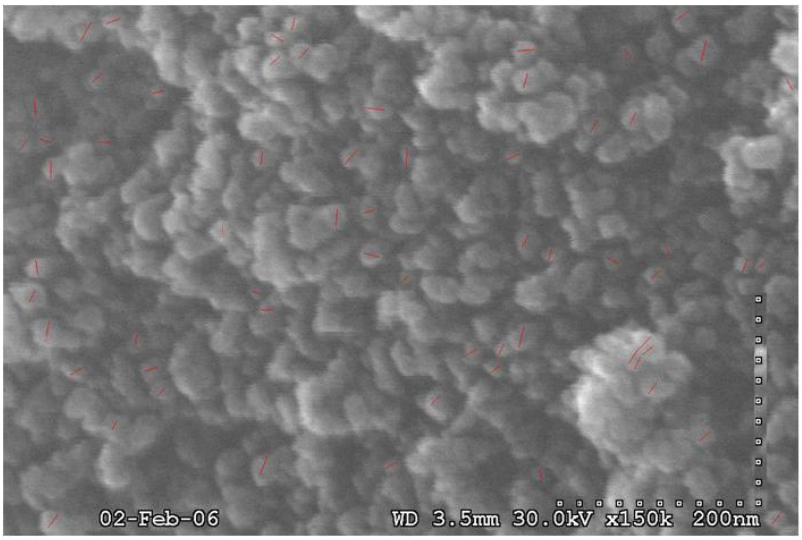


Figure 2.1: Scanning electron micrograph of $TiO_2$ porous film, image taken by K. Lobato

### 2.1.1 Titanium dioxide films

Titanium dioxide is the most commonly used wide band-gap semiconductor in DSSCs manufacturing process. Titanium dioxide is also used in number of products including cosmetics, paints, plastics and paper [5, 40]. As a non-toxic and relatively inexpensive compound titanium dioxide films serve as the main component of the DSSCs. The $TiO_2$ film has a large band gap and also a high specific surface area. Adsorption of dye sensitizer on the $TiO_2$ surface results in a formation of a monolayer of dye as a surface coverage. By increasing the contact area between the semiconductor and the dye, the amount of light harvesting is increased. The increased injection of electrons from the dye to the semiconductor film improves the efficiency of light harvesting. Apart from providing a folded surface to enhance light harvesting by the adsorbed sensitizer, the role of the $TiO_2$ film is to serve as an electron transporter [5]. The conduction band of the $TiO_2$ semiconductor accepts the electrons from the electronically excited sensitizer or dye molecules. The excellent light-harvesting efficiency achieved in the DSSCs using only a monolayer of adsorbed dye is due to the high surface area of the porous nanocrystalline $TiO_2$ layer [29, 41].

Figures 2.1 and 2.2 show the structure of $TiO_2$ porous film and nanotube film used in the DSSCs as an electron collector to support a monolayer of sensitizer. The exploration of new architectures for the $TiO_2$ film in DSSCs is expected to yield significant

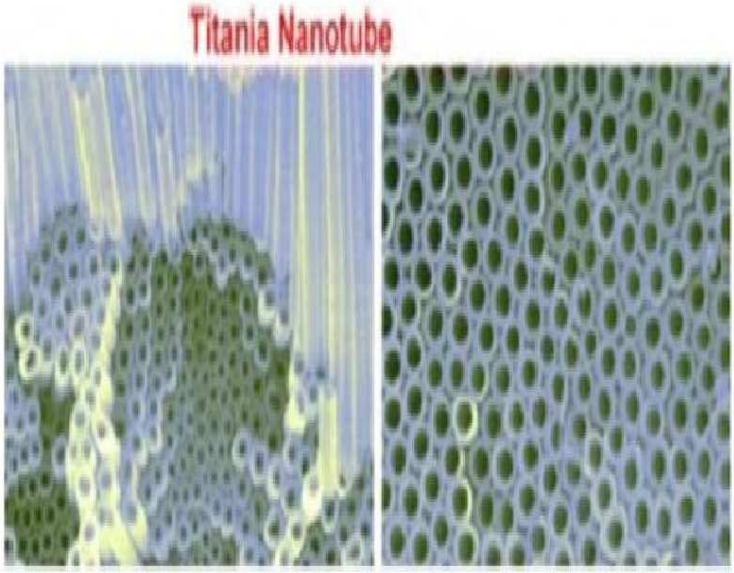


Figure 2.2: Scanning electron micrograph of image of titanium nanotube array used to fabricate dye-sensitized cells, image from [29]

improvements of the solar cell efficiency. The current manufactured DSSCs are composed of $TiO_2$ porous or nanoparticles film. Electron transport in the porous $TiO_2$ film compared to $TiO_2$ nanotube film is known to be relatively slow and is one cause of a decrease in efficiencies [42]. $TiO_2$ nanotube films are currently used in DSSC research for the improvement of the DSSCs efficiency, as they are expected to display improved charge transport in comparison with $TiO_2$ nanoparticle film. The current reported efficiency of $TiO_2$ nanotube film based DSSCs ranges from 6.9 to 7.6%, this is low compared to the 11.2% efficiency of DSSCs based on $TiO_2$ porous film [42]. As described above the most widely used porous material is $TiO_2$, although other wide-band semiconductor oxides such as ZnO (zinc oxide), $SnO_2$ (tin oxide), $SnO_2$/MgO or $Nb_2O_5$ (Niobium oxide) have also been employed. Table 2.1 illustrates the different efficiency obtained using these oxides. The nanocrystalline film consists of inter-connected colloidal particles in the size range of 15-30nm with layer thickness typically between 5-15 $\mu$m [28, 43]. The size and topography are key to increase the efficiency of capturing electrons. The colloidal $TiO_2$ material is prepared by a hydrothermal sol-gel method in acidic or basic aqueous media. The nanoparticles of the oxide are generally applied industrially in different ways, such as by screen printing onto the glass or flexible plastic support covered with transparent conducting layer of fluorine-doped tin oxide (FTO) or tin-doped indium oxide (ITO). Each particle is coated with a monolayer of dye molecules formed by self-assembly from a staining solution [28, 43].

| Oxide | Efficiency | Reference |
|---|---|---|
| $TiO_2$ | 11.2% | [42] |
| ZnO | 6% | [44] |
| $SnO_2$ | 1% | [45] |
| $Nb_2O_5$ | 5% | [46] |

Table 2.1: Comparison between power conversion efficiencies of different oxides used in DSSCs.

## 2.2 Importance of dye uptake in DSSCs

As discussed in the introduction chapter, the adsorption of dye on to the $TiO_2$ film is important for the performance of the solar cell as the dye is used as photon absorber [47]. The general understanding is that, a high surface dye coverage on $TiO_2$ film will give rise to a higher probability of electron injection and hence improves the overall efficiency of the solar cell. As reported by Chou *et al.* [38], insufficient surface coverage results in the reduction of the number of the photons absorbed and reduces the short circuit current and overall light conversion efficiency. Sufficient surface coverage of the light absorbing dye on the surface of the film will result in greater photon absorption and thereby increases the short circuit current and the overall conversion efficiency [38].

For the $TiO_2$ nanotube based DSSCs, it was found that the performance of the cells strongly depends on the morphology and electronic properties of the nanotubes [39]. The first key factor in $TiO_2$ nanotubes based solar cells, which determine the overall efficiency is dye-loading, that is, the available dye covered area on the tube walls [39]. The surface area of the $TiO_2$ nanotube film is one of the important parameters for the dye loading and improvements of the short circuit photocurrent ($J_{sc}$) [39]. According to Jennings *et al.* [29], the total internal surface area of the inside and outside of the nanotubes ($A_i$) of the titanium nanotube layers can be calculated using the expressions

$$A_i = \pi(D_i + D_o)lNA_p \tag{2.1}$$

where $D_i$ is the inner diameter of the tubes, $D_o$ is the outer diameter, $l$ is the tube length, N is the number of tubes per unit projected area and $A_p$ is the projected area of the nanotube layer.

## 2.3 Theory and model description

### 2.3.1 Adsorption

Adsorption processes from a liquid phase to a solid surface are of immense importance in diverse fields of everyday life, science and technology. Although the equilibrium properties of different adsorption systems are well covered in the literature, the rates of the processes have attained less attention [48]. As the adsorption process is between different objects, the kinetics of these processes depends on different parameters. In solution the rate depends on the diffusion coefficient of the adsorbate molecules, the movement of the molecules (convection) and the geometry of the adsorbent surface. At the interface the rate depends on the interaction forces between the adsorbate molecules and the surface [48]. The simplest adsorption process is the Langmuirian adsorption process in which no interactive forces between the adsorbate molecules are assumed and monolayers are assumed to be formed.

The present model is intended for a general case in which dye molecules are adsorbed on the surface of the $TiO_2$ pore to form a monolayer. It is based on the Langmuir isotherm model, which uses the active sites concept in an adsorption expression in order to address the reduction of its rate with the coverage of the wall [49]. The Langmuir isotherm model represents a simplified case of dye adsorption, since it assumes:

1. Adsorption of dye is controlled by transient diffusion along the pore
2. The dye is adsorbed to the surface of the pore and only a monolayer is formed.
3. Constant properties of molecules even after the adsorption

The added advantage of the Langmuir isotherm is that it relates the coverage or adsorption of dye molecules on the $TiO_2$ to the high concentration of the dye solution at a fixed temperature.

### 2.3.2 Model description (Comsol)

Finite element methods (FEM) are numerical techniques that are widely used in fields as diverse as chemical and structural-engineering. The method allows very complex, and analytically insoluble, problems to be solved approximately. In this work, the models are solved using the Comsol Multiphysics software which is commercially available and

solves systems of partial differential equation (PDE) and ordinary differential equations (ODE). One of the main selling points of the Comsol Multiphysics software is its ability to deal with so called Multiphysics Simulations; interacting equations which can be coupled together [50].

Analytical solutions of partial differential equations are restricted to simple domain geometries and boundary conditions. Therefore, they are of limited use in real-world applications. Numerical approximation methods, however, allow the handling of these complex problems. Originally developed for the analysis of mechanical structure, the Finite Element Software (FEM) is today widely used to solve problems in all fields of engineering and science [50]. Adsorption and diffusion of dye molecules has proven to be a challenging subject both theoretically and experimentally. Adsorption and diffusion processes under the Langmuir isotherm assumptions have been modelled mathematically to better understand the phenomena involved [51]. Also computer methods have been employed for decades to study adsorption processes in electrochemical systems characterized by semi-infinite diffusion, in order to get a better understanding of those phenomena [51]. In this work a numerical model using the finite element method based on Comsol software has been developed to study adsorption of dye molecules on the surface $TiO_2$ nanotube film. The work takes into account the diffusion and adsorption of the dye molecules on the pore and follows the Langmuir assumption.

Highly ordered $TiO_2$ nanotube films are currently getting more attention as an attractive candidate for a semiconductor in DSSCs [29, 31, 33, 34, 52]. A $TiO_2$ nanotube is represented by a cylinder penetrating the entire film with bulk concentration of dye molecules at the first end as shown in figure 2.3, with the bottom view illustrating the boundary condition as applied to Comsol multiphysics. The radius of the nanotube $R_0$ = 50nm and the length (d) = 20 $\mu$m. At the closed end of the nanotube we have a flux zero boundary condition, which shows that nothing is allowed to pass through. The other assumption is that the initial bulk concentration $c_d$ does not change. The implementation and boundary condition of the model is discussed in appendix A.

### 2.3.3 Diffusion-adsorption (present model)

We solved the diffusion equation (Fick′s second law), equation 2.2, for dye molecules concentration $c(r, z.t)$, where $r$ is the distance from the center of the pore in a radial direction, $z$ is the distance from the closed end of the pore and $t$ is the time,

$$\frac{\partial c}{\partial t} = D\nabla^2 c = \frac{D}{R_0^2}\left[\frac{1}{r}\frac{\partial}{\partial r}\left(r\frac{\partial c}{\partial r}\right)\right] + \frac{D}{d^2}\frac{\partial^2 c}{\partial z^2} \tag{2.2}$$

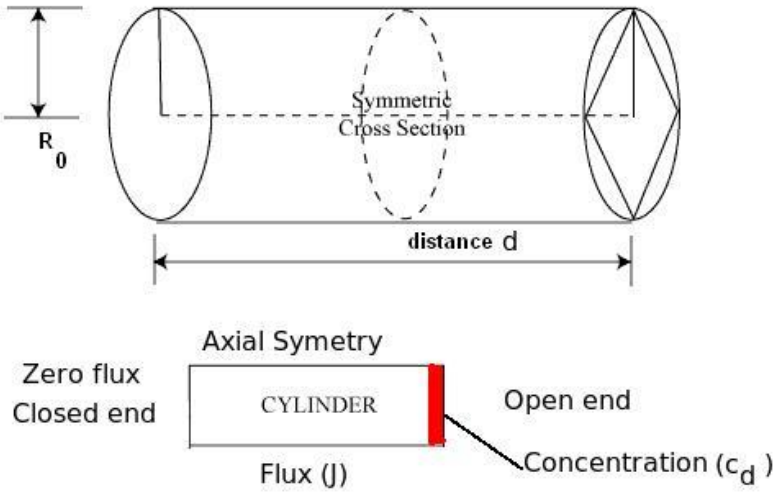


Figure 2.3: Top panel: Schematic representation of a $TiO_2$ nanotube pore where $R_0$ is the pore radius and d is the thickness of the nanotube film. Bottom panel: The boundary condition as applied in the Finite Element model (Comsol).

To find the net flux of dye molecules $J(z,t)$ moving towards the pore surfaces,

$$J = -D\frac{\partial c}{\partial t} \tag{2.3}$$

we consider the molecules flowing onto the surface and being adsorbed onto it less the desorbed molecules to give the fractional surface coverage, given by,

$$\theta(z,t) = \Gamma(z,t)/\Gamma_{max} \tag{2.4}$$

where $\Gamma(z,t)$, is the surface coverage a distance $z$ from the electron extracting electrode and $\Gamma_{max}$ is the maximum surface coverage of the $TiO_2$ nanotube film. If all molecules a distance $l_{mol}$ out from the surface are adsorbed, where $l_{mol}$ is the length of the dye molecule,

$$\Gamma_{max}\frac{\partial\theta(z,t)}{\partial t} = k_{ads}l_{mol}c(r,z,t)\,(1-\theta(z,t)) - k_{des}\Gamma(z,t) \tag{2.5}$$

where $k_{ads}$ and $k_{des}$ are respectively the adsorption and desorption rate of dye molecules.

It is worth mentioning that $l_{mol}$ is used in this model to account for the length of the dye molecules sticking on the nanotube surface. If there is no energy barrier to overcome for adsorption to occur then, every collision between a dye molecule and an active site will result in the adsorption of the dye molecule. The change in the dye concentration in the $TiO_2$ film arises from two processes: diffusion of dye molecules to the active layer on the $TiO_2$ film and the dye molecules adsorbing and desorbing from the active side in the layer. The diffusion of dye molecules on the $TiO_2$ film is described by the simple diffusion equation (Fick′s second law, equation 2.2) and the adsorption and desorption of dye molecules is described by surface flux boundary equation (Langmuir equation, equation 2.5).

We assume a state of quasi equilibrium, i.e, adsorption and desorption take place quickly compared to the time taken for the dye molecules to diffuse to the surface, thus the left hand side of equation 2.5 is set to zero [51, 53]. Hence, if $\kappa = \frac{k_{ads}}{k_{des}}$,

$$k_{ads} l_{mol} c(r, z, t)(1 - \theta(z, t)) - k_{des} \Gamma_{max} \theta(z, t) = 0 \tag{2.6}$$

so

$$\theta(z, t) = \frac{c(r, z, t)/c_{con}}{1 + c(r, z, t)/c_{con}} = 1 - \frac{1}{1 + c(r, z, t)/c_{con}} \tag{2.7}$$

where c(r,z,t) is the dye concentration and $c_{con}$ is the constant for Langmuir isotherm given by,

$$c_{con} = \frac{\Gamma_{max}}{\kappa l_{mol}} \tag{2.8}$$

The boundary conditions at the curved surface (radial axis), at all times $t$ is given by

$$J(r = R_0, t) = \Gamma_{max} \frac{\partial \theta(z, t)}{\partial t} = \frac{\Gamma_{max}/c_{con}}{(1 + c(R_0, z, t)/c_{con})^2} \frac{\partial c(R_0, z, t)}{\partial t} = - D \frac{\partial c(r, z, t)}{\partial r}\bigg|_{r=R_0} \tag{2.9}$$

The boundary conditions at the surface (along the nanotube), at all times $t$ is given by

$$J(z, t) = \Gamma_{max} \frac{\partial \theta(z, t)}{\partial t} = \frac{\Gamma_{max}/c_{con}}{(1 + c(R_0, z, t)/c_{con})^2} \frac{\partial c(R_0, z, t)}{\partial t} = - D \frac{\partial c(r, z, t)}{\partial z}\bigg|_{z=0} \tag{2.10}$$

The adsorption and diffusion of the dye molecules into $TiO_2$ nanotube pore was implemented and solved using the 2D axial symmetry in Comsol (FEM) Finite Element Methods Multiphysics package. The problem is set up as an axially symmetric transient conversion diffusion problem for the dye molecule flux and adsorption in the cylindrical geometry. The boundary conditions of bottom, top and side are all of conversion dif-

fusion type. At the beginning of the simulation the pore is empty except at a distance $w$ which is defined as $w = 0.01 \times$d, where d is the length of the $TiO_2$ nanotube.

## 2.4 Results

### 2.4.1 Characteristic time

Simple analytical characteristic time expressions were developed to understand the general behaviour of the diffusion of dye molecules along the nanotube radius and the surface (length) of the $TiO_2$ nanotube. Along a pore radius, the diffusion towards the pore surface occurs very quickly. The time scale is determined by the characteristic time for a dye molecule to diffuse along a radius to the pore surface,

$$t_r = \frac{R_0^2}{D} \tag{2.11}$$

where D is the dye diffusion coefficient, $R_0$ is the radius of the pore. Along the pore surface the time scale is determined by,

$$t_z = \frac{d^2}{D} \tag{2.12}$$

where d is the length of the pore.

### 2.4.2 Numerical results

As illustrated using the characteristic time expressions equations 2.11 and 2.12, the diffusion along the pore radius is very fast compared to the diffusion along the pore surface, where adsorption and desorption of dye molecules takes place. For shorter time scales the pore is filled only in the radial direction. For example, with a radius of the nanotube $R_0 = 10$nm and the diffusion coefficient $D = 2 \times 10^{-10} m^2 s^{-1}$, the radial diffusion time scale is $\approx 50$ ps. For long times, the pore is filled as the dye is replenished from outside the pore and the dye concentration everywhere reaches a uniform value of $c_d$. Because of the rapid diffusion in the radial direction noted above, the surface concentration does not vary with the radius of the nanotube except over times much shorter than shown here. Diffusion along the pore is slowed down by adsorption of the dye molecules at the pore surface. The adsorbed molecules are removed from solution, so more dye has to diffuse in from the pore entrance at z = d to replace them.

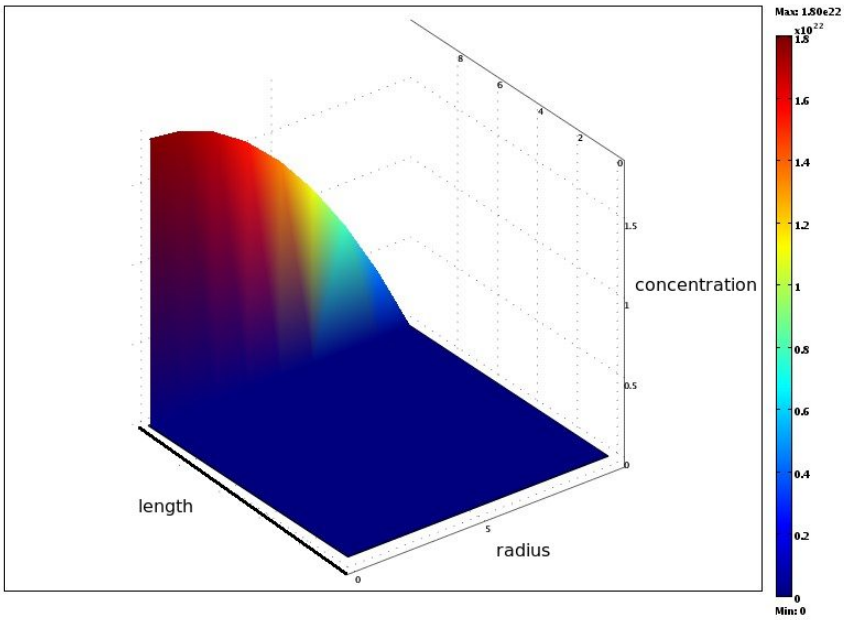


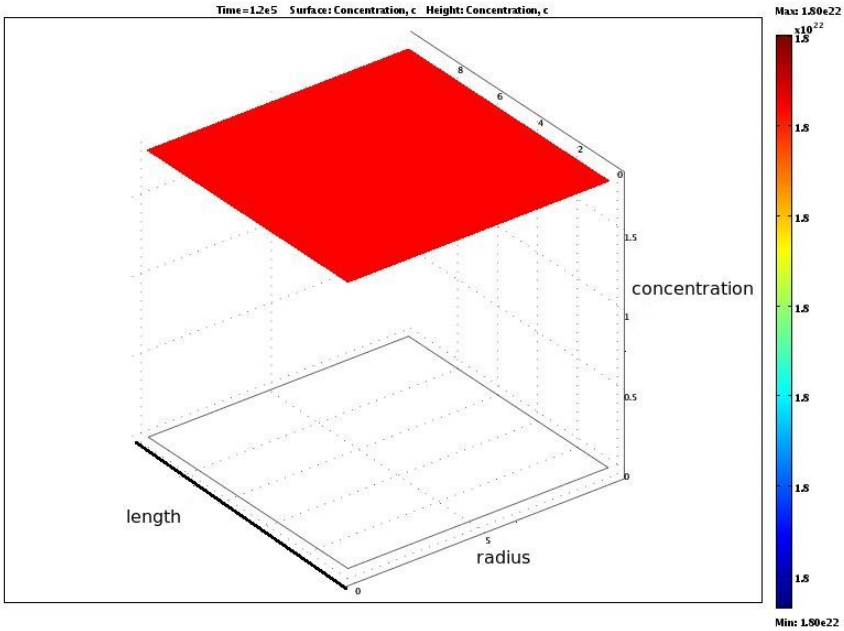


Figure 2.4: 3D plot of c(r, z, t = 0) (A) and c(r, z, t $\rightarrow \infty$) (B). The z axis goes into the page, with the open edge of the pore at z = d (open end) at the back and the r axis goes from left to right, with the right hand edge being r = $R_0$.

Figure 2.4 (A), shows the initial condition. As shown in the figure, initially we have an empty pore except at distances $z > 0.01d$, where we have the bulk concentration ($c_d$) of dye flowing into the pore. Figure 2.4 (B), shows the distribution of the concentration at longer time, it can be observed by looking at the colour change that there are dye molecules adsorbed on the surface of the pore. At longer time (t$\rightarrow \infty$) we expect the concentration $c_d$ to be uniformly distributed along the pore. This is clearly illustrated by the colour bar of figure 2.4 (B).

#### 2.4.2.1 Duration of dye loading

Currently the dye loading procedure followed is dipping the $TiO_2$ films into dye solution for several hours and even days. The dipping duration time is important as it determines the photocurrent of the device [38, 39]. Optimization of the dye uptake time is one of the important factors especially for the manufacturing of the DSSCs as shorter times will be effective for industrial solar cell production, rather than hours or days. Ghicov *et al.* [39] reported that the short circuit photocurrent increases up to 4 days of dye loading and for greater immersion times like 7 days the short circuit photocurrent decreases due to aggregation of dye on the surface. This process leads the dye molecules to gather together or sit on top of each other. If micro-cluster of dye molecules is present on the surface of the $TiO_2$ semiconductor, the efficiency of the electron injection is reduced. Therefore an optimum time is needed for dye uptake to prevent the dye aggregation [37].

Simulations were performed to study the factors affecting the dye loading time. As illustrated in figure 2.5 (A) and (B), the value of the adsorption-desorption ratio ($\kappa$) plays an important role in the time taken for dye uploading. Comparing the two figures (A) and (B), it is clear that there is a difference in the saturation time between the two values of $\kappa$. As shown by the characteristic times expressions (see section 2.4.1 above) the diffusion along the pore radius is faster compared to the slower diffusion on the nanotube surface which is affected by the adsorption and desorption of dye molecules. This delay is seen more clearly for the much larger value of $\kappa$ used in figure 2.5 (B), as in this case almost all the molecules landing on the surface stick. These results show that the dye uptake time depends on the value of $\kappa$. From the figure our simulation shows that, it can take as long as 25 minutes or 2000 minutes depending on the values of $\kappa$ and diffusion coefficient, to reach a saturation time for the dye upload for an initial dye concentration of $c_d = 6\times\ 10^{21}$ m$^{-3}$. These results show that, depending on the nature of the material ($\kappa$ and D), it can take few hours for sufficient dye uploading. Several time scales have been reported for dye uptake like 20 minutes for higher dye concentration ($5\times10^{-4}$M) [38], which was enough to give a higher light

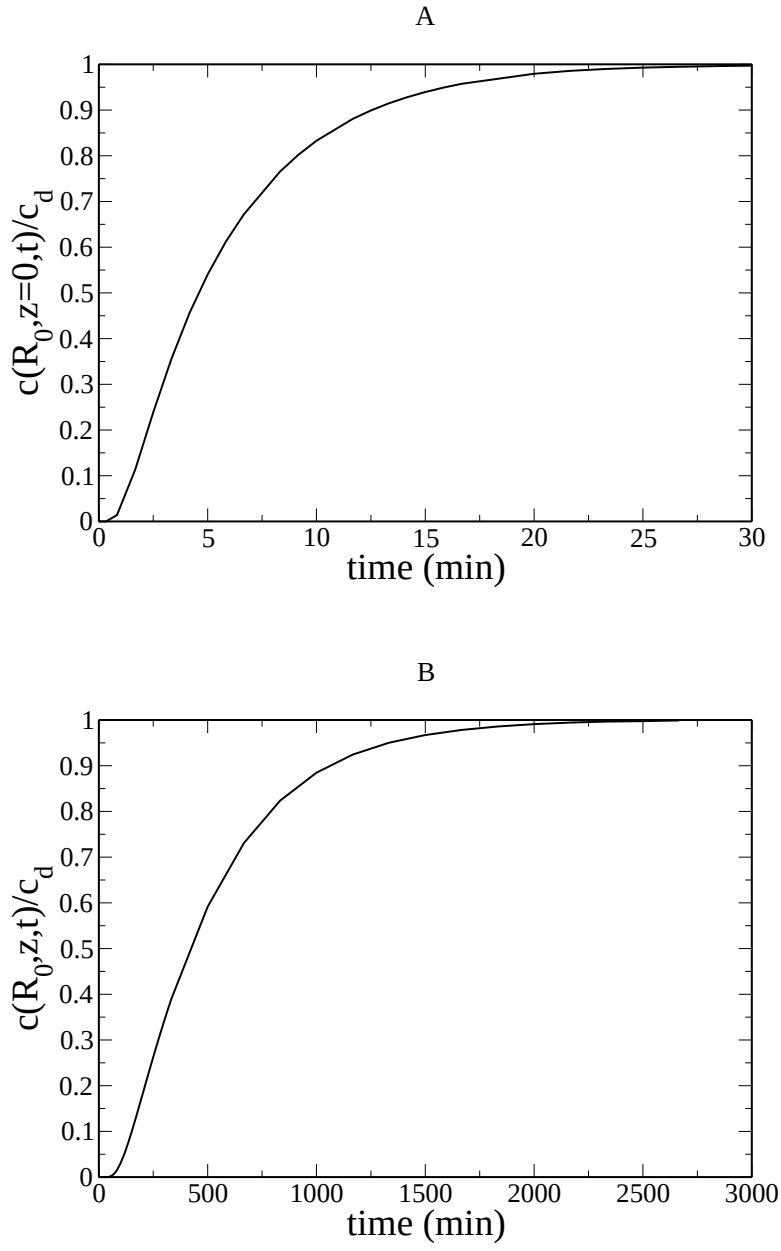


Figure 2.5: Time required to upload the dye on the pore, measured as $c(r = R_0, z = 0, t)/c_d$=0.99, for $\kappa = 10^4$ (A) and $\kappa = 10^6$ (B). The value used for calculations are $c_d$ = 6× $10^{21}$ $m^{-3}$, $D = 5.5 \times 10^{-10}$ $m^2 s^{-1}$, $\Gamma_{max} = 2 \times 10^{19}$ $m^{-2}$, d = 20 $\mu$m.

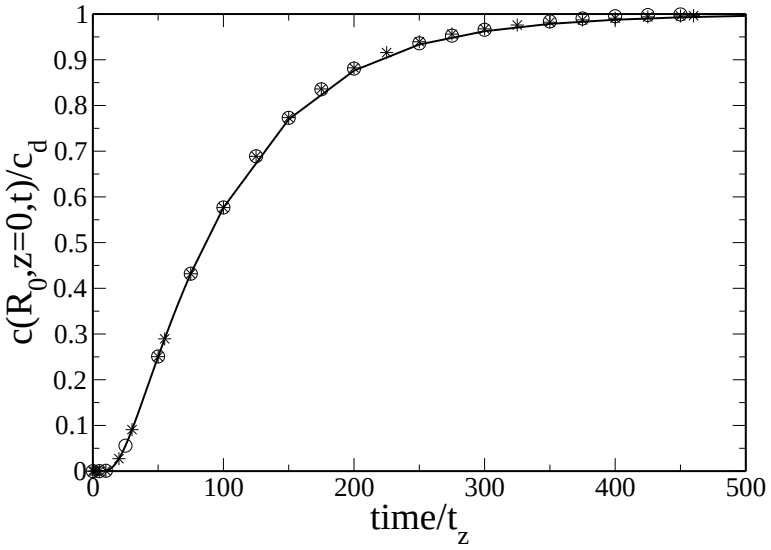


Figure 2.6: Dependence of $c(r = R_0, z = 0, t/t_z)/c_d$ on the different values of diffusion coefficient, for D = $2 \times 10^{-8}$ $m^2s^{-1}$ (cycle), D =$2 \times 10^{-9}$ $m^2s^{-1}$ (star), D = $2 \times 10^{-10}$ $m^2s^{-1}$ (solid line), $\kappa = 10^6$,$c_d = 6 \times 10^{21} m^{-3}$, $\Gamma_{max} = 2 \times 10^{19}$ $m^{-2}$

conversion efficiency, 5h for adsorption of phenol red into the $TiO_2$ nanotube film with diffusion coefficient of about 9 $\times 10^{-7} cm^2s^{-1}$ [41] and 1 to 7 days for dye uptake on $TiO_2$ nanotubes film [39]. This shows that the optimization of the duration of dye loading on the $TiO_2$ film is an important subject for research in DSSCs and there is a need to optimize the dye uploading time for a better performance of the solar cell and industrial production. The meanings of $D$ and $\kappa$ need to be understood, so that an optimum time and sufficient coverage of the film can be achieved.

The adsorption of dye molecules onto the $TiO_2$ surface is based on the diffusion process, thus the diffusion coefficient plays an important role on the dye uptake time. A higher value of diffusion coefficient reduces the time to upload the dye, while a lower value increases the time for dye uptake in the pore. For a higher diffusion coefficient we expect the dye molecules to move fast compare to lower diffusion coefficient, which results in greater number of dye molecules moving into and sticking on the surface of the nanotube in less time. This results show that the value of the diffusion coefficient should be as high as possible and its meaning need to be understood both experimentally and theoretically. Figure 2.6 shows the time variation of the dye uptake on the pore at the closed end. It can be observed that the variation is the same for different diffusion coefficients. The graph has been scaled by the time $t_z$, given by equation 2.12.

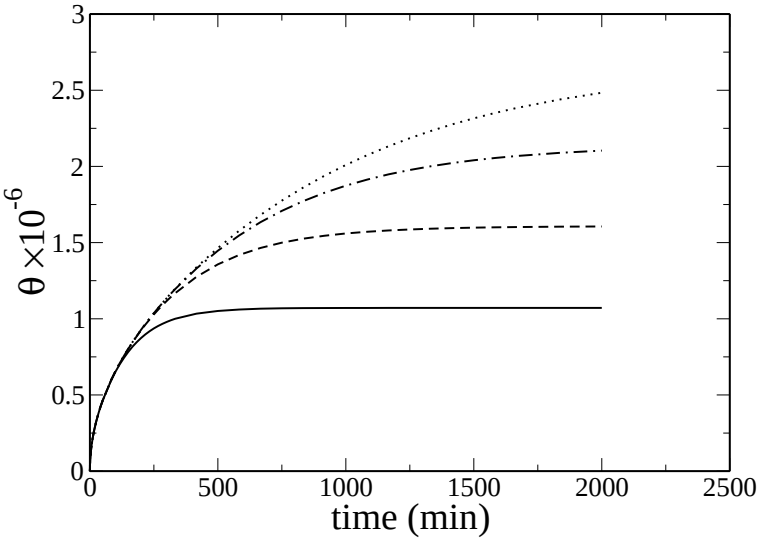


Figure 2.7: The effect of changing the $TiO_2$ nanotube film thickness on the surface coverage, i.e., $d = 10$ $\mu$m (solid line), $d = 15$ $\mu$m (dashed line), $d = 20$ $\mu$m (dash dot line), d = 25 $\mu$m (dotted line) the value used for calculations are $c_d = 6\times\ 10^{21}$ $m^{-3}$ , D = $8.5 \times 10^{-10}$ $m^2s^{-1}$, $R_0 = 10$ nm, $\Gamma_{max} = 5 \times 10^{19}$ $m^{-2}$ and $\kappa = 2 \times 10^6$

#### 2.4.2.2 Surface coverage

As discussed above in DSSCs the surface of the $TiO_2$ nanotube or porous film is one of the most important factors, as it gives the probability of the amount of dye to be adsorbed onto it. The understanding is that the higher the surface area covered by the dye molecules, the higher the probability of absorption of photons. As the dye is the main parameter for the photon absorption, there is a need to understand the effects of the film surface on the amount of dye molecules adsorbed onto the surface. In DSSCs based on the $TiO_2$ nanotubes film, several parameters need to be understood for the adsorption of dye onto the surface. These are parameters such as the nanotube length and others. Simulations were done in order to evaluate the influence of the $TiO_2$ nanotube length on the surface coverage and the saturation time.

Figure 2.7 shows the effect of varying the nanotube film thickness on the surface coverage. As indicated in the figure, the surface coverage increases with increasing film thickness. It is also worth to note that the variation of the nanotube film thickness is achieved by increasing the length of the nanotube. Thus as we increase the thickness of the $TiO_2$ nanotube film, we are increasing the surface area, which gives a higher probability of dye molecules sticking on the surface. This is also one of the research areas in dye sensitized solar cells that has been given attention for the improvement of

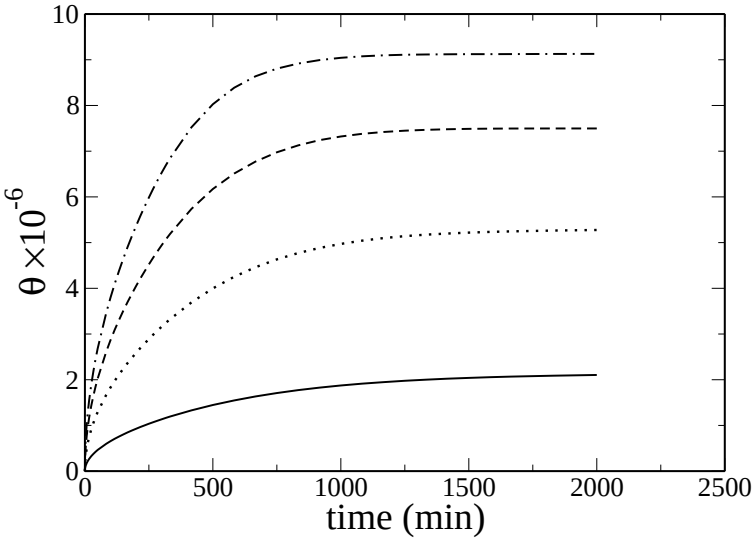


Figure 2.8: Dependence of the surface coverage on the initial dye concentration ($c_d$), i.e., $c_d = 6\times\ 10^{21}$ m$^{-3}$ (solid line), $c_d = 1.8\times\ 10^{22}$ m$^{-3}$ (doted line), $c_d = 3\times\ 10^{22}$ m$^{-3}$ (dashed line), $c_d = 4.2\times\ 10^{22}$ m$^{-3}$ (dash dot line), the value used for calculations are D = 8.5 $\times\ 10^{-10}$ m$^2$s$^{-1}$, d = 20 $\mu$m, $\Gamma_{max} = 5\ \times\ 10^{19}$ m$^{-2}$ and $\kappa = 2\ \times 10^6$

the efficiency [42]. A close look in the figure 2.7 shows that the initial speed of the dye uptake process is the same for different values of nanotube thickness. The increasing of the saturation time with the increasing film thickness, is from the fact that as we increase the film thickness we are increasing the number of the active sites (surface available for dye attachment) on the film. So we expect more dye molecules to be adsorbed on the surface of the film and this will lead to an increase in the saturation time as it will now take longer than in a thin film with less active sites.

As reported by Ghicov *et al.* [39], increasing the thickness of the film leads to an increase in the short circuit photocurrent. This increase can be attributed to the higher surface available for dye attachment and therefore a higher number of photogenerated electrons. As illustrated on figure 2.7 increasing the length of the nanotube increases the surface coverage, which means that there will be a higher amount of dye molecules adsorbed on the surface.

The initial dye concentration (bulk concentration) is one of the main factors which affects the surface coverage and the dye uptake time. Figure 2.8 illustrates the dependence of the surface coverage on the initial dye concentration ($c_d$). It can be observed from the figure that the surface coverage ($\theta$) increases with increasing $c_d$. As we increase the amount of the bulk concentration we are increasing the number of dye molecules

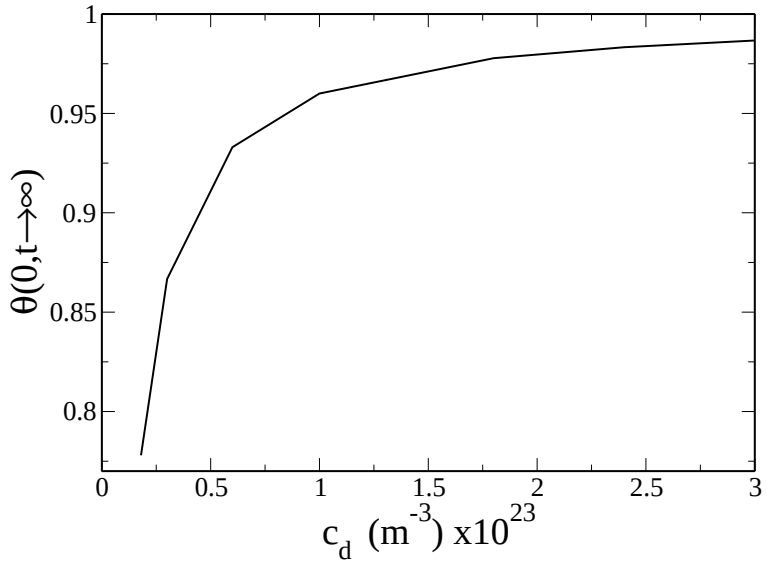


Figure 2.9: Surface coverage at the extracting electrode side for long times $\theta(0, t \to \infty)$ vs initial concentration $c_d$, d = 10 $\mu$m, $\Gamma_{max} = 2 \times 10^{19}$ m$^{-2}$ and $\kappa = 10^6$

in the solution. Thus we are also increasing the probability of more dye molecules to diffuse into the nanotube and hence reducing the saturation time. As illustrated in the figure the saturation time decreases with increasing $c_d$. Similar effects of the initial bulk concentration on the saturation time were reported experimentally by Chou *et al.* [38]. They further reported that at higher dye concentrations, a shorter immersion time is needed to obtain the highest overall light conversion efficiency and for lower dye concentrations, a longer immersion time is needed to obtain the highest overall light conversion efficiency, as insufficient surface coverage of the light-absorbing dye molecules attached on the surface of the film would result in the reduction in the number of electrons injected, consequently decreasing the short circuit current density and overall light conversion efficiency [38].

As discussed above the initial bulk concentration ($c_d$) at the open end of the pore is an important parameter, as it determines the concentration and coverage thoughout the pore at very long times. Figure 2.9 shows how the surface coverage $\theta(0, t \to \infty)$ from equation (2.7) varies with $c_d$. The figure demonstrates that $\theta(0, t \to \infty)$ is close to unity for a wide range of $c_d$ values. This is in agreement with the Langmuir assumption that only a monolayer is formed at the surface of the pore.

## 2.5 Comparison with experimental results

Experiments measurements of dye uptake on the $TiO_2$ nanotubes film were performed by H.Wang, at the University of Bath, Department of Chemistry. The $TiO_2$ nanotubes film samples were annealed in air at 450 $^oC$ for 2 h and then cooled to 100 $^oC$ before being immersed in a glass vial containing the dye cis-bis(isothiocyanato)bis(2,2'-bipyridyl-4,4'-dicarboxylato)-ruthenium($II$) bis-tetra (N719) in ethanol at different initial concentration (0.01 and 0.03 mM). The vial was then sealed completely. The variation of the absorption spectrum of the solution with time was monitored by a UV-Visible spectrophotometer (Varian, Cary 50). The characteristic absorption peak of the dye at 535 nm was used to calculate the amount of the dye adsorbed onto the film. Simulations were performed to compare the modelling results with the experimental dye uptake results. The main parameters used for the fitting of results are the diffusion coefficient (D) and adsorption-desorption ratio ($\kappa$).

Simulations were performed for comparison with the experimental results. The parameter $\Gamma_{max}$ used for fitting was calculated as described by Jennings *et al.* [29]. The value of diffusion D = 4 $\times$ $10^{-11}$ $m^2s^{-1}$ used for the fitting was found to be in agreement with the reported results in literature. For example a value of D = 1$\times$ $10^{-11}$ $ms^{-1}$ for diffusion of Phenol Red on nanotube arrays of 1000 $\mu$m length [41] and D = 4$\times$ $10^{-11}$ m $s^{-1}$ for adsorption of proteins on the walls of a microchannel [49]. The value of $\kappa$ was determined from the normal Langmuir constant ($K$). $K$ is in dimension of $mol^{-1}$ $m^3$ and our $\kappa$ is dimensionless as we account the length which is occupied by the dye molecule ($l_{mol}$) on the film. The value of $K$ can be determined from the dye uptake under equilibrium conditions (time greater than 30 h). From the Langmuir surface coverage ($\theta$) equation given by [49],

$$\theta = \frac{Kc}{1 + Kc} \tag{2.13}$$

it follows that,

$$\frac{1}{\Gamma} = \frac{1}{K\Gamma_{eq}}\frac{1}{c} + \frac{1}{\Gamma_{eq}} \tag{2.14}$$

So that $\Gamma_{max}$ and $K$ can be determined from a straight line fit of $\frac{1}{\Gamma}$ vs $\frac{1}{c}$. This is clearly illustrated by figure 2.10. Only the lower bulk concentration were considered, as there is aggregates problem of dye molecules when using the higher bulk concentration. After getting the value of $K$ we convert it to $\kappa$ as [54],

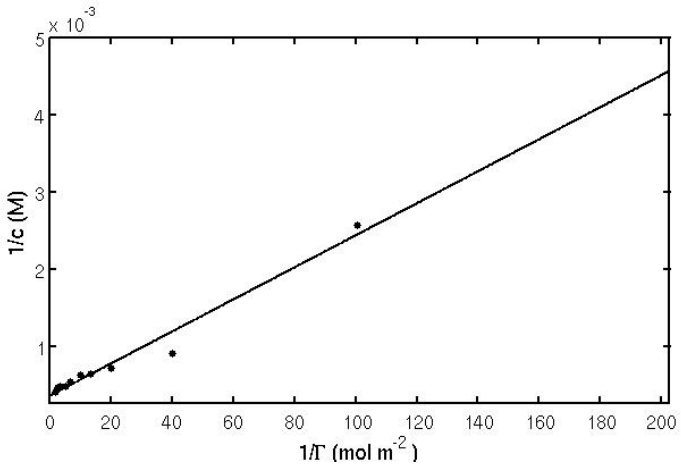


Figure 2.10: Graph of $\frac{1}{\Gamma}$ vs $\frac{1}{c}$ with a straight line fit, to illustrate how $\Gamma_{max}$ and $K$ can be determined.

$$\kappa = K\left(\frac{\Gamma_{eq}}{l_{mol}}\right) \tag{2.15}$$

where $\Gamma_{eq}$ is the monolayer coverage from the dye uptake under equilibrium.

Figure 2.11 (A) and (B) compare the experimental and modelling results for dye adsorption on a 20 $\mu$m nanotube for the bulk concentration of 0.01 mM and 0.03 mM respectively. From figure (A) we observe good agreement between the modelling and experimental results. After several hours it can be seen that experimentally the dye uptake reaches equilibrium slowly. The reason for the observed lower rate for dye adsorption at longer time, is that at this point in time there are less active sites on the $TiO_2$ nanotube film available for the dye molecules to be adsorbed. At the beginning of the adsorption, there are large number of vacant active sites on the $TiO_2$ nanotube film available and the initial rate of dye uptake is quite fast. However as the active sites are filled, fewer vacant active sites remain and relatively more dye molecules remain in solution. For higher concentrations, at the beginning of the process we have a large number of vacant active sites and more dye molecules in the solution, which leads to a faster diffusion process. This can be observed on figure (B), which shows that, experimentally the adsorption of dye is very fast for the first few hours and starts to saturate quickly. This observation clearly illustrates that during the process of adsorption and desorption of dye molecules into the $TiO_2$ film, we are changing the concentration inside the film and occupied sites of the surface.

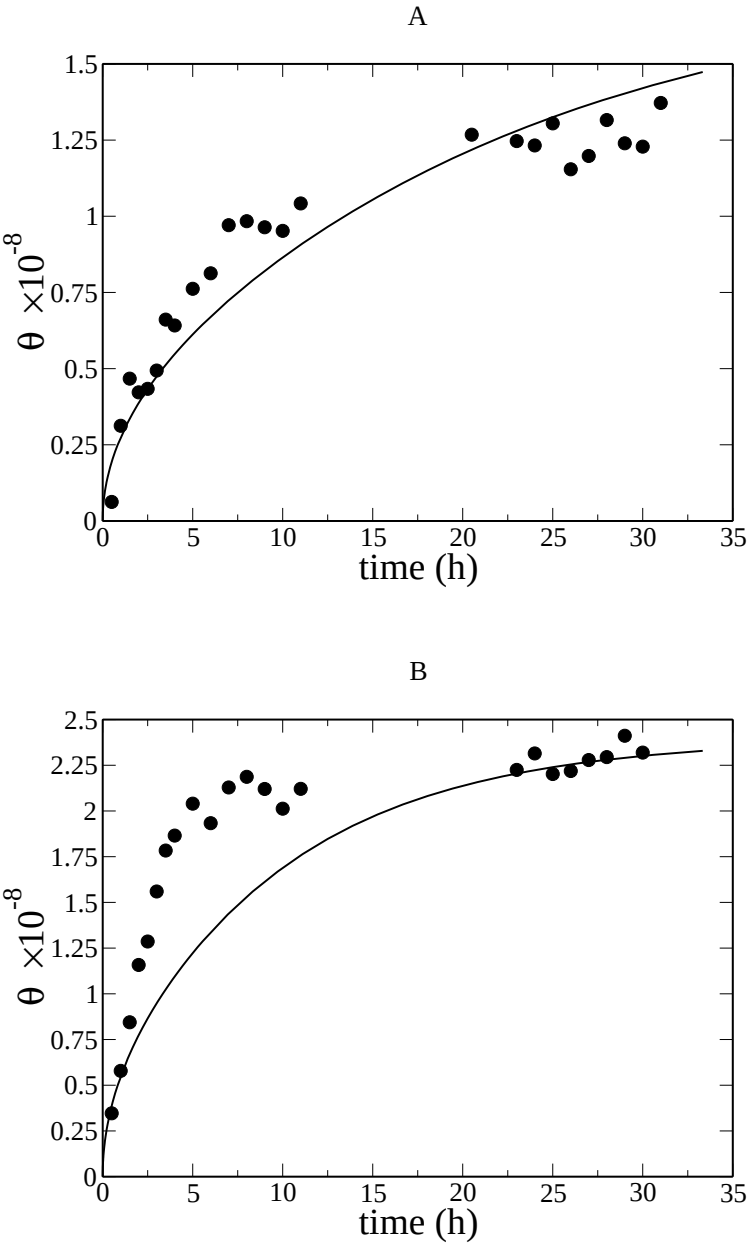


Figure 2.11: Comparison between the experimental (filled circle) and modelling (solid line) results for dye uptake on a 20 $\mu$m nanotube, for bulk concentration 0.01mM (A) and 0.03mM (B). The value used for modelling are D = 4 $\times$ $10^{-11}$ $m^2s^{-1}$, $\Gamma_{max}$ = 8.5 $\times$ $10^{19}$ $m^{-2}$ and $\kappa = 1 \times 10^6$

The similar observation of a very fast dye uptake for the first few hours and then a slower rate as the active layer of the film decreases, was also reported by Holliman *et. al* [55], where they have studied the dye adsorption on different $TiO_2$ film samples. The faster and slower dye uptake can be attributed to the fact that, at the beginning of the process there are many numbers of active sites on the $TiO_2$ nanotube film and for a longer time the active sites on the $TiO_2$ nanotubes film decreases and it takes longer for the dye molecules to find an active site to stick. It is clear from figure 2.11 (A) and (B), that for a lower concentration the saturation time is higher compared to the saturation time for higher concentration. The trend of the modelling and the experimental results for the effect of different dye concentrations on the immersion time for dye adsorption agree well with the results reported by Chou *et. al* [38]. To understand the discrepancy between the Comsol based model and the experimental results, a 1D model was developed using an effective diffusion coefficient illustrated in Appendix A, section A.2.3. It is worth mentioning that the Comsol based model mimics the experimental dye uptake process as it takes into account both diffusion and the adsorption and desorption of the dye molecules at the surface of the film, while the 1D model only takes into account the diffusion of the dye.

## 2.6 Conclusion

In this work we have developed a simple model for dye uptake in DSSCs. The model presented shows that it can take a few hours for the dye to be adsorbed onto a nanoporous $TiO_2$ film in a DSSC, in agreement with experimental results. Our model shows that the time depends on the ratio of adsorption to desorption rates $\kappa$ and so will vary for different film materials. The diffusion coefficient also plays an important role in the dye uptake time, but our modelling results show that the concentration variation is the same for different diffusion coefficients and can be given by scaling the time by the simple expression for $t_z$ in equation (2.11).

Future work

In this work more effort was devoted to the adsorption of dye molecules into the $TiO_2$ nanotube film as one of the films which has recently been taken into consideration for efficiency improvement of the dye sensitized solar cells. The focus of this work was looking at the diffusion of dye into the nanotube, but the dye molecules can also be adsorbed on the outside of the nanotube. Further work will be to extend the model so that it can also take into consideration the dye molecules which are adsorbed on the outer side of the nanotube film. The market production of the dye sensitized solar cell is based on the $TiO_2$ porous film, work is in progress looking at the dye uptake process in the $TiO_2$ nanoparticle film rather than the $TiO_2$ nanotube film. Currently further work is planned to be done, where more effort will be looking at the variation of different $TiO_2$ film geometries and all the other related parameters. The experimental starting point can be done by comparing the dye uptake on anatase, brookite and rutile $TiO_2$ films.

# Chapter 3

# Electron Diffusion Length in Dye Sensitized Solar Cells

## 3.1 Preamble

In this chapter we introduce a reliable new approach to estimate the effective electron diffusion length $L_n$ theoretically described using a multiple trapping model which involves calculating the effective electron diffusion coefficient $D_n$ and lifetime $\tau_n$. We show that in this context,

$$L_n = \sqrt{D_n \tau_n} \simeq L_0 = \sqrt{D_0 \tau_0} \tag{3.1}$$

where $L_n$ and $L_0$ are the effective and free electron diffusion length respectively. The parameters $D_0$ and $\tau_0$ are defined as the free diffusion coefficient and lifetime of the conduction band electrons respectively.

In dye sensitized solar cells (DSSCs) light absorption occurs on dye molecules attached to $TiO_2$ nanoparticles. An electron is injected from the excited dye to the $TiO_2$ semiconductor film and moves by diffusion until it is collected at the substrate or lost by recombination during the process [29, 56, 57, 58]. The apparent absence of electrical field components normal to the substrate is attributed to effective shielding of photoinjected electrons by high concentration of ions in the electrolyte. The diffusion of electrons to the substrate contacts gives rise to a time delay between the electron injection into the $TiO_2$ semiconductor film and electron collection at the substrate. The competition between the electron transport to the anode and the electron transfer to tri-iodide ($I_3^-$)

ions in the electrolyte determines the efficiency of the collection of the photoinjected electrons. The important parameter in this process is the effective electron diffusion length ($L_n$), defined as the average distance an injected electron can travel through the cell before recombination. $L_n$ is determined by $D_n$ and $\tau_n$ as [29, 56, 57, 58, 59, 60],

$$L_n = \sqrt{D_n \tau_n} \tag{3.2}$$

If $L_n \gg d$ (where $d$ is the device thickness), only a small fraction of injected electrons will be lost before it is collected. Thus, a longer electron diffusion length is desirable for a higher probability of collecting more injected electrons. Efficient cells are characterized by a value of $L_n$ that considerably exceeds the $TiO_2$ film thickness [61, 62]. In the multiple trapping model, $D_n$ and $\tau_n$ are controlled by the distribution of electrons in the conduction band and the trapping states, apart from $D_0$ and $\tau_0$.

Several recent studies have indicated that values for $L_n$ derived by different methodological approaches can be significantly different [19, 63, 64]. It has been shown that the reason for the discrepancy between the techniques is probably caused by invalid assumptions in the analysis of the steady state data, like the assumption that recombination of electrons with electrolyte is first order in conduction band concentration [64]. Despite the limited relevance of $L_n$ obtained by small-perturbation methods to device operation, it is important to reaffirm the underlying theoretical model commonly used to describe electron transport in DSSCs. In a related study of the electron diffusion length, Leng *et al.* [65] have recently found that steady state IPCE measurements and transient photovoltage measurements yield similar values of the $L_n$ in a $TiO_2$ based water splitting cell [65]. Recently Jennings *et al.* [66] compared three different techniques (IPCE, electrochemical impedance spectroscopy (EIS), modulated impedance method (IMPS and IMVS)) to study the electron diffusion length and found good agreement. They also concluded that the simple diffusion recombination (multiple trapping) model used to describe the DSSCs operation is correct, provided the assumptions and conditions made during experimental measurements are the same [66]. In this work following in agreement with Jennings *et al.* [66] conclusion, we set out to show that using the first order electron recombination assumption in the multiple trapping model the value $L_n$ and $L_0$ are almost the same.

## 3.2 Intensity modulated photocurrent and photovoltage spectroscopy

A standard characterization technique of a photovoltaic (PV) device consists of the determination of the DC current-voltage curves under different incident light intensities. Such curves do not provide any information about the internal dynamics of the PV devices. Therefore additional information needs to be obtained using time and frequency dependent measurements. The application of small perturbations, such as small AC amplitude variation in the light intensity of variable frequency drives the system out of equilibrium so that measurements of transient response provide information about internal processes [58, 59, 67].

Intensity modulated photocurrent and photovoltage spectroscopy (IMPS and IMVS), are well established methods for the determination of an effective electron diffusion coefficient and lifetime, $D_n$ and $\tau_n$ [68]. These are the most important ingredients for estimating $L_n$ especially when calculated at the same average quasi Fermi level (corresponding to the same free electron concentration or equivalently the same trapped electron concentration). IMPS and IMVS involve a superimposition of a small sinusoidal perturbation of the light intensity on a large steady state background level [58, 59, 60, 67, 69]. In terms of theory analytical IMPS expressions for the diffusion limited and kinetically limited case have been derived [60], where the extraction rate constant $k_{ext}$ for electron transfer from $TiO_2$ to the substrate is included. Numerically the solution for the excess electron density profile can be obtained for short and open circuit when $k_{ext}$ value is large and zero respectively. So far a useful approach to extract the effective diffusion coefficient is by fitting the experimental IMPS responses to the analytical solution. This approach assumes that $D_n$ is constant throughout the film, whereas it must vary with position [29, 60, 67]. In this work we consider a full numerical solution of the time dependent continuity equation with trapping and detrapping of electrons to calculate the frequency dependence of the IMPS and IMVS response data. Thus a convenient way to estimate $D_n$ and $\tau_n$ is obtained by noting the minimum of the frequencies at which they are minimized. These frequencies corresponds to the inverse of the mean transient time ($\tau_{tr}$) for electron diffusion to the substrate (IMPS) and the inverse of the electron life time (IMVS) [29].

A widely used but incorrect approach is when $L_n$ is derived using $D_n$ and $\tau_n$ calculated at the same intensity. This approach gives a different quasi Fermi level at short and open circuit. Under open circuit the quasi Fermi level is higher compared to the short circuit and this leads us to underestimate $L_n$, as the IMPS response is obtained at a lower $E_{Fn}$ value compared to IMVS response. This problem can be avoided by calculating the effective diffusion coefficient and life time at the same quasi Fermi level,

which constitutes a major correction in the calculation of $L_n$ as we demonstrate below.

## 3.3 Multiple trapping model

The multiple trapping model is essentially an attempt to explain electron transport, which experimentally could be looked at through measurements by frequency domain techniques, incident photon-to-current conversion efficiency (IPCE) ratio, electrochemical impedance spectroscopy (EIS), etc. Electrons are assumed to partake in a random walk in the $TiO_2$ conduction band, being free. This random walk is interrupted by trapping events where an electron becomes localized in a trap state below the conduction band edge; the electron is now taken to be immobile and trapped until it is thermally released back into the conduction band and the random walk continues. This trapping and detrapping process occurs multiple times during transit across the $TiO_2$ film, hence the name multiple trapping model.

As a model which is related to electron transport in the dye sensitized solar cell, it considers diffusion as the main driving force of electrons in the $TiO_2$ semiconductor. Several works have been reported using the multiple trapping model to describe several aspects of electron transport on the DSSCs [70, 71, 72]. As far as the author knows it has not hitherto been shown that in the multiple trapping model $\mathrm{L}_0 \simeq \mathrm{L}_n$.

Experimentally the effective electron diffusion coefficient as measured by frequency domain techniques is found to vary with the intensity [29]. This intensity dependence is often explained by the multiple trapping model. The time dependent continuity equation for conduction band density $n_c$, in which traps are explicitly considered, is given by [29, 56, 57, 58, 59, 60, 68, 73, 74],

$$\frac{\partial n_c}{\partial t} = D_0 \frac{\partial^2 n_c}{\partial x^2} + \alpha I_0 e^{-\alpha x} - k_{cb}(n_c - n_{eq}) - \frac{\partial n_t}{\partial t} \tag{3.3}$$

$$\frac{\partial n_t}{\partial t} = N_{t0}\langle \frac{\partial f}{\partial t} \rangle = \langle k_t n_c (1-f) - k_d N_{t0} f \rangle = k_t \langle n_c (1-f) - e_{et} f \rangle \tag{3.4}$$

The continuity equation for $f$ is

$$N_{t0}\langle \frac{\partial f}{\partial t} \rangle = \langle k_t n_c (1-f) - k_d N_{t0} f \rangle - k_{tb}(n_c - n_{eq}) = \frac{\partial n_t}{\partial t} - k_{tb} N_{t0} \langle f - f_{eq} \rangle \tag{3.5}$$

where $D_0$ is the free electron diffusion coefficient, $\alpha$ the absorption coefficient, $I_0$ the

illumination intensity, $k_{cb}$ is the recombination rate of conduction band electrons, $n_{eq}$ is the equilibrium density of electrons in the dark, $N_{t0}$ is the total density of trap sites, $f$ is the trap occupation probability, $k_t$ is the trapping rate, $k_{tb}$ is the trap recombination rate of electrons with electrolyte and $k_d$ is the detrapping rate. It is crucial to note that $k_d$ is not a constant, but depends on the trap energy $E_T$ as it is given by $k_d = k_t N_c e_{et}/N_{t0}$, where $e_{et} = \exp\left[[-(E_C - E_T)]/(k_B T)\right]$ as there is a distribution of traps in DSSCs [29, 75].

At steady-state conditions the rate of trapping at any given point in the $TiO_2$ film must be equal to the rate of detrapping at that same point. Thus the generation and capture terms for the exchange of carriers between band and trap states cancel out and so the trapping and detrapping can be left out of the continuity equation 3.3. As a result the presence of trap states cannot have any effect on steady-state characteristics of the cell, such as the electron diffusion length.

The traps are described satisfactorily in terms of an energy-dependent distribution equation,

$$g(E_T) = \frac{N_{t0}\beta}{k_B T}\exp\left(-\frac{\beta\left(E_C - E_T\right)}{k_B T}\right), \tag{3.6}$$

where the factor $\beta$ represents the rate at which the trap distribution falls off into the bandgap [58, 59, 69, 76].

The angular brackets in equation 3.5 represent the averaging over the trap distribution, equation 3.6, as $\langle f \rangle$ is given by,

$$\langle f \rangle = \int_{E_{Fneq}}^{E_C} dE_T g(E_T) f(E_T) \tag{3.7}$$

If f is approximated by a low temperature stepfunction in equation 1.1, the density of the trapped electrons is given by [29, 59, 69, 76],

$$n_t \simeq \frac{N_{t0}}{N_c}\left[\exp\left(-\beta\frac{(E_C - E_{Fn})}{k_B T}\right) - \exp\left(-\beta\frac{(E_C - E_{Fneq})}{k_B T}\right)\right] = \frac{N_{t0}}{N_c}\left[\left(\frac{n_c}{N_c}\right)^{\beta} - \left(\frac{n_{eq}}{N_c}\right)^{\beta}\right] \tag{3.8}$$

### 3.3.1 Boundary conditions

At the anode, that is, $x = 0$

$$\frac{n_t}{N_c} \approx D_0 \frac{\partial n_c}{\partial x}\bigg|_{x=0} = k_{ext}(n_c - n_{eq}) \tag{3.9}$$

At the cathode i.e. $x = d$

$$\frac{\partial n_c}{\partial x}\bigg|_{x=d} = 0 \tag{3.10}$$

where $k_{ext}$ is the electron extraction rate constant at the substrate $x = 0$ and $d$ is the film thickness. The short circuit photocurrent or IMPS solution is obtained by allowing $k_{ext}$ to be large [29, 56, 57, 58, 59, 60, 67], while the photovoltage or IMVS solution is obtained by setting $k_{ext}$ to be zero.

The first boundary condition states that, the electron extraction rate at the anode ($x = 0$) is first order in the local electron concentration. The second boundary condition indicates that at the cathode side of the $TiO_2$ ($x = d$) no electron concentration gradient exists.

During the IMPS and IMVS measurements the cell is illuminated with the sinusoidally modulated light with a small ac component (10% of the dc component). We assume a small modulation $\delta \ll 1$ of the steady states incident light intensity $I_{0ss}$, at a fixed angular frequency ($\omega = 2\pi$f) given by [29, 60, 62, 77],

$$I_0 = I_{0ss} + \delta I_0 \exp(i\omega t) \tag{3.11}$$

which will result in a modulation of the steady state conduction electron density $n_{css}$ given by,

$$n_c = n_{css} + \delta n_c \exp(i\omega t) \tag{3.12}$$

and of the steady state trap occupation probability $f_{ss}$ given by,

$$f = f_{ss} + \delta f \exp(i\omega t). \tag{3.13}$$

For a modulated incident light intensity, equation 3.3 and 3.5 becomes respectively,

(ignoring terms greater than 1st order in $\delta n$ and $\delta f$)

$$i\omega\delta n_c = D_0\frac{\mathrm{d}^2\delta n_c}{\mathrm{d}x^2} - k_b\delta n_c + \alpha\delta I_0\exp(-\alpha x) - i\omega N_{t0} < \delta f > \ . \tag{3.14}$$

$$\frac{i\omega N_{t0}}{N_c k_t}\delta f = (1 - f_{ss} - \delta f)\left(\frac{n_c}{N_c} + \frac{\delta n_c}{N_c}\right) - e_{et}\,(f_{ss} + \delta f) \tag{3.15}$$

Hence

$$\frac{\delta f}{\delta n_c} = \frac{1}{N_c}\frac{(1 - f_{ss})}{\left[\frac{i\omega N_{t0}}{N_c k_t} + \frac{n_c}{N_c} + e_{et}\right]} \tag{3.16}$$

From equations 3.7 and 3.8 it follows that

$$\frac{\delta n_t}{N_c} = \frac{N_{t0}}{N_c}\left\langle\frac{\delta f}{\frac{\delta n_c}{N_c}}\right\rangle\frac{\delta n_c}{N_c} \tag{3.17}$$

Rewriting eqn 3.14,

$$\frac{\mathrm{d}^2\delta n_c}{\mathrm{d}x^2} - \gamma^2\delta n_c + \frac{\alpha\delta I_0 e^{-\alpha x}}{D_0} = 0 \tag{3.18}$$

where

$$\gamma^2 = \frac{1}{D_0}\left\{i\omega + k_{cb}\left\langle\frac{(1 - f_{ss})(i\omega N_{t0}/k_t)}{\left[\frac{i\omega N_{t0}}{k_t N_c} + \frac{n_c}{N_c} + e_{et}\right]}\right\rangle\right\} \tag{3.19}$$

Since $\gamma$ varies with $x$, at short circuit, equation 3.18 can be solved numerically. The Numerical Recipes routine solvde was used to solve the equation.

The photocurrent conversion efficiency is given by,

$$\Phi(\omega) = \frac{D_0}{\delta I_0}\frac{\partial\delta n_c}{\partial x}\bigg|_{x=0} \tag{3.20}$$

### 3.3.2 Photovoltage

The quasi Fermi level ($E_{Fn}$) is defined through the electron conduction band density as,

$$n_c = N_c \exp \frac{-(E_c - E_{Fn})}{k_B T} \tag{3.21}$$

where $N_c$ is the density of the conduction band of states in the $TiO_2$ semiconductor, $E_c$ is the conduction band energy.

In the dark, at equilibrium, the conduction band electron density is determined by the dark Fermi level ($E_{Fneq}$) and is given by,

$$n_{eq} = N_c \exp \frac{-(E_c - E_{Fneq})}{k_B T} \tag{3.22}$$

The photovoltage ($U_{photo}$) or the open circuit voltage ($V_{oc}$) is defined simply as the difference between the quasi Fermi level ($E_{Fn}$) of the $TiO_2$ and the dark Fermi level ($E_{Fneq}$),

$$qV_{oc} = E_{Fn} - E_{Fneq} \tag{3.23}$$

so that the pertubation in photovoltage $\delta U_{photo}$ calculated at open circuit

$$\delta U_{photo} = \frac{k_B T}{q} \ln \left(1 + \frac{\delta n_c}{n_c}\right) \tag{3.24}$$

From equation 3.3, within the multiple trapping model, $n_c \propto I_0$. At open circuit, in the steady state where $\partial n_c/\partial t = \partial n_t/\partial t = 0$, $n_c$ does not vary significantly with position $x$ so the term $\propto D_0$ can be neglected. Thus, if we assume in equation 3.3 that $\exp(\alpha x) \approx 1$ throughout the device,

$$\alpha I_0 \approx k_{cb} n_c \quad \Rightarrow \quad n_c \approx \frac{\alpha I_0}{k_{cb}} \tag{3.25}$$

## 3.4 Quasi static model

When a dye sensitized solar cell (DSSC) is perturbed away from equilibrium, for example by a short pulse of light, the timescale of the relaxation of free carriers is not only determined by the values of $D_0$ and $\tau_0$, but also by the trapping and detrapping

terms in the continuity equation 3.3. If the trapping and detrapping processes are very fast with respect to free carrier relaxation processes (transport and recombination), an approximate equilibrium between free and trapped electron carriers is maintained even when the system as a whole is perturbed away from equilibrium, this is known as the quasi static approximation. Bisquert and Vikhrenko [78] have introduced the quasi-static assumption that the free and trapped electrons remain essentially in a local equilibrium, even when the system is displaced away from equilibrium by some perturbation.

The quasi-static condition relates the time dependence of the conduction band electron density $\frac{\partial n_c}{\partial t}$ in the noncrystalline $TiO_2$ film to the corresponding rate of change of the density of trapped electrons $\frac{\partial n_t}{\partial t}$, by

$$\frac{\partial n_t}{\partial t} = \frac{\partial n_t}{\partial n_c}\frac{\partial n_c}{\partial t} \tag{3.26}$$

Then equation 3.3 in the absence of a generation term can be witten as,

$$\frac{\partial n_c}{\partial t} = D_n \frac{\partial^2 n_c}{\partial x^2} - \frac{n_c - n_{eq}}{\tau_n} \tag{3.27}$$

where

$$D_n = \left(1 + \frac{\partial n_t}{\partial n_c}\right)^{-1} D_0 \approx \left(\frac{\partial n_t}{\partial n_c}\right)^{-1} D_0 \tag{3.28}$$

and

$$\tau_n = (1 + \frac{\partial n_t}{\partial n_c})\tau_0 \approx (\frac{\partial n_t}{\partial n_c})\tau_0 \tag{3.29}$$

This approximation is only valid if $D_n$ does not vary with $x$. The reason is that the more general form of the continuity equation in the absence of recombination is,

$$\frac{\partial n_c}{\partial t} = \frac{\partial J_n}{\partial x} - \frac{n_c - n_{eq}}{\tau_n} \tag{3.30}$$

where $J_n = -D_n \frac{\partial n_c}{\partial x}$. If $D_n$ varies with $x$, $\frac{\partial J_n}{\partial x} \neq D_n \frac{\partial^2 n_c}{\partial x^2}$. Since $D_n$ varies with $n_c$ $(x)$ this problem occurs at short circuit, see figure 3.2, (A). This problem does not exist when finding the photovoltage since at open circuit the charge density is independent of $x$ to a very good approximation, see figure 3.2 (B). We address this problem by solving the continuity equation for a fixed free charge density ($n_{cqs}$) equal to the charge

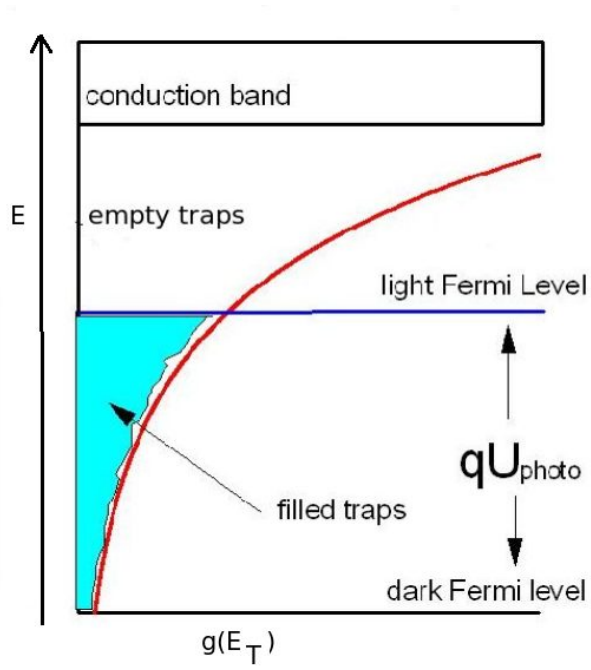


Figure 3.1: Graphical illustration of density of the electron trap distribution g($E_T$), illustrating the exponential distribution of traps in DSSCs.

density at a constant quasi Fermi level which is equal to the average quasi Fermi level, that is,

$$n_{cqs} = N_c e^{\left(\frac{-(E_C - E_{Fnav}}{k_B T}\right)} \tag{3.31}$$

where $E_{Fnav}$ is the average quasi Fermi level.

With this assumption the expressions derived by Dloczik *et al.* [60], for $\Phi$ can be used with $D_0$ replaced by $D_{nqs}$ where

$$D_{nqs} = D_0 \frac{n_c}{n_t}\bigg|_{n_c = n_{qs}} \tag{3.32}$$

where $D_{nqs}$ effective diffusion coefficient calculated from the quasistatic approximation. The expressions for $\Phi$ are given in section B.3 of Appendix B for substrate and electrolyte side illumination.

Figure 3.1 illustrates the density of electron trap states in the $TiO_2$ which appear to be distributed exponentially in energy [75]. In general, the density of electrons in the conduction band is many orders of magnitude lower than the density of trapped electrons. Although electron transport and electron transfer involve conduction band electrons,

dynamic measurements of photocurrent and photovoltage are strongly influenced by trapping/detrapping since the trap occupation responds to changes in the density of electrons or the change in the electron quasi Fermi level in the conduction band [75]. In this work we account for the trapping and detrapping of electrons as illustrated in equation 3.3.

## 3.5 Results

The parameter values common to all the figures are $I_0 = 3.08 \times 10^{20}$ m$^{-2}$s$^{-1}$ $T = 293$K, $D_0 = 0.4$ cm$^2$ s$^{-1}$, $d = 13$ $\mu$m, $\alpha = 5.3{\times}10^4$ m$^{-1}$, $T = 293$K, $T_c = 1090$K, $k_t = 1 \times 10^{10}$ s$^{-1}$, $N_c = 1 \times 10^{26}$m$^{-3}$, $N_{t0} = 1 \times 10^{27}$ m$^{-3}$, $\tau_0 = 4 \times 10^{-5}$ s and $k_{ext} = 1 \times 10^3$ ms$^{-1}$, unless indicated on the figure captions. These values were chosen to be consistent with the parameter values used in [29, 68] and to maximize agreement with experimental data.

The electron density profiles for short circuit and open circuit conditions are illustrated in figure 3.2. Figure 3.2, (A), demonstrates the profile of the short circuit electron density gradient that drives the electrons to the anode. At short circuit the photocurrent is determined by the exponential trap distribution at the anode where the electron density is much lower compared with its value at the cathode side. The profiles have the same shape for different values of intensity, as illustrated on the figure 3.2, (A). Figure 3.2, (B), illustrates the electron density profile at open circuit and it can be noted that the profiles scale linearly with intensity, since the free electron life time is independent of intensity under open circuit [29]. Thus from the two figures of the electron density profiles, under open circuit conditions the concentration of electrons is much higher compared to its maximum value under short circuit conditions at the same intensity.

### 3.5.1 Electron trapping rate constant

The electron trapping rate constant ($k_t$) is one of the most important parameters of the modelling. In figures 3.3 and 3.4, the characteristic plots of photocurrent response ($\Phi$) are presented, for different values of the electron trapping rate. As illustrated in figure 3.3 for the lower values of $k_t$, we observe several behaviours in the IMPS responses. The reason for the different spectra is competition between trapping and recombination. It is clear from figure 3.3 that the minimum angular frequency ($\omega_{min}$) varies with $k_t$. This will affects transition time ($\tau_{tr}$) and hence the effective diffusion coefficient of electrons to the anode as illustrated by equation 3.33. As illustrated in figure 3.4, $\omega_{min}$ for higher

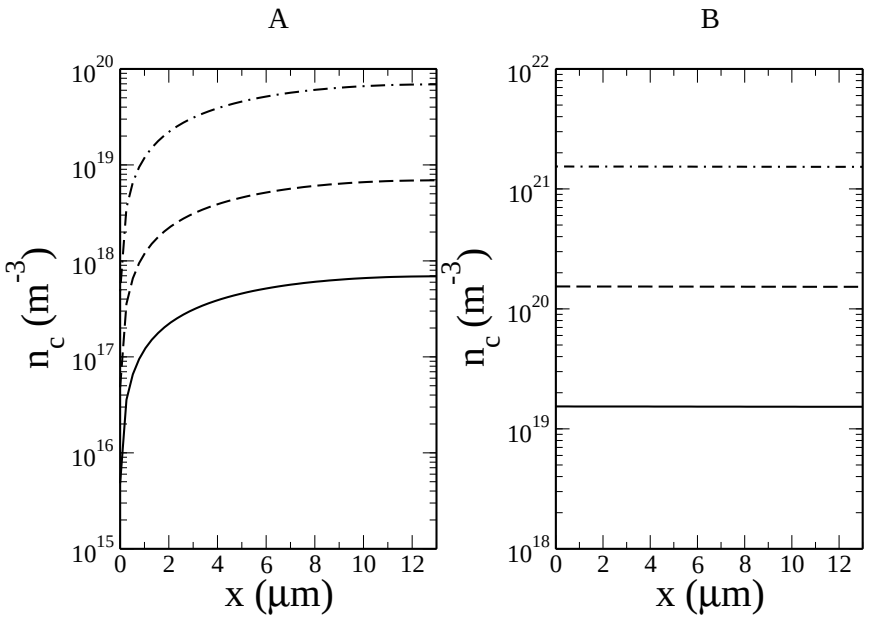


Figure 3.2: Short (A) and open (B) circuit electron density profile for illumination from substrate side, for the intensity $I_0 = 1 \times 10^{19}$ $m^{-2}s^{-1}$ (solid line), $I_0 = 1 \times 10^{20}$ $m^{-2}s^{-1}$ (dashed line) and $I_0 = 1 \times 10^{21}$ $m^{-2}s^{-1}$ (dash-dot line) respectively.

trapping rate is almost on the same position. For higher values of $k_t$, for example $1 \times 10^{11}$ $s^{-1}$ and $1\times 10^{12}$ $s^{-1}$ we observe a limit in the trapping rate constant as the two values of $k_t$ give similar IMPS responses, especially at lower frequencies. For this work $k_t$ was taken as $1 \times 10^{10}$ as it was found to give IMPS response which agrees well with the experimental IMPS results. As illustrated on the figure 3.4, it can be observed that for a lower value of trapping rate, the response is higher compared to a large value of the trapping rate.

The IMPS response transient time ($\tau_{tr}$) is related to the film thickness, $d$ and $D_n$ by,

$$\tau_{tr} = \frac{1}{\omega_{min}} = \frac{d^2}{\zeta D_n} \tag{3.33}$$

where $\zeta$ is a numerical factor which depends upon the layer thickness and the direction of illumination [19, 29, 79].

Figure 3.5 illustrates the dependence of the transient time ($\tau_{tr}$) on the electron trapping rate. As demonstrated in the figure, $\tau_{tr}$ decreases with an increasing $k_t$. At the higher value of the trapping rate, $\tau_{tr}$ is almost independent of the trapping rate. This follows from the observation above that at higher values of the trapping rate, the IMPS

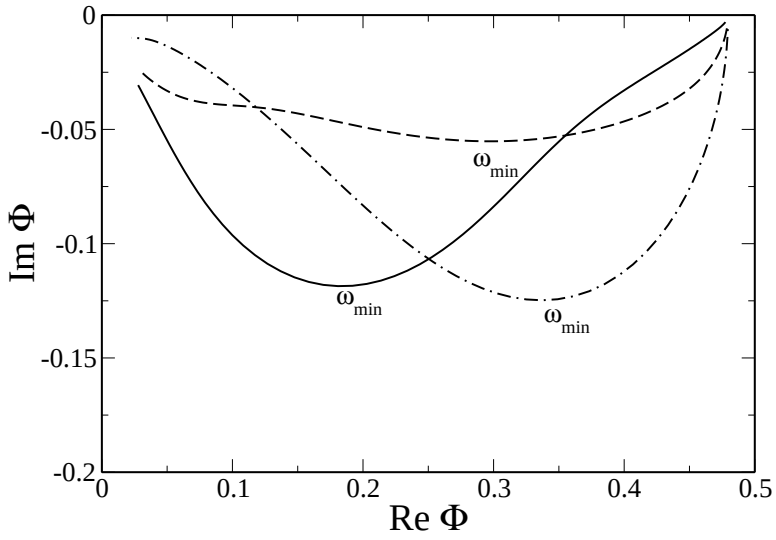


Figure 3.3: Im ($\Phi$) vs Re($\Phi$) for different electron trapping rate, $k_t = 1 \times 10^6$ s$^{-1}$ (solid line), $k_t = 1 \times 10^7$ s$^{-1}$ (dashed line), $k_t = 1 \times 10^8$ s$^{-1}$ (dash-dot line), for substrate side illumination.

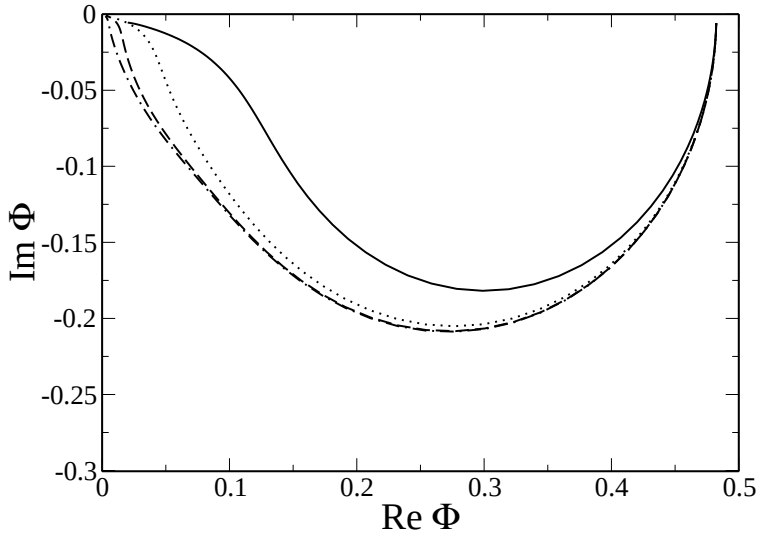


Figure 3.4: Im ($\Phi$) vs Re($\Phi$) for different electron trapping rate, $k_t = 1 \times 10^9$ s$^{-1}$ (solid line),$k_t = 1 \times 10^{10}$ s$^{-1}$ (dotted line), $k_t = 1 \times 10^{11}$ s$^{-1}$ (dashed line), $k_t = 1 \times 10^{12}$ s$^{-1}$ (dash dot line) for substrate side illumination.

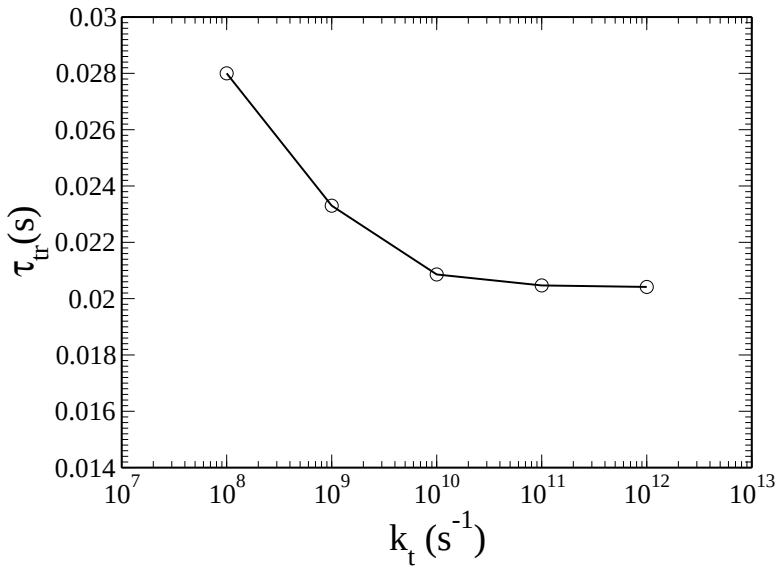


Figure 3.5: Dependence of the transient time ($\tau_{tr}$) on the electron trapping rate ($k_t$), for substrate side illumination.

response is almost similar at lower frequencies and hence the $\tau_{tr}$ will be constant as it is obtained from the minimum angular frequency ($\omega_{min}$) of the IMPS responses.

### 3.5.2 Short and open circuit quasi Fermi level

Figure 3.6 illustrates the simulated short circuit and open circuit quasi Fermi levels ($E_{Fn}$). It can be observed from the figure that the short circuit $E_{Fnsc}$ is lower that the open circuit $E_{Fnoc}$. This can be noted from the fact that, the short circuit electron density is lower than the open circuit electron density, see figure 3.2. The short circuit electron density and the short circuit quasi Fermi level vary with position, while the open circuit electron density and quasi Fermi level are independent of position. At short circuit the electron quasi Fermi level is determined by the balance between the electron injection and transport to the anode contact and electron transfer to the $I_3^-$ is neglected, but at open circuit the quasi Fermi level is given by the balance between electron injection to the $TiO_2$ and transfer to $I_3^-$. The main objective of this work is to show that in the multiple trapping model the free electron diffusion length ($L_0$) is almost equal to the effective diffusion length ($L_n$), provided the difference between the open and short circuit quasi Fermi levels is taken into consideration. This is achieved by calculating the second intensity ($I_{0oc}$) to align the open circuit quasi Fermi level ($E_{Fnoc}$) to the average short circuit quasi Fermi level ($E_{Fnscav}$) as discussed in section

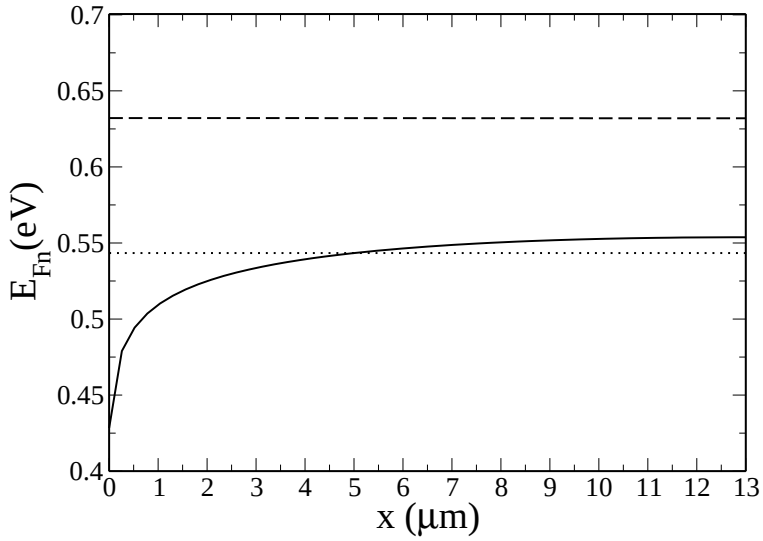


Figure 3.6: Short circuit (solid line), average short circuit (dotted line) and open circuit (dashed line) quasi Fermi profile for substrate side illumination, $I_0 = 3.08 \times 10^{20}$ $m^{-2}s^{-1}$.

3.5.3 below. $I_{0sc} = 3.08 \times 10^{20}$ $m^{-2}s^{-1}$ was used as the original intensity to calculate $E_{Fnsc}$, $E_{Fnscav}$(0.5444 eV) and $E_{Fnoc}$ (0.6321 eV). The shift required to align $E_{Fnscav}$ and $E_{Fnoc}$ is $\Delta E_{Fn} = 0.0877$ eV (the difference between $E_{Fnoc}$ and $E_{Fnscav}$) and the calculated second intensity, $I_{0oc} = 9.56 \times 10^{20}$ $m^{-2}s^{-1}$.

As reported by Jennings *et al.* [29] there are many different ways to calculate the average or mean short quasi Fermi level values. They argued that, $E_{Fnscav}$ values can be calculated from the integrated free electron density, trapped electron density and the average value of the $E_{Fn}$ from the continuity equation. In this work the average short circuit $E_{Fnsc}$ was obtained by using the average value of the $E_{Fn}$ from the continuity equation and this was compared to the values obtained by the integrated free electron density as reported by Jennings and we found that the two methods gives nearly the same value of the average short circuit $E_{Fnsc}$. This is clearly illustrated in figure B.1, in Appendix B.

The difference between the electron $E_{Fn}$ under open and short circuit conditions is the key issue in this work, since the electron transport is measured under short circuit conditions and the electron transfer to $I_3^-$ is characterized under the open circuit condition. The transport of electrons is characterized by $D_n$ and electron recombination is characterized by $\tau_n$ extracted using the IMPS and IMVS responses respectively and hence to obtain the correct value of the effective diffusion length $D_n$ and $\tau_n$ must be

calculated at the same $E_{Fn}$.

### 3.5.3 Determination of second intensity ($I_{0oc}$)

As shown in figure 3.6, we can align $E_{Fnscav}$ and $E_{Fnoc}$ by either shifting $E_{Fnoc}$ to $E_{Fnscav}$, or by shifting $E_{Fnscav}$ to $E_{Fnoc}$. For consistency in this work $E_{Fnoc}$ was shifted down to $E_{Fnscav}$.

The electron density ($n_c$) is given by,

$$n_c = N_c \exp \frac{-(E_c - E_{Fn})}{k_B T} \tag{3.34}$$

and since it is directly proportional to intensity we can assume that,

$$\frac{\alpha I_{0sc}}{k_{cb}} = N_c \exp \frac{-(E_c - E_{Fnsc})}{k_B T} \tag{3.35}$$

and

$$\frac{\alpha I_{0oc}}{k_{cb}} = N_c \exp \frac{-(E_c - E_{Fnoc})}{k_B T} \tag{3.36}$$

dividing equation 3.35 by 3.36 and solving for $I_{0oc}$, we get

$$I_{0oc} = I_{0sc} \exp \frac{(E_{Fnsc} - E_{Fnoc})}{k_B T} \tag{3.37}$$

where $E_{Fnscav}$ is the average short circuit quasi Fermi level value, $E_{Fnoc}$ is the open circuit quasi Fermi level value and $(E_{Fnscav} - E_{Fnoc})$ gives the difference between the short and open circuit quasi Fermi level at the original intensity $I_{0sc}$.

After calculating the second intensity ($I_{0oc}$), we determine the open circuit quasi Fermi level, which correspond to the average short circuit quasi Fermi level. This gives a way to calculate $\tau_n$, which corresponds to $D_n$ at the same quasi Fermi level. The value of second intensity ($I_{0oc}$), is lower than the initial intensity, which is in line with the fact that we are shifting down the open circuit quasi Fermi level ($E_{Fnoc}$) to a lower value corresponding to the short circuit $E_{Fnsc}$ value. As mentioned above, we can also shift the short circuit quasi Fermi level to the same point as the open circuit quasi Fermi level, which in turn gives a higher value of the second intensity as it depend on the sign

of the arguments in equation 3.37.

### 3.5.4 Determination of effective electron diffusion coefficient and life time

Using the two different intensities ($I_{0sc}$ and $I_{0oc}$) values we now calculate $D_n$ and $\tau_n$ at the same quasi Fermi level respectively. Figure 3.7 shows the real and imaginary part of the photocurrent (A) and photovoltage (B) responses calculated from the full numerical model where trapping and detrapping of electrons are considered. The values of $D_n$ is extracted from the IMPS responses and $\tau_n$ is extracted from the IMVS responses. The effective electron diffusion coefficient is related to the transient time ($\tau_{tr}$), which defines the electron transport from the $TiO_2$ to the anode, given by the inverse of the minimum angular frequency ($\omega_{min}$) where $\omega_{min}$ is defined as the minimun angular frequency of the imaginary IMPS or IMVS response respectively. From equation 3.33, the effective diffusion coefficient can be obtained as,

$$D_n = \frac{\omega_{min} d^2}{\zeta} \tag{3.38}$$

where $\zeta$ is the numerical factor which depends upon the layer thickness and the direction of illumination [19, 29, 79]. To validate the value of $\zeta$, simulations were done using the quasistatic assumption to calculate the value of $D_n$, and the corresponding $\omega_{min}$ from its IMPS response. This is discussed in detail in appendix B. The calculation was done for the film thickness of 13 $\mu$m and we obtained a value of $\zeta = 2.7486$ and $\zeta = 2.433$ for substrate and electrolyte side illumination respectively. Our electrolyte side values agree well with the values reported by Jennings *et al.* [29].

The effective electron life time ($\tau_n$) is calculated at open circuit, where we get the IMVS response as shown in figure 3.7 graph B, this is achieved by setting $k_{ext} = 0$ in equation 3.9. The effective electron life time is related to the minimum angular frequency ($\omega_{min}$) of the IMVS by,

$$\tau_n = \frac{1}{\omega_{min}} \tag{3.39}$$

The calculated value of $D_n$ and $\tau_n$ are different from $D_0$ and $\tau_0$ and are intensity dependent as indicated in figure 3.8, (A) and (B). $D_n$ increases with an increase in the intensity and $\tau_n$ decreases with an increase in the intensity. The intensity dependence arises from the influence of electron trapping/detrapping on the dynamic photocurrent

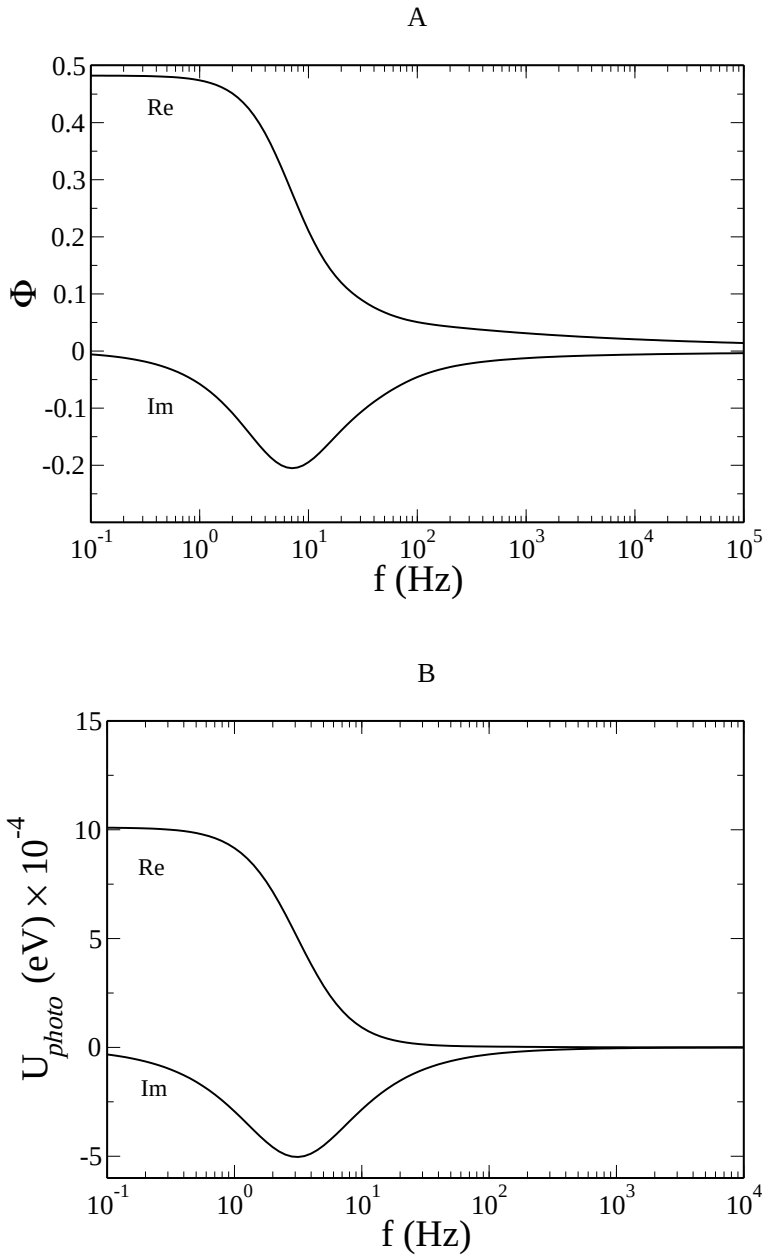


Figure 3.7: Typical full numerical IMPS (A) and IMVS (B) response for illumination from substrate side.

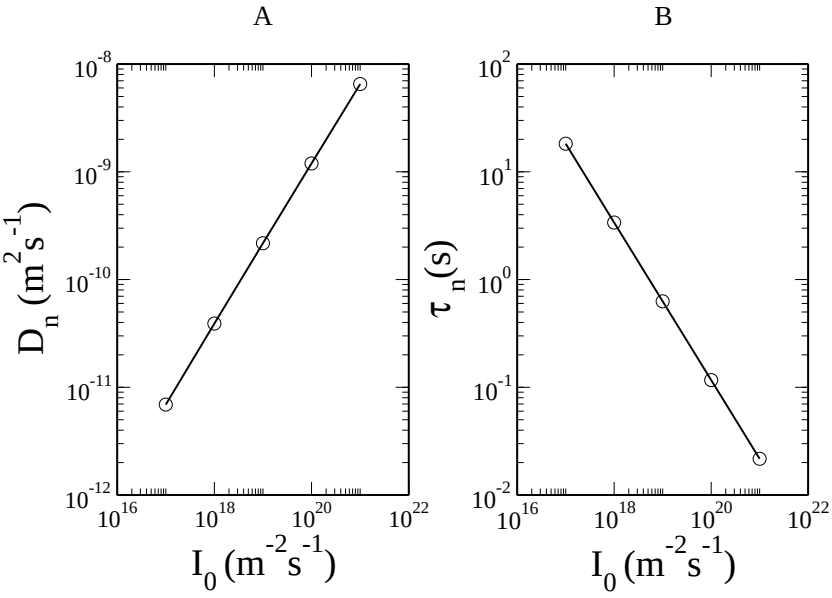


Figure 3.8: Intensity dependence of the effective electron diffusion coefficient and life time

and photovoltage responses [75]. This is clearly shown in figure 3.1. As we increase the intensity the electron quasi Fermi level increases and hence the filled trap states level. The electrons most likely to detrap come from the topmost occupied level. As this level approaches the conduction band, the detrapping time decreases rapidly, so the electrons take less time to diffuse through the $TiO_2$ film.

The intensity dependence of $D_0$ and $\tau_0$ shows that IMVS and IMPS can be used to determine $\tau_n$ and $D_n$ in DSSCs for a wide range of intensities. The intensity dependence of $D_n$ indicates that electron transport in DSSCs is influenced by trapping and detrapping of electrons from a distribution of trapping levels that are probably located at the surface of the $TiO_2$ particles [80]. In general, it is understood that under practical operating conditions, $D_n \ll D_0$ and $\tau_n \gg \tau_0$ [29]. In the multiple trapping model, the effective diffusion coefficient varies with distance from the fact that at short circuit conditions, the free electron density and electron quasi Fermi level vary with the distance and fall steeply close to the anode. This can also be observed from figure 3.2, graph A, which shows the profile of the short circuit free electron density.

Figure 3.9 illustrates the intensity dependency of $\tau_{tr}$ of the IMPS responses. As shown in the figure $\tau_{tr}$ decreases with increasing intensity. The $\tau_{tr}$ gives the average time for collection of photoinjected electrons at the anode. This dependence of $\tau_{tr}$ is due to the fact that, as the intensity increases, the rate of electron transport increases as there is an increase in the photoinjected electrons. This is clearly illustrated from equation

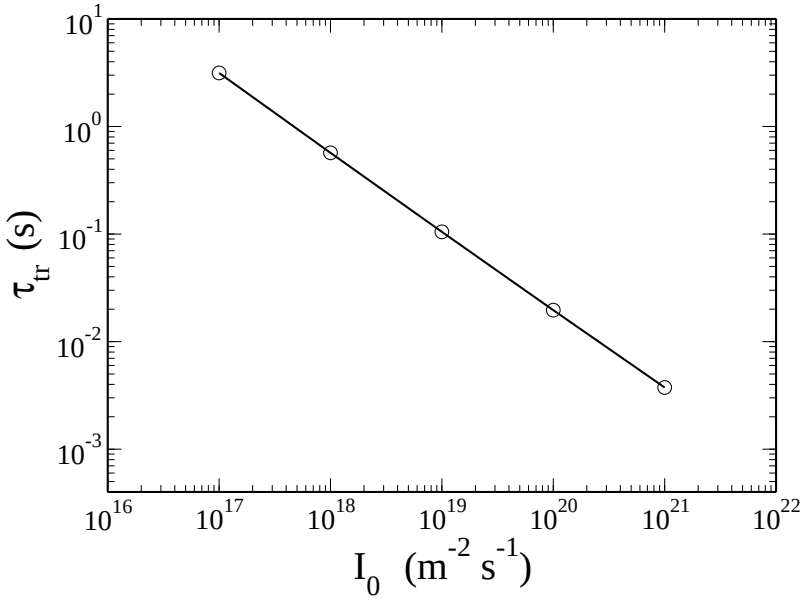


Figure 3.9: Intensity dependence of transition time ($\tau_{tr}$).

3.38 which shows that as $\omega_{min}$ increases $D_n$ will also increase and hence $\tau_{tr}$ decreases.

## 3.6 Comparison of the different models

As a way of illustrating that our extracted values of the effective electron diffusion coefficient from the multiple trapping model agree with the other model, $D_n$ values were calculated using the quasistatic model developed by Bisquert and Vikhrenko, see section 3.4. $D_n$ from the full numerical solution is shown on figure 3.10. A comparison with $D_n$ from the quasistatic model is also provided. There is good agreement between the two sets of values. The slight difference could be because in the quasi static model it is assumed that when the solar cell is displaced away from equilibrium by illumination, the trapping and detrapping takes place very fast and the equilibrium is maintained, it is necessary to use the average value of free electron density, while the full numerical model takes into account that at short circuit the free electron density varies with distance.

To further illustrate the importance of the multiple trapping model assumption that, $D_n$ at short circuit varies with position, the IMPS response calculated from the quasistatic model is compared to the full numerical solution. As illustrated in figure 3.11, there is a good agreement between the quasistatic and full numerical IMPS responses,

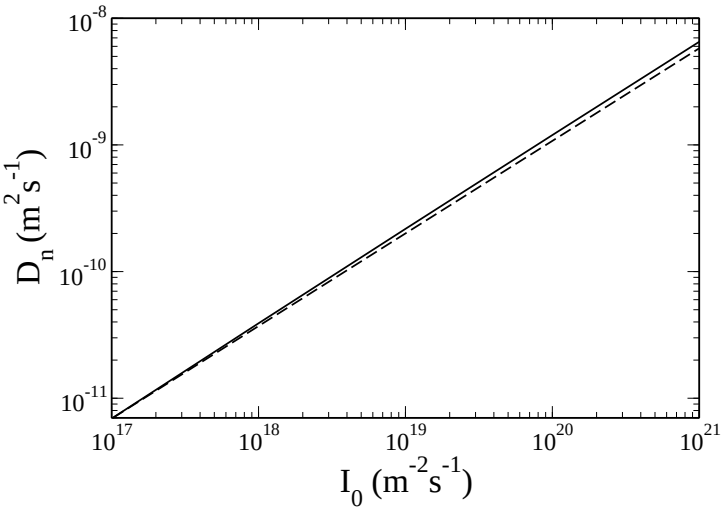


Figure 3.10: Comparison of the effective diffusion coefficient calculated from the full numerical $\omega_{min}$ (solid line) and from the quasi static (dashed line) approach at different intensities.

especially at lower frequency and they begin to deviate at high frequency, near $\omega_{min}$. Our full numerical solution is reproduced well by the the quasistatic model. This agreement validates the assumption made in the quasistatic model that the trapping and detrapping processes occur sufficiently fast that the system behaves as though it is in equilibrium with a well defined quasi-Fermi level determined by the electron density at that point. The deviation of the quasistatic model from the full numerical solution, even at lower frequency, fulfills the fact that in the full numerical model $D_n$ varies with position and depends on the account of the trapping and detrapping of electron as also reported by Peter [75].

## 3.7 Estimation of the electron diffusion length

The effective electron diffusion length can be calculated by taking the square root of the product of the effective diffusion coefficient and life time, at the same value of the quasi Fermi level. This approach does not underestimate the value of $L_n$ as it has taken into account the difference between the short and open circuit quasi Fermi levels. Overall we would like to stress that if the difference between the short circuit and open circuit quasi Fermi level is taken into consideration, the effective and free electron diffusion lengths are almost equal, that is,

$$L_n = \sqrt{D_n \tau_n} \simeq L_0 = \sqrt{D_0 \tau_0}. \tag{3.40}$$

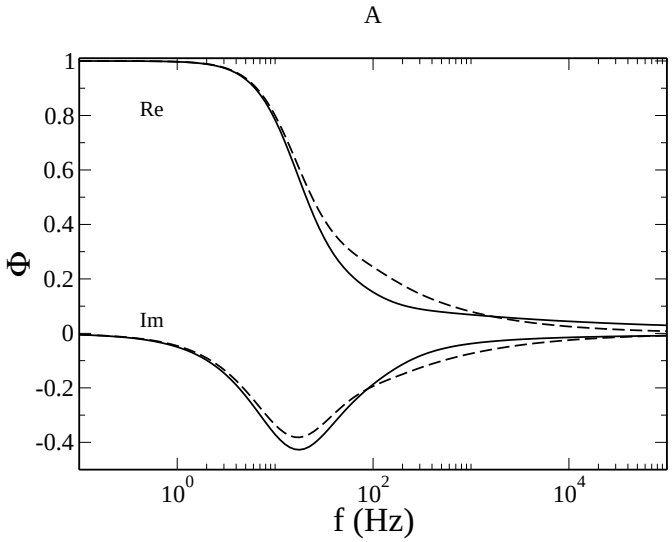


Figure 3.11: IMPS response for the multiple trapping model (solid line), quasistatic model (dashed line) for a 13 $\mu$m DSSC.

| $\tau_0$ (s) | $D_n$ ($m^2s^{-1}$) | | $\tau_n$ (s) | |
|---|---|---|---|---|
| | SE | EE | SE | EE |
| $4 \times 10^{-5}$ | $2.37\times10^{-9}$ | $2.95\times10^{-9}$ | 0.740 | 0.668 |
| $1 \times 10^{-5}$ | $2.85\times10^{-9}$ | $3.22\times10^{-9}$ | 0.198 | 0.182 |
| $2.5 \times 10^{-6}$ | $3.21\times10^{-9}$ | $3.44\times10^{-9}$ | 0.063 | 0.060 |

Table 3.1: Extracted value of $D_n$ and $\tau_n$ for different values of $\tau_0$ for substrate (SE) and electrolyte (EE) side illumination.

Simulations were performed for three values of $L_0$, obtained by varying $\tau_0$ while fixing $D_0$ at the value listed at the start of this section. As discussed above the extraction of $D_n$ and $\tau_n$ from the IMPS and IMVS respectively for illumination from substrate (SE) and electrolyte (EE) at the same quasi Fermi level was followed and values of $D_n$ and $\tau_n$ are calculated using the $\omega_{min}$ from both the IMPS and IMVS of the full numerical solution. Table 3.1 shows the $\tau_0$ values used to obtain different $L_0$ and the corresponding extracted values of $D_n$ and $\tau_n$.

In support of the argument that $L_0 \simeq L_n$, values of $L_0$ and $L_n$ for substrate (SE) and electrolyte (EE) side illumination are shown on table 3.2. Table 3.2 compares the $L_0$ from Table 3.1 with the values of $L_n$ calculated using $D_n$ and $\tau_n$ respectively. It is clear from table 3.2, that if the difference between the open circuit and short circuit quasi Fermi level is taken into consideration, $L_0$ is close to $L_n$. This result shows that the procedure used to calculate $L_n$, by considering the difference between the short circuit and open circuit $E_{Fn}$ [29, 75], is in good agreement with the quasistatic model

| $L_0$ ($\mu$m) | $L_n$ ($\mu$m) | |
|---|---|---|
| | SE | EE |
| 40 | 41.88 | 44.39 |
| 20 | 23.75 | 24.21 |
| 10 | 14.22 | 14.37 |

Table 3.2: Comparison between $L_0$ and $L_n$ extracted from different values of $D_0$,$\tau_0$ and ($D_n$,$\tau_n$) respectively for substrate (SE) and electrolyte (EE) side illumination, given in table 3.1.

prediction that $L_0$ and $L_n$ must be equal. The values of $L_n$ in this study are equal to or greater than the film thickness leading to complete collection of the photogenerated and injected electrons in the external circuit.

The fact that $L_0 \simeq L_n$ means that the free electron diffusion length can be used to characterize the DSSCs. The collection of the photogenerated electrons depends on the competition between the diffusion of electrons into the $TiO_2$ and the recombination with the redox electrolyte. The procedure followed in this work shows that the effective diffusion lengths and free diffusion length are almost equal and greater than the films thickness. The values of $L_n$ in this study are larger than the average film thickness leading to complete collection of the photogenerated and injected electrons in the external circuit.

It is important to note that in the multiple trapping model $D_n$ and $\tau_n$ depend on the trap distribution and on the illumination intensity, but their square root product, $L_n$ is almost independent of intensity [29, 59, 75]. So the effective diffusion length is independent of trap occupancy as also reported by Bailes *et al.* [76].

## 3.8 Comparison with experimental results

An experimental measurement of IMPS was performed by H.Wang at the University of Bath, Department of Chemistry. The IMPS was carried out with a DSSC under short-circuit. The DSSC consisted of a dye (N719) coated $TiO_2$ mesoporous film (13 $\mu$m), and an electrolyte composed of 0.5 M NaI, 0.05 M $I_2$, 0.5M tert-butylpyridine in a solvent mixture of acetonitrile and valeronitrile (85:15, V/V) as well as a thermally platinised counter electrode. A red light emitting diode (LED, 627 nm) was used as the light source to adjust the electron density in the $TiO_2$ film. A 5% of the bias illumination was superposed to the bias illumination through a Solartron 1260 frequency response analyzer. The current generated by the bias illumination was offset with a potentiostat and the current signal from the modulated light was recorded by the potentiostat which

was connected to a computer.

The theoretical predictions and experimental data were scaled to give the same zero frequency intercept on the real axis which should correspond to the steady state IPCE. Figures 3.12 and 3.13 compare the experimental and theoretical IMPS responses calculated using the full numerical and the analytical solutions for substrate side (A) and electrolyte side illumination (B), for two different intensities, $I_0 = 3.08 \times 10^{20}$ $m^{-2}s^{-1}$ and $I_0 = 1.047 \times 10^{21}$ $m^{-2}s^{-1}$ respectively. These results indicate that there is good agreement between modeling and experiment at low frequency and that the value of $\omega_{minIMPS}$ is similar for all three cases. Deviations arise between the models and the experimental data, since the experimental IMPS results are affected by the $RC$ attenuation at high frequency, where $R$ is the series resistance of the contacts and $C$ is the capacitance of the substrate electrode [67, 77, 81, 82]. In electrolyte side illumination, deviations between experiment and theory occur at lower frequencies because a delay is introduced into the electron transport to $TiO_2$, which depends on the illumination side.

## 3.9 Near infrared (IR) response

The electron transient time ($\tau_{tr}$) and recombination time are important parameters to characterize the efficiency of DSSCs as discussed above. Near infrared (IR) absorption method is currently used to study the electron transport in DSSCs [67, 74, 68]. It has been shown that the near IR measurements method provide a simple and reliable way of characterizing the trapped ($n_t$) electron density under variety of experimental conditions [74]. The advantage of this technique is that it allows the measurements of the IR responses for both short and open circuit at the same conditions, that is at pair of intensities ($I_{0sc}$ and $I_{0op}$) where short circuit trapped electron density is the same as the open circut trapped electron density ($n_t$) and hence the quasi Fermi level [68]. This allows $D_n$ and $\tau_n$ to be determined at the same trapped electron density. In this section we show that even when the measurements of the short and open circuit IR responses are done under the same conditions and intensity, their minimum angular frequency ($\omega_{min}$) are not the same.

As discussed above the majority of electrons in the dye sensitized solar cells are trapped and the current is carried by a much lower density of free electrons in the conduction band [76]. The density of the trapped electrons can be measured as a function of trap occupancy by electrical techniques such as impedance [83] and charge extraction [84]. Steady state infrared (IR) transmittance measurements are well established as a way of following electron accumulation in porous $TiO_2$. Transient IR absorption

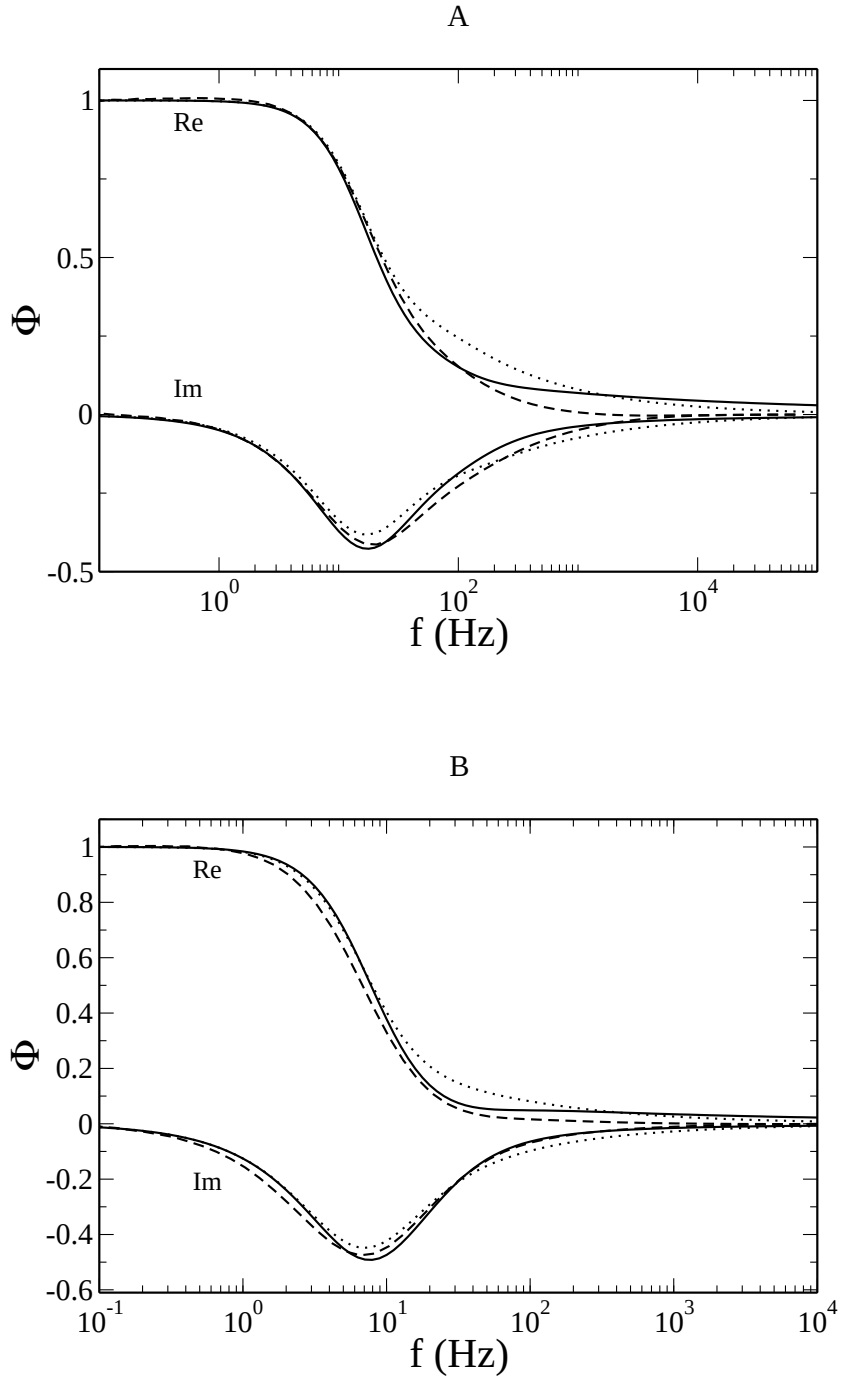


Figure 3.12: Comparison between the experimental (dashed line), multiple trapping model (solid line) and quasistatic model (dotted line) IMPS responses for substrate (A) and electrolyte (B) side illumination, $I_0 = 3.08 \times 10^{20}$ m$^{-2}$s$^{-1}$.

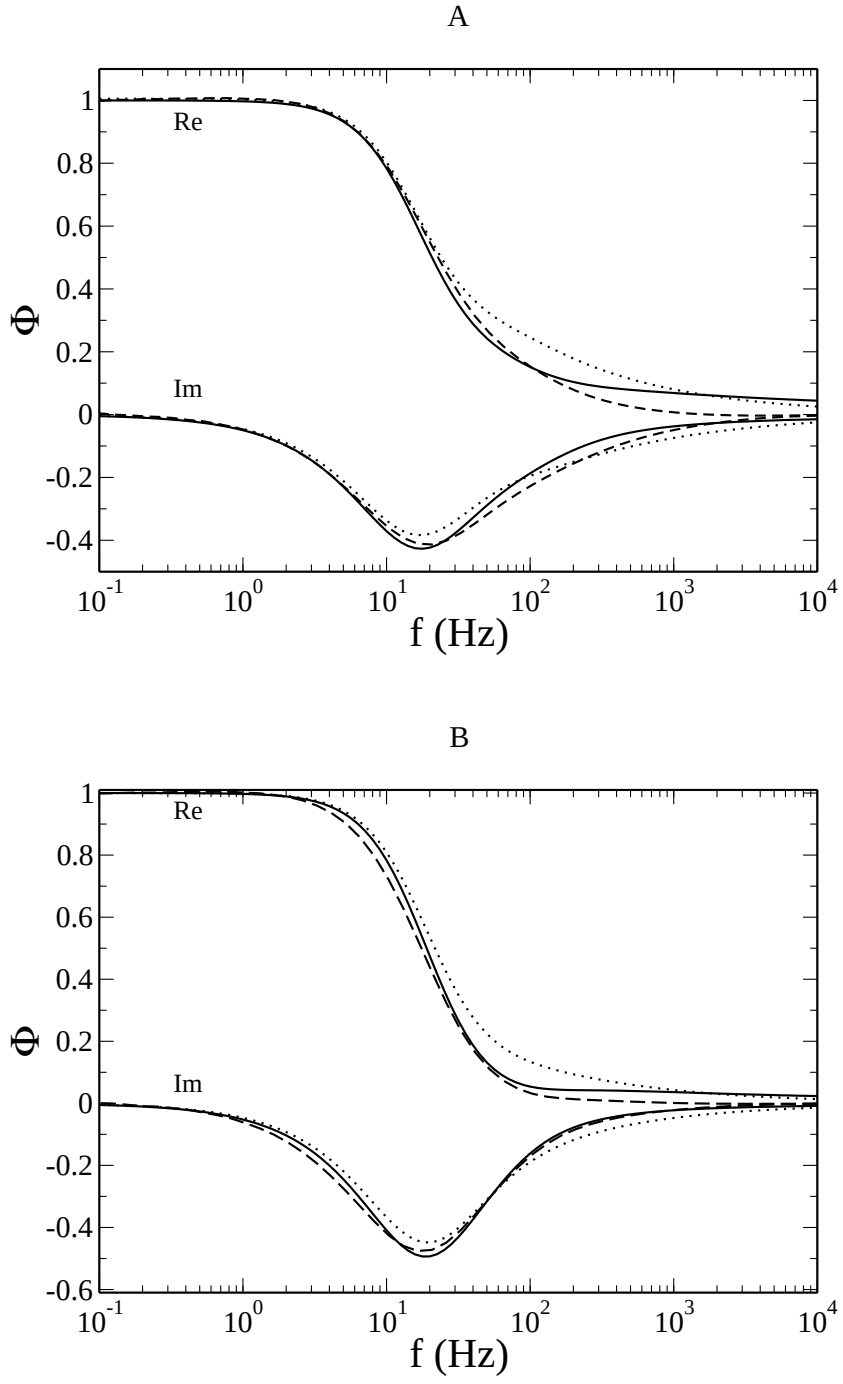


Figure 3.13: Comparison between the experimental (dashed line), multiple trapping model (solid line) and quasistatic model (dotted line) IMPS responses for substrate (A) and electrolyte (B) side illumination, $I_0 = 1.047 \times 10^{21}$ m$^{-2}$s$^{-1}$.

measurements on porous $TiO_2$ and DSSCs have been widely used to follow electron injection and trapping on the pico-second time scale as well as on longer scale. The use of the near-infrared transmittance to follow changes in the density of trapped electrons under different conditions have been described by Nguyen *et al.* [74]. A steady state method of determining the electron diffusion length in dye sensitized solar cells using the near infrared absorption method have been described by Wang and Peter [68]. The advantage of the infrared method, to determine the electron diffusion length is that, the near-infrared method looks at the trapped electron rather than the free electrons. This makes the IR method a convenient way of establishing the trap electron occupancy in DSSCs [68].

As illustrated by Nguyen *et al.* [74] the near-infrared (IR) absorption measurement is a reliable way to measure the trapped electron density . Theoretically the infrared measurements are generally thought to probe the integrated trapped electron density of photogenerated charge carriers throughout the cell. It follows from equation 3.16 that IR responses can be calculated as [85],

$$\frac{\delta Q_t}{N_c} = \frac{N_{t0}}{N_c}\int_0^d \left\langle \frac{1 - f_{ss}(x)}{\left[\frac{i\omega N_{t0}}{N_c k_t} + \frac{nc(x)}{N_c} + e_{et}\right]} \right\rangle \frac{\delta n_c(x)}{N_c} dx \tag{3.41}$$

where $\delta Q_t$ is the infrared response.

The density of trapped electrons under steady state can be predicted theoretically using the following approach. The starting point is the continuity equation, which describes the injection, transport and recombination of electrons in DSSCs. Solution to the continuity equation with appropriate boundary conditions gives the profiles of the free electron density through out the device, see figure 3.2. The quasi Fermi level relative to the conduction band can then be calculated from the Boltzmann relationship. Once $E_{Fn}$ is known, the local total trapped electron density can be obtained. The total trapped electron density can be obtained from equation 3.8.

### 3.9.1 Results

The parameter values common to all the figures are: $I_0 = 1 \times 10^{20}$ $m^{-2}s^{-1}$ $T = 293K$, $D_0 = 0.4$ $cm^2$ $s^{-1}$, $d = 13$ $\mu m$, $\alpha = 5.3{\times}10^4$ $m^{-1}$, $T_c = 950K$, $k_t = 1 \times 10^{10}$ $s^{-1}$, $N_c = 1 \times 10^{26} m^{-3}$, $N_{t0} = 1 \times 10^{27}$ $m^{-3}$, $\tau_0 = 4 \times 10^{-5}$ s and $k_{ext} = 1 \times 10^3$ m $s^{-1}$, unless indicated on the figure captions. These values were chosen to be consistent with the parameter values used in [29, 68] and to maximize agreement with experimental data.

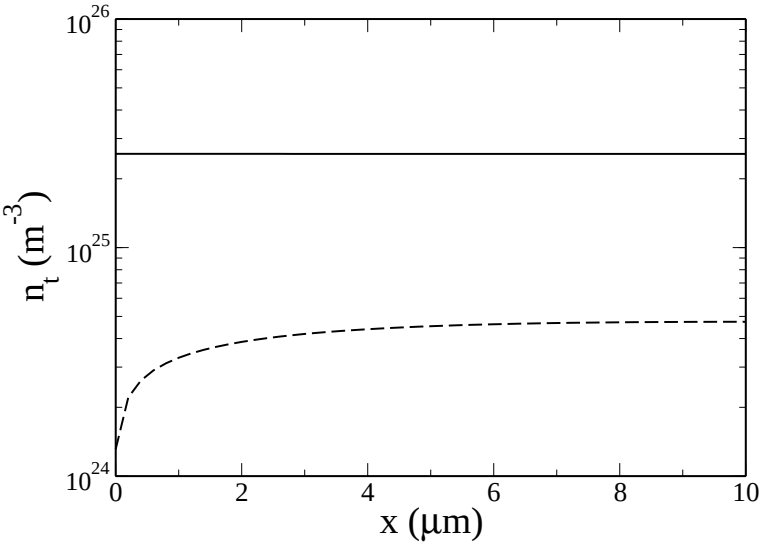


Figure 3.14: Trapped electron density calculated from the steady state continuity equation for open circuit (solid line) and short circuit (dashed line) conditions.

Figure 3.14 illustrates the simulated trapped electron density profiles, $n_t$, under open circuit and short circuit conditions. The figure 3.14 illustrates that the short circuit trapped electron density is lower compared to the open circuit trapped electron density and hence the electron quasi Fermi level at short circuit is lower compared to open circuit. Following Wang and Peter [68] and section 3.5.2 above, we determine the effective electron diffusion length using the total trapped electron density. There is a need to establish a pair of intensities for which the trapped electron density is the same at open circuit as at short circuit. This is the same idea which was introduced in section 3.5.2 above by using the free electron density and hence the quasi Fermi level to show that if the difference between short and open circuit is taken into consideration $L_n \simeq L_0$.

Figure 3.15 demonstrates the dependence of the trapped electron density on the free electron diffusion coefficient ($D_0$). It can be observed from the figure that a lower value of the diffusion coefficient gives rise to a higher trapped electron density.

### 3.9.2 Comparison with experimental results

Figures 3.16 and 3.17 illustrate the comparison between experimental and modeling IR responses, for short and open circuit respectively. The figure shows good agreement

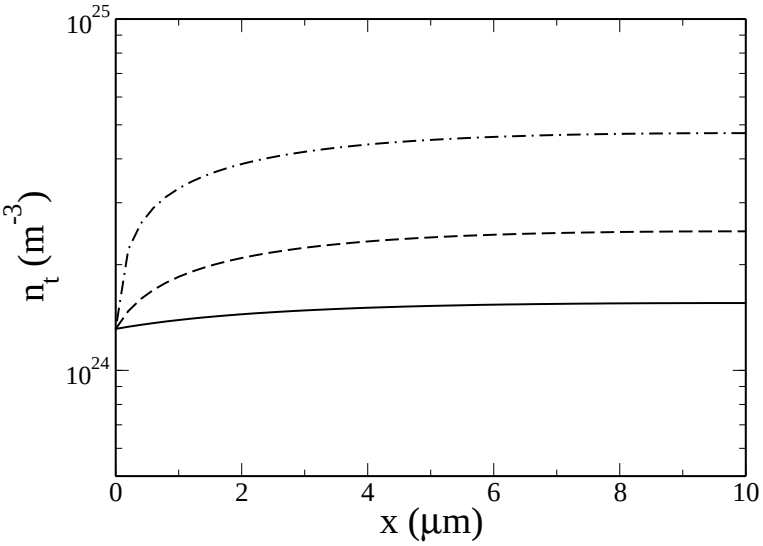


Figure 3.15: Dependency of the short circuit trapped electron density calculated from the steady state continuity equation on the diffusion coefficient for $D_0 = 0.4 \times 10^{-2}$ $m^2s^{-1}$ (solid line), $D_0 = 0.4 \times 10^{-3}$ $m^2s^{-1}$ (dashed line), $D_0 = 0.4 \times 10^{-4}$ $m^2s^{-1}$ (dashed-dot line).

between the modeling and the experimental results especially for the imaginary IR responses for both short and open circuit, as their $\omega_{min}$ are used to extract $D_n$ and $\tau_n$ respectively. Our results show that $\omega_{min}$ of the short and open circuit are not the same. This result shows that even when the short and open circuit IR responses are measured at the same quasi Fermi level, the transport time ($\tau_{tr}$) is different from the recombination time ($\tau_n$) as expected. This is in line with the fact that at short circuit the minimum angular frequency is related to the transport time, as we are looking at electron diffusion and at open circuit it is related to the electron recombination time The good agreement between the modelling and the experimental results shows that the near IR measurements can be used to study electron transport in DSSC.

## 3.10 Thickness dependence

In order to improve the DSSCs performance, optimization of the thickness of the porous $TiO_2$ layer is very important because the cell characteristics exhibit significant variation depending on the thickness of the porous $TiO_2$. Several studies have been conducted experimentally [63, 86, 87, 88] and theoretically [70, 71] to determine the effect of the $TiO_2$ film thickness on the performance of dye sensitized solar cells (DSSCs). Most

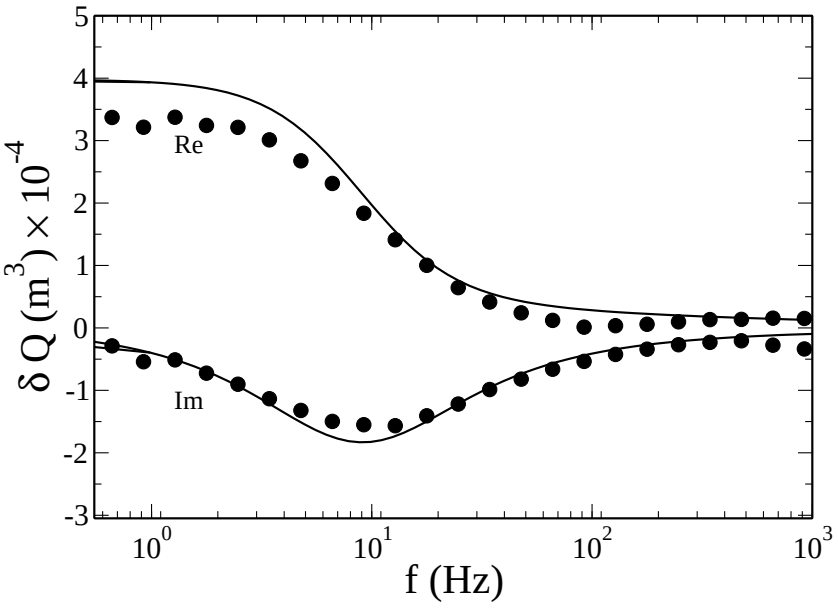


Figure 3.16: Comparison between numerical solution (solid line) and experimental results ( filled circles) for short circuit infrared response.

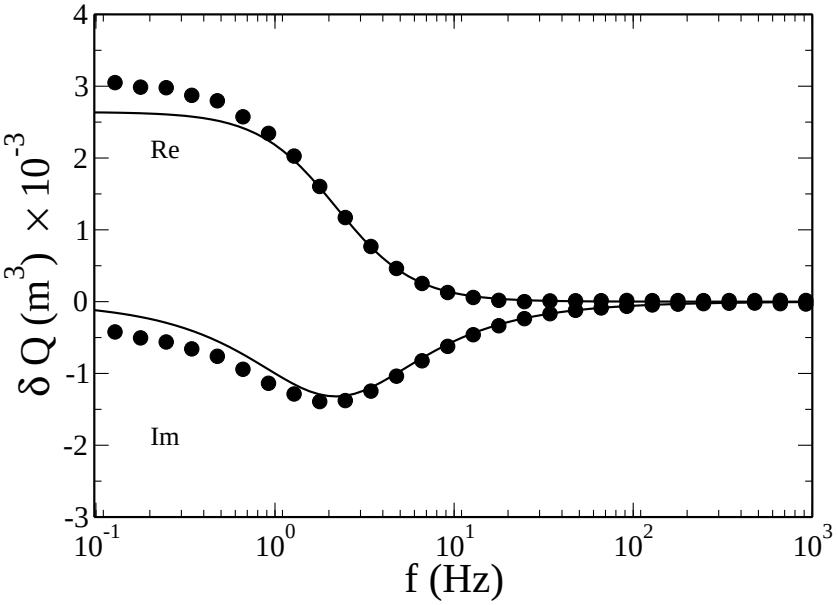


Figure 3.17: Comparison between numerical solution (solid line) and experimental results ( filled circles) for open circuit infrared response.

of the papers are based on the study of effects of the film thickness on short circuit current [86, 87], open circuit voltage [70, 86], fill factor [87], maximum power point [71], electron diffusion length [63], etc. The study of the dependence of the electron diffusion length on the film thickness is of more importance. Since by estimating the electron diffusion length we can get information about the electron transport and recombination processes in the dye sensitized solar cells.

It has been shown that the film thickness dependence of the photocurrent and photovoltage is limited at higher film thicknesses [86, 87]. Hara *et al.* [86] has reported that the photocurrent density increases up to 16 $\mu$m for DSSC due to an increase in the amount of dye adsorption on the surface of the $TiO_2$ film. Ito *et al.* [87] reported that the maximum short circuit photocurrent density corresponding to SE and EE side illumination is obtained for $TiO_2$ film thicknesses of 19 $\mu$m and 16 $\mu$m respectively. The most common utilized $TiO_2$ film thickness in various studies has been reported to be around 11-13 $\mu$m [89], although as reported by Hara and Ito [87, 86], film thicknesses can be greater than this, because the $L_n$ in DSSCs is expected to be longer than 20 $\mu$m [89].

Barnes *et al.* [63] reported that there is no clear link between electron diffusion length and the film thickness. As discussed above the electron diffusion length is the key parameter to characterize the performance of the solar cell. The collection of the photogenerated electrons depends on the competition between the diffusion of electrons into the $TiO_2$ film and the recombination of electrons with the redox electrolyte. In order to understand the meaning of the electron diffusion length in DSSCs, as described above, we calculate the diffusion lengths using $D_n$ and $\tau_n$ obtained from the IMPS and IMVS respectively, where the difference between the short circuit and open circuit quasi Fermi level was taken into account, to investigate the dependence of the ratio $\frac{L_n}{d}$ on the $\Delta E_{Fn}$, the difference between the open circuit and the short circuit quasi Fermi level at the same intensity.

### 3.10.1 Results

The parameter values common to all the figures are: $d = 13$ $\mu$m, $\alpha = 2.5\times10^5$ m$^{-1}$, $I_0 = 1 \times 10^{20}$ m$^{-2}$s$^{-1}$, T = 293K, $T_c = 1090$K, $D_0 = 0.4 \times 10^{-4}$m$^2$ s$^{-1}$, $k_t = 1 \times 10^{10}$ s$^{-1}$, $N_c = 1 \times 10^{26}$m$^{-3}$, $N_{t0} = 1 \times 10^{27}$ m$^{-3}$, $\tau_0 = 4 \times 10^{-5}$ s and $k_{ext} = 1 \times 10^3$ m s$^{-1}$ unless indicated on the figure captions. These values were chosen to be consistent with the parameter values used in [29, 68] and to maximize agreement with experimental data.

#### 3.10.1.1 Dependence of effective diffusion coefficient and lifetime

Figure 3.18, (A), illustrates the dependence of $D_n$ for substrate side illumination on the $TiO_2$ film thickness. It is evident from the figure that $D_n$ increases with increasing device thickness ($d$). The same observation was reported by Nakade *et al.* [90]. The effective electron life time decreases with an increasing film thickness as shown in figure 3.18, (B). At higher device thicknesses $\tau_n$ is almost independent of the device thickness.

#### 3.10.1.2 Dependence of electron quasi Fermi level

Figure 3.19 shows the electron quasi Fermi level profile variation for different $TiO_2$ film thicknesses. The variation of $E_{Fn}$ at short circuit and open circuit indicates the electron distribution on the film respectively. As illustrated in the figure the profile distribution of the Fermi level differ for different device thicknesses. At lower film thicknesses, we expect a high probability of electron recombination compared to higher film thicknesses. For higher device thickness $d > 15\mu$m our results shows that the profile variation of the short circuit Fermi level is the same. For higher values of the device thickness, higher than the value used here, there are effects on the electron transport, like the higher resistance of the thicker film [71], the depth of the light absorption [70, 71, 86], etc.

Figure 3.20 illustrates the dependence of $\Delta E_{Fn}$ on the device thickness ($d$). $\Delta E_{Fn}$ is defined as the difference between the open and short circuit quasi Fermi levels at the same intensity. As illustrated in the figure, $\Delta E_{Fn}$ decreases with increasing device thickness, this is from the fact that $V_{oc}$ decreases with an increase in device thickness [71, 86, 91]. As light is transmitted into the depth of the $TiO_2$ film, the intensity gradually decreases. Therefore as $d$ increases the free electron density becomes lower, resulting in a lower $V_{oc}$. Ni *et al.* [71] further explain that the higher resistance of the thicker film also contributes to the reduction of the photovoltage. At higher thicknesses the number of useful photons for electron photogeneration will reach a limit and thus a further increase in the device thickness will not increase the performance of the cell. An increase in the device thickness leads to an increase of loss in the injected electrons due to recombination of the electrons in the $TiO_2$ nanoparticles and increasing the series resistance of the cell, resulting in a decrease in the photovoltage. The decrease of $V_{oc}$ with an increase in the thickness is also due to $TiO_2$ sites where no dye is adsorbed [87]. For higher thicknesses there will be a large surface area not covered by dye compared to lower thicknesses. Thus increasing the thickness leads to an increase in the non-excited area which lowers $V_{oc}$. As the short circuit $E_{Fn}$ does not vary at higher device thicknesses but the open circuit $E_{Fn}$ decreases, $\Delta E_{Fn}$ will decrease with increasing $d$.

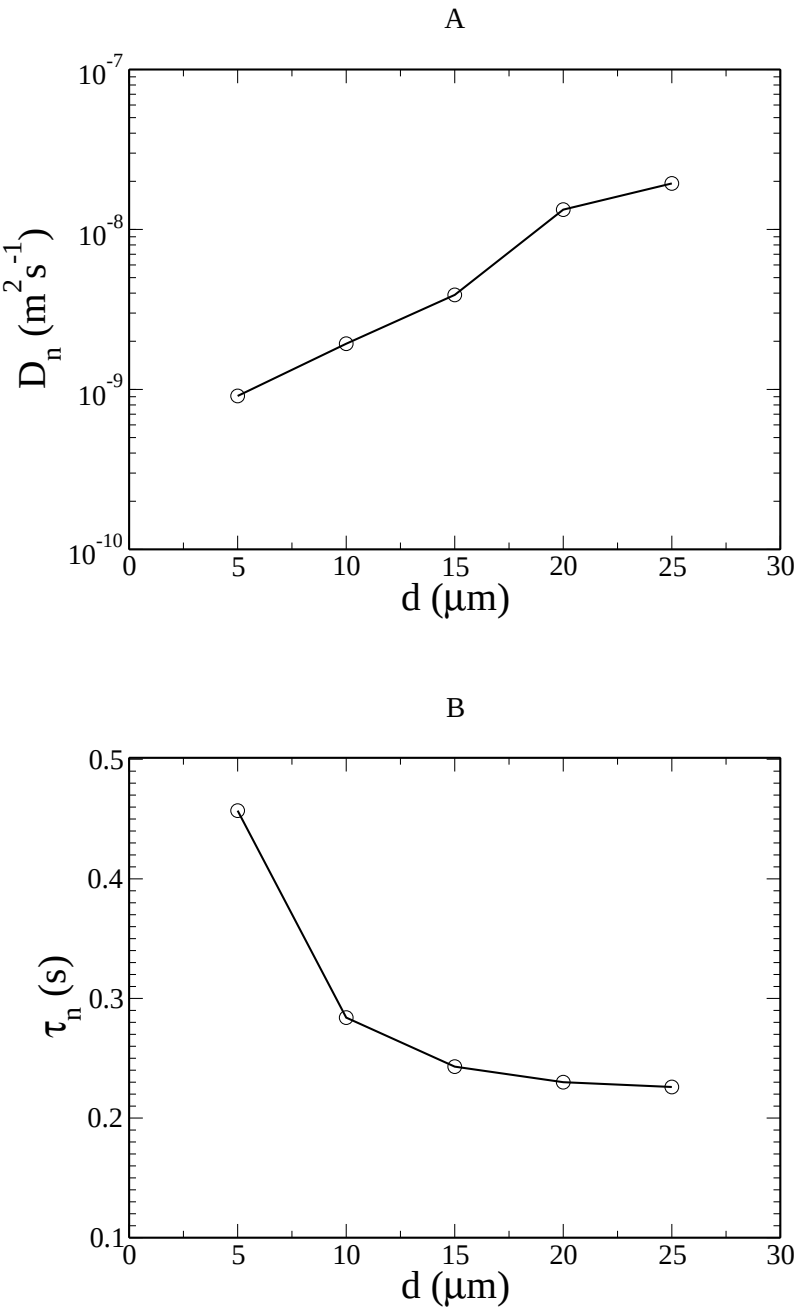


Figure 3.18: Dependence of $D_n$ (A) and $\tau_n$ (B) on the device thickness (d), for substrate side illumination.

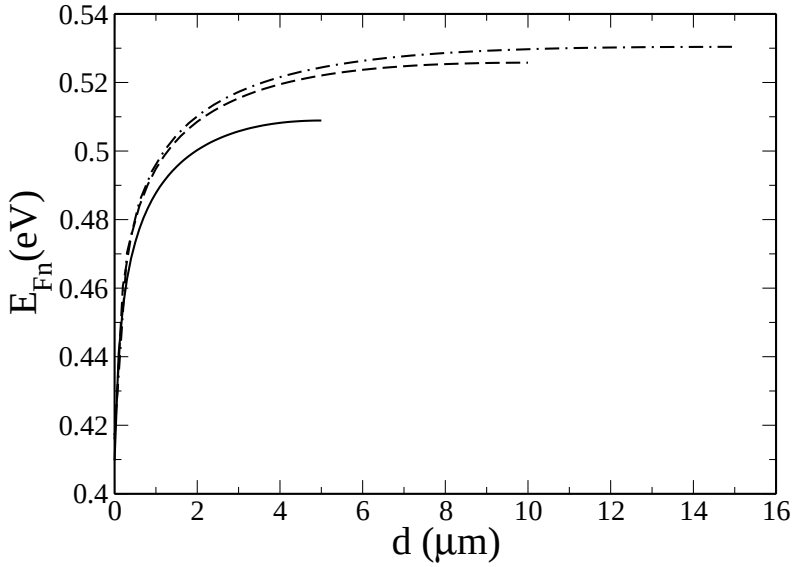


Figure 3.19: Dependence of quasi Fermi level $E_{Fn}$ profile on the device thickness ($d$) for substrate side illumination). $d = 5$ $\mu$m (solid line), $d = 10$ $\mu$m (dashed line), $d = 15$ $\mu$m (dash-dot line),

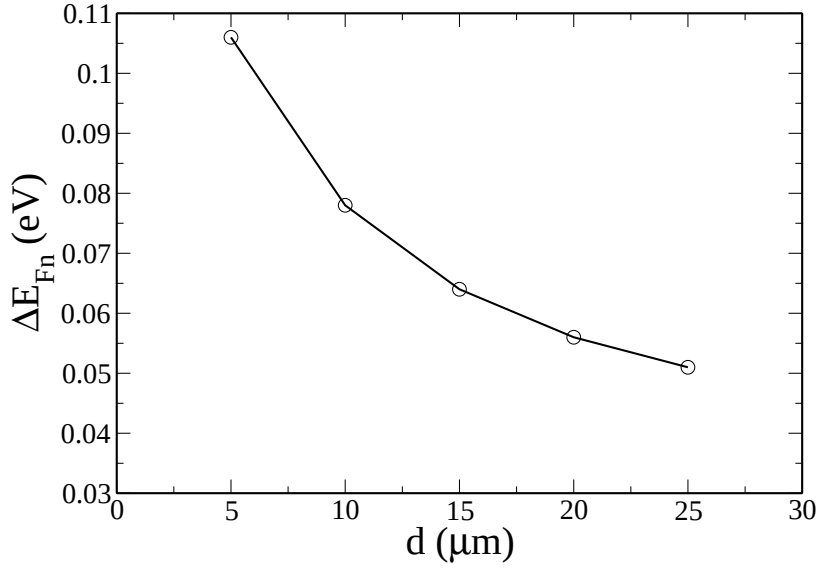


Figure 3.20: Dependence of $\Delta E_{Fn}$ on the device thickness ($d$) thickness for substrate side illumination.

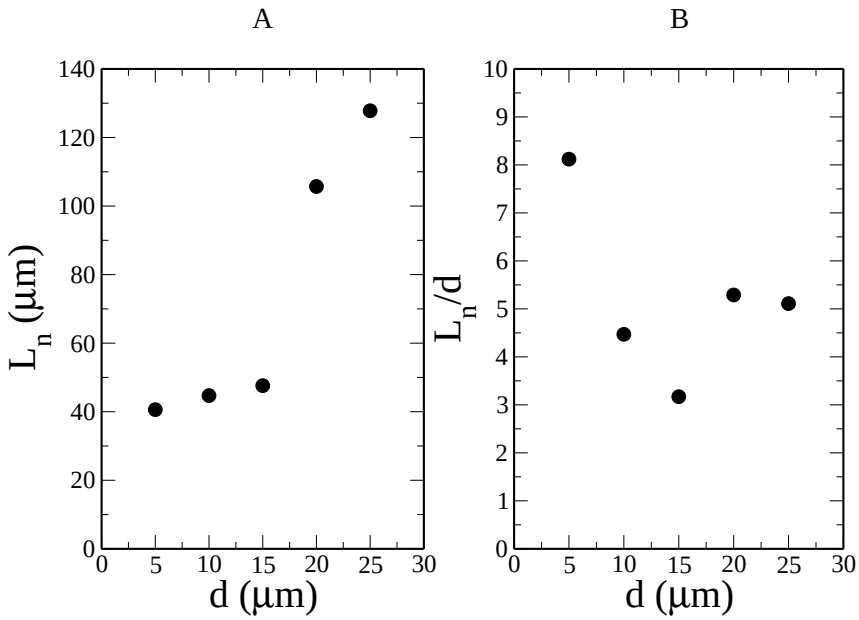


Figure 3.21: Dependence of $L_n$ (A) and $\frac{L_n}{d}$ (B) on the device thickness ($d$).

#### 3.10.1.3 Dependence of electron diffusion length

Figure 3.21 (A) and (B), illustrates the dependence of $L_n$ and $\frac{L_n}{d}$ on $d$ respectively. As shown in the figure (A), the dependence of $L_n$ on $d$ does not give clear information, as there is no trend in $L_n$ varying with $d$. The similar trend of the dependence of $L_n$ on the film thickness was also experimentally observed and reported by Barnes *et al.* [63]. Further to the dependence of the electron diffusion length on the film thickness we investigate the dependence of $\frac{L_n}{d}$ on the film thickness as illustrated in figure 3.21, (B). It can be observed from the figure that, there is no trend in the dependence of $\frac{L_n}{d}$ on $d$. Thus the dependence of $L_n$ and ratio $\frac{L_n}{d}$ on device thickness does not show a clear way forward on the improvement of the electron transport and performance of the dye sensitized solar cells.

### 3.10.2 Comparison with experimental result

Experimental measurements were carried out by H. Wang at the University of Bath, Department of Chemistry to investigate the dependence of $L_n$ on $\Delta E_{Fn}$. Two types of $TiO_2$ paste/colloid (Solaronix HT and Dyesol) were employed in order to adjust the thickness of $TiO_2$ film. Different DSSCs of different $TiO_2$ thickness were made. As described in section 3.8, IMPS and also IMVS measurements in this case were

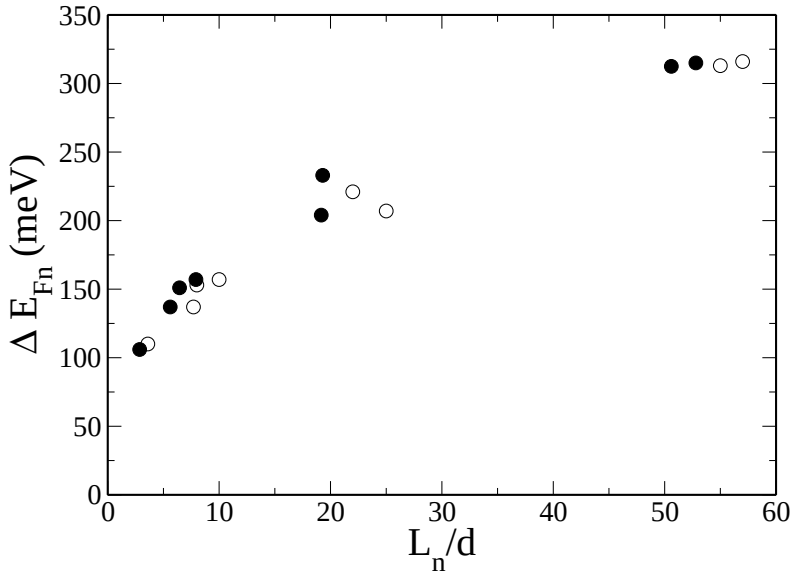


Figure 3.22: Comparison between the experimental (filled circles) and simulations (circles) results, for the dependence of $\frac{L_n}{d}$ on $\Delta E_{Fn}$.

performed to determine the $E_{Fnsc}$, $E_{Fnoc}$,$\Delta$ $E_{Fn}$ and $L_n$ for the different solar cells.

Simulations were performed for different values of $d$ to calculate the value of $L_n$ by extracting the value of $D_n$ and $\tau_n$ at the same quasi Fermi level. $\Delta$ $E_{Fn}$ was calculated from $E_{Fnscav}$ and $E_{Fnoc}$ at the same intensity, see 3.5.2 above. Figure 3.22 shows the comparison between the modelling and the experimental results for the dependence of $\frac{L_n}{d}$ on $\Delta E_{Fn}$. The results show good agreement. As illustrated in the figure $\Delta E_{Fn}$ increases with increasing $\frac{L_n}{d}$. As $\frac{L_n}{d}$ increases with increasing $\Delta E_{Fn}$ to further improve the performance of the dye sensitized solar cells more work needs to be done to look towards enhancing the light harvesting efficiency of the dye over a broader spectrum such as the infrared region.

## 3.11 Conclusion

The multiple trapping model based on diffusion as the main driving force for electron transport in dye solar cells has been presented. In this work we were able to show that the free electron diffusion length ($L_0$) is almost equal to the effective diffusion length ($L_n$) provided the difference between the quasi Fermi levels is taken into consideration. The IMPS and IMVS are a better way of estimating the electron diffusion length in DSSCs, as they can be used over a wide range of intensities to determine $D_n$ and $\tau_n$ respectively. Our IMPS simulation results shows good agreement with the experimental IMPS results.

We also succeeded in showing that the dependence of electron diffusion length of dye sensitized solar cells in $TiO_2$ film thickness has no trend which can give information on electron transport. The difference in the electron quasi Fermi level at open and short circuit at the same intensity, is found to depend on the ratio $\frac{L_n}{d}$ and our simulations results also show good agreement with the experimental results.

Future work

The problem encountered in the literature is that several studies show that different experimental methodologies give different values of $L_n$ [19, 63, 64], while other studies show the agreement between different methodologies [65, 66]. This shows that much work still needs to be done to understand the real meaning of $L_n$ in DSSCs and electron transport as a whole. The meaning of the $D_n$ and $\tau_n$ needs to be understood as these parameters describe the performance of the solar cells. In this work our calculations are based on the assumption that the electron recombination is first order, currently work is in progress to extend the model to understand for the case when the recombination is not first order or nonlinear.

The film morphology also affects the path length of the electrons in the film. From the multiple trapping model, the longer the transport pathway, the more electrons undergo trapping and detrapping events and the longer they spend in the particle network before being collected. In this scenario transport is limited both by trapping and film morphology. The optimization of the film morphology, thickness and understanding the absorption coefficient as it varies with the film thickness needs more attention to improve the efficiency of DSSCs.

# Chapter 4

# Study of Photo-Generated Charge Carrier Density in Dye Sensitized Solar Cells by Microwave Reflectance

## 4.1 Introduction

In this work, simulations of microwave reflectivity experiments have been carried out with the aim of quantifying the charge carrier density in Dye Sensitized Solar Cells (DSSCs). These calculations are made relatively difficult by the complex multilayered structure of the DSSCs. The main focus of this work is to quantify the relationship between the photomodulated reflectivity and conductivity of the porous $TiO_2$ semiconductor layer. Interpretation of the experimental results requires a relationship between the reflectivity and conductivity to be established. In addition to calculating this proportionality factor, we also want to quantify the electron transport in DSSCs, as a better understanding of the transport mechanism could lead to improved device efficiency. Ultimately, we aim to simulate and explain the experimental results. We need to answer and explain the following questions,

1. What is the relation between the photomodulated reflectivity and the photoconductivity?
2. How does the reflection coefficient depend on the device geometry?

3. Why is the relationship between the conductivity and light intensity nonlinear?

Microwave reflectivity is now a well established tool for measurements of charge carriers in semiconductors [92, 93]. This technique can be used to determine bulk minority-carrier lifetimes and surface recombination velocities, carrier mobilities, dielectric constants and effective masses, and to study charge transfer from excited dye molecules to semiconductors [94]. Knowledge of the kinetics of free charge carriers is essential to understand the function and performance of solar cells and of many semiconductor devices [95]. Microwave reflection measurements of these kinetics are attractive because they avoid the need for contacts or special sample preparation and are non-destructive [96]. Another important fact is that, as this technique involves high frequency it is sensitive to high mobility charge carriers. Measurements of free charge carrier kinetics at microwave frequencies range are appropriate for the study of the low conductivity semiconductor materials [97].

To summarize, since microwave reflectivity is sensitive to the concentration of free charge carriers, such measurements can be used to monitor photo-induced change in carrier density in semiconductor materials [97].

## 4.2 Conductivity of semiconductor materials

In DSSCs, a porous $TiO_2$ layer functions as an electron collector and transport material. As mentioned above the porous $TiO_2$ film has a high surface area, which gives high probability of dye surface coverage and has attracted much interest in DSSCs [98]. Better understanding of the transport mechanism in this material could lead to efficiency improvements of the solar cells. Thus the microwave reflection measurements are useful for the future development of DSSCs.

Electromagnetic waves penetrate much deeper in materials with a low electrical conductivity and are reflected by highly conducting materials such as metals [99]. As the $TiO_2$ is assumed to have a low conductivity, we expect the microwaves to penetrate deeply and the reflection of the microwave power to give information about the electron transport. The reflection of the microwaves by a semiconductor layer is determined by its conductivity as discussed in section 4.4 below. The conductivity is determined by the concentration of the free carriers, such as electrons [99]. In the dark the concentration of the free charge carriers is low in pure semiconductor materials. Under illumination the concentration of the free carriers increases. The photo induced free charge carriers will change the conductivity of the semiconductor and hence the reflected microwave

power [99, 100]. The conductivity is related to the free electron density by,

$$\sigma = n_c \mu_e q \tag{4.1}$$

where $n_c$ is the free electron carriers density, $\mu_e$ is the electron mobility and q is the electron charge. The contribution made by positive charge to the conductivity can be neglected due to their low mobility. Thus photomodulated experiments yield a quantity dependent upon the change in conductivity ($\Delta\sigma$) on illumination [96]. This assumption is made throughout this work.

Several microwave frequency photoconductivity experiments have been reported in the literature. The majority of these studied silicon (Si) [93, 95, 96, 97, 99, 101, 102]. There are few measurements of porous semiconductors [103, 104, 105, 106]. In particular, very few experimental results have been reported on porous $TiO_2$ films [104, 107] and so far no work has been reported on microwave measurements in a fully working dye sensitized solar cell according to the our knowledge. The experimental measurements are based on the assumption of a linear relationship between the photomodulated microwave power reflection and the change in conductivity [96].

## 4.3 Experimental setup and measurements

The experimental measurements were performed by Halina Dunn [108]. The experimental arrangement is illustrated in figure 4.1. DSSCs, and the simplified structures relevent to them, were fixed onto the end of a waveguide as clearly illustrated in figure 4.2 and irradiated with a few mW (milliwatt) of $\approx$ 33 GHz microwaves. The power reflected back into the waveguide was sampled by a directional coupler and measured with a detector. The main aim of our calculations was to provide a proportional factor that can be used to relate experimental microwave reflectivity to the $TiO_2$ conductivity.

As illustrated in figure 4.2 measurements were performed in two different cases, a case with a highly conducting layer behind the solar cell (short) (A) and without a short (B). Figure 4.2 illustrates the different layers making up a DSSC and as mentioned earlier it can be observed that the structure of DSSC is quite complex, as it has several layers of different thicknesses. As shown in the figure there is a window in the highly conducting fluorine tin oxide (FTO) layers to allow microwave power to pass through to the $TiO_2$ layer. The windows were created by etching away the FTO. They are the same dimension as the waveguide opening. The figure illustrates the different layers of material which build up the dye sensitized solar cell. We have several layers of different thicknesses: 1mm glass, 200 nm FTO layers with a window, compact $TiO_2$

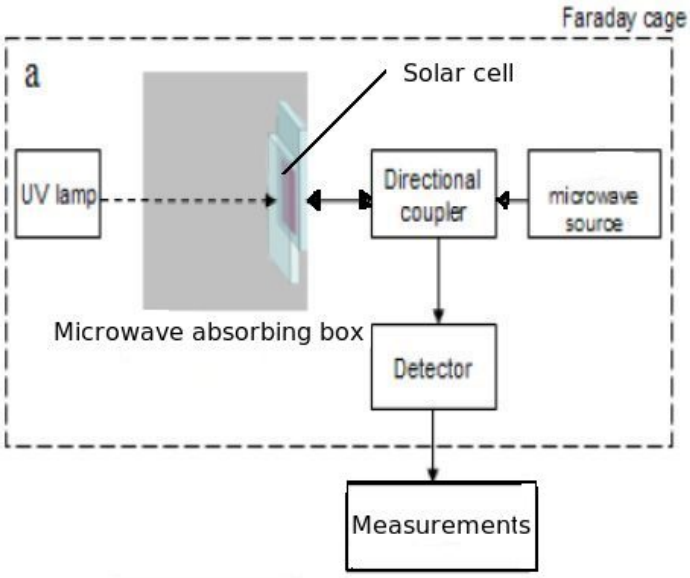


Figure 4.1: The graphical representation of the setup of the experiment to measure the reflection coefficient using microwave techniques, image from [108]

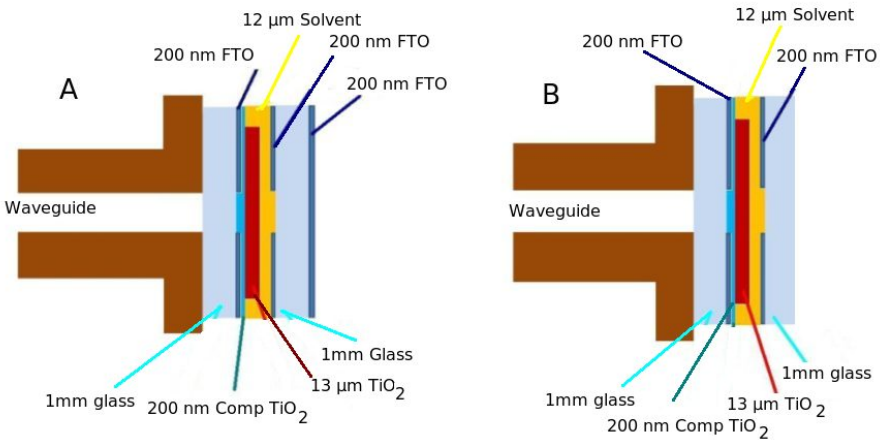


Figure 4.2: Illustration of the experimental setup of the microwave reflection measurements. (A) represents a case when we have a shorting layer behind the cell and (B) represents a case without a short.

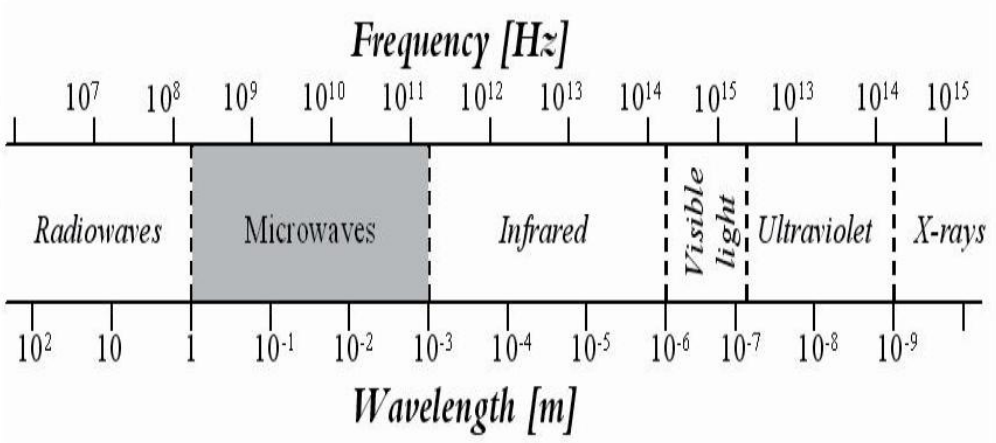


Figure 4.3: Electromagnetic spectrum with the wavelength in free space.

(Comp $TiO_2$), $TiO_2$ (13 $\mu m$) and the electrolyte (12 $\mu m$). The compact $TiO_2$ layer is essential to avoid short circuiting and loss of current through recombination at the FTO electrode [109]. As illustrated in figure 4.2 (A) the last layer of FTO is not etched and acts as a short. All the microwave power which reaches it will be reflected back. Simulations where done for both types of the structure (with and without a short).

## 4.4 Physical principles of microwave reflection

The electromagnetic spectrum shown in figure 4.3 covers radiation with a different wide range of properties. Microwaves are electromagnetic waves that have a frequency range from around 0.3 GHz to 300 GHz with corresponding wavelengths ranging from 1m to 1mm.

The theoretical analysis of the microwave reflectance involves solving Maxwell's equations with the appropriate boundary conditions. Maxwell's equations are given by [110, 111, 112]:

$$\bigtriangledown \times \mathbf{E} = -\frac{\partial \mathbf{B}}{\partial t} \tag{4.2}$$

$$\bigtriangledown \times \mathbf{H} = \mathbf{J} + \frac{\partial \mathbf{D}}{\partial t} \tag{4.3}$$

$$\bigtriangledown \cdot \mathbf{D} = \rho \tag{4.4}$$

$$\bigtriangledown \cdot \mathbf{B} = 0 \tag{4.5}$$

where $\mathbf{E}$ is the electric field, $\mathbf{H}$ is the magnetic field, $\mathbf{D} = \epsilon\ \mathbf{E}$, $\mathbf{B} = \mu\ \mathbf{H}$, $\mathbf{J} = \sigma\ \mathbf{E}$, $\mu$ is the permeability, $\epsilon$ is the permittivity, $\sigma$ is the electrical conductivity of the medium, $\mathbf{D}$ is the electric flux density, $\mathbf{B}$ is the magnetic flux density and $\mathbf{J}$ is the electric current density.

### 4.4.1 Propagation of waves in an isotropic dielectric

Before we consider the reflection of microwave at an interface, we must first understand how the characteristics of a medium affect the propagation within that medium.

In general, a dielectric material can be described by the permittivity, $\epsilon$, the permeability, $\mu$, and the electric conductivity, $\sigma$. Using a relative permittivity $\epsilon_r$ and a relative permeability $\mu_r$, $\epsilon$ and $\mu$ are written as $\epsilon = \epsilon_r\epsilon_0$ and $\mu = \mu_r\mu_0$, where $\epsilon_0$ and $\mu_0$ are the permittivity and permeability of free space. These properties of the materials determines the attenuation and phase of the microwave fields. For a plane wave in a homogeneous lossy medium propagating along z axis, the electric field can be simply written as [110, 113],

$$\mathbf{E} = R_e\left(\mathbf{E}_0 e^{(-\gamma z + jwt)}\right) \tag{4.6}$$

where $\omega$ is the angular frequency of wave, $\gamma$ is the propagation constant and Re denotes that the real part of the expression is taken (in some notation this is implicitly assumed).

The propagation constant determines the change undergone by the amplitude and phase of the wave as it propagates in a given direction

$$\gamma = j\omega\sqrt{\epsilon\mu(1 + \frac{\sigma}{j\omega\epsilon})} = \alpha + j\beta \tag{4.7}$$

The real part of the propagation constant is defined as the attenuation constant ($\alpha$) while the imaginary part is defined as the phase constant ($\beta$). The attenuation constant determines the rate at which the fields of the wave are attenuated and the phase constant determines the rate at which the phase changes as the wave propagates. The bigger $\alpha$ becomes, the higher the attenuation.

$\alpha$ and $\beta$ can be expressed in terms of the material properties, $\epsilon$,$\mu$ and $\sigma$ respectively as [110, 113],

$$\alpha^2 = \frac{\omega^2}{2}\mu\epsilon\left[-1 + \sqrt{1 + \frac{\sigma^2}{\omega^2\epsilon^2}}\right] \tag{4.8}$$

and

$$\beta^2 = \frac{\omega^2}{2}\mu\epsilon\left[1 + \sqrt{1 + \frac{\sigma^2}{\omega^2\epsilon^2}}\right] \tag{4.9}$$

For a case of a lossless material, $\sigma = 0$, the attenuation constant ($\alpha$) is zero, and $\beta = \omega\sqrt{\mu\epsilon}$ so no power is lost during the propagation of the wave. The propagation constant becomes complex given by,

$$\gamma = \sqrt{j\omega\epsilon\mu} \tag{4.10}$$

For a lossy material, $\sigma \ll \omega\epsilon$, the propagation constant has both the real and imaginary parts and $\alpha = \mathrm{Re}(\gamma)$ and $\beta = \mathrm{Im}\ (\gamma)$. Thus the wave travels with attenuation determined by $\sigma$ of the material.

For a good conductor $\sigma \gg \omega\epsilon$ and

$$\alpha = \beta \simeq \sqrt{\frac{\omega\mu\sigma}{2}} \tag{4.11}$$

Thus both the attenuation constant and the phase constant increase as $\sqrt{\gamma}$. The attenuation of the waves in a good conductor increases with frequency as clearly illustrated by 4.11. The inverse of equation 4.11 described the skin depth which is described as [110],

$$\delta_s = \sqrt{\frac{2}{\omega\sigma\mu}} \tag{4.12}$$

where $\omega$ is the angular frequency ($2\pi$f), $\sigma$ is the electrical conductivity and $\mu$ is the permeability. The skin depth, equation 4.12 shows that the depth to which the electromagnetic radiation can penetrate a conducting surface decreases as the electrical conductivity and the angular frequency increases. The skin depth is of the order of a micron or less for most metals at microwave frequencies. On the other hand, microwaves only partially reflect from and freely propagate through dielectric materials. It is the

combination of these two conditions which allowed the development of microwave reflection method which permits the measurements of dielectric properties in different materials. As in this work the angular frequency is fixed, thus the skin depth will be determined by the conductivity of the semiconductor $TiO_2$ and hence the reflection coefficient will depend on the conductivity.

As described above when microwaves are directed towards a material, part of the energy is reflected, part is transmitted through the surface and of this latter quantity part of it is absorbed. The proportions of energy, which falls into these categories have been defined in terms of the dielectric properties. The dielectric constant ($\epsilon$) tells us a lot about reflection properties and wavelength in the material. The free space wavelength ($\lambda_0$) is reduced by a factor $\epsilon$ as the microwaves propagates inside the material [114],

$$\lambda = \frac{\lambda_0}{\sqrt{\epsilon}} \tag{4.13}$$

### 4.4.2 Reflection from an interface

When a plane wave propagating in a homogeneous medium encounters an interface with a different medium, a portion of the wave is reflected from the interface while the remainder is transmitted. This situation is shown in figure 4.4. The reflected and transmitted waves can be determined by considering the electromagnetic field boundary conditions at the interface. The expressions of the incident $\mathbf{E}_i$, reflected $\mathbf{E}_r$ and transmitted $\mathbf{E}_t$ electric fields may be written as [113],

$$\mathbf{E}_i = \mathbf{E}_0 e^{(-\gamma_1 z + j\omega t)}, \tag{4.14a}$$

$$\mathbf{E}_r = \Gamma\ \mathbf{E}_0 e^{(\gamma_1 z + j\omega t)}, \tag{4.14b}$$

$$\mathbf{E}_t = T\mathbf{E}_0 e^{(-\gamma_2 z + j\omega t)} \tag{4.14c}$$

where $\Gamma$ is the voltage reflection coefficient and $T$ is the voltage transmission coefficient.

At the interface (z=0) the tangential continuity electric and magnetic field boundary conditions must be satisfied so that,

$$\mathbf{E}_i + \mathbf{E}_r = \ \mathbf{E}_t \Rightarrow 1 + \Gamma = T \tag{4.15}$$

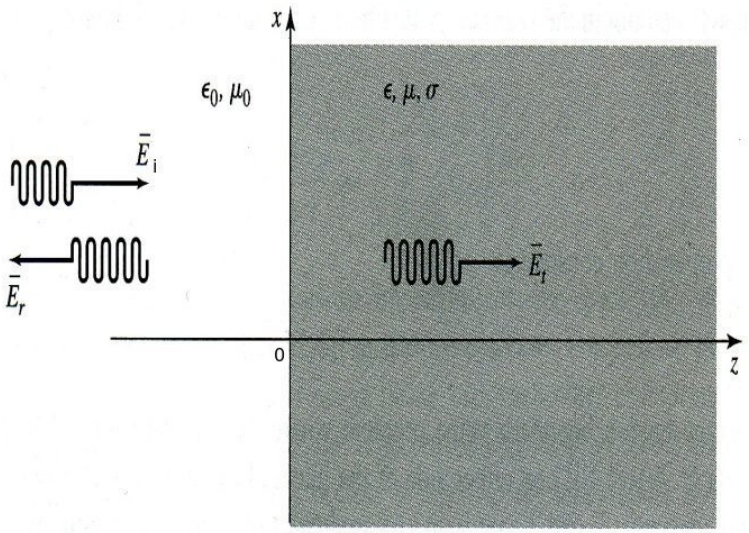


Figure 4.4: Reflection and transmission of a plane wave incident on a single lossy dielectric material, normal incidence, picture from [113].

and

$$\mathbf{H}_i + \mathbf{H}_r = \mathbf{H}_t \Rightarrow \frac{1-\Gamma}{\sqrt{\frac{\mu_0}{\epsilon_0}}} = \frac{T}{\sqrt{\frac{\mu}{\epsilon}}} \tag{4.16}$$

where $\mu_0$ is the permeability of the free space, $\epsilon_0$ is the permittivity of the free space, $\mu$ is the permeability of the medium and $\epsilon_0$ is the permittivity of medium as illustrated in the figure.

The voltage reflection coefficient can be given as [92],

$$\Gamma = \frac{(\gamma_1 - \gamma_2)}{(\gamma_1 + \gamma_2)} \tag{4.17}$$

where $\gamma_1$ is the permittivity of the first medium and $\gamma_2$ is the permittivity of the second medium.

The total electric field in the two media are given as,

$$\mathbf{E}_1 = \mathbf{E}_i + \ \mathbf{E}_r = \mathbf{E}_0 \left[ e^{(-\gamma_1 z + j\omega t)} + \Gamma e^{(\gamma_1 z + j\omega t)} \right] \tag{4.18}$$

at medium one and

$$\mathbf{E}_2 = \mathbf{E}_t = \mathbf{E}_0 \left[ T e^{(-\gamma_2 z + j\omega t)} \right] \tag{4.19}$$

at medium two.

The power reflection coefficient R($\sigma$) is calculated from the voltage reflection coefficient as [92],

$$\frac{\Delta V(\sigma)}{V(\sigma)} = \Gamma \tag{4.20}$$

which is equivalent to the field reflection coefficient $\frac{\Delta \mathbf{E}(\sigma)}{\mathbf{E}(\sigma)}$,

$$R(\sigma) = \frac{\Delta P(\sigma)}{P(\sigma)} = \left( \frac{\Delta V(\sigma)}{V(\sigma)} \right) \left( \frac{\Delta V(\sigma)}{V(\sigma)} \right)^* = \left( \frac{\Delta \mathbf{E}(\sigma)}{\mathbf{E}(\sigma)} \right) \left( \frac{\Delta \mathbf{E}(\sigma)}{\mathbf{E}(\sigma)} \right)^* = \Gamma\Gamma^* \tag{4.21}$$

where $*$ denotes the complex conjugate.

### 4.4.3 Microwave interference within a layered dielectric structure

As discussed above when a plane wave propagating in a homogeneous medium encounters an interface with a different medium, a portion of the wave is reflected from the interface while the remainder of the wave is transmitted. The dye sensitized solar cell is made up of several layers as illustrated under the experimental setup and measurements, so we understand that the microwave will undergo multiple reflection within the solar cell structure. As a way of developing the modelling we need to first understand the behaviour of the multiple reflection within different layers.

Kunst and Beck describe a simple case for calculating the reflection coefficient of a dielectric layer with thickness $d$ [92]. In general as illustrated in figure 4.5 the wave incident on the boundary with the second medium is partially reflected back and partially transmitted to medium 2. At the interface between materials 2 and 3, the transmitted to material 2 field is partially reflected back and partially transmitted to the material 3, etc. If there is also another material 4, the same process of reflection will happen between material 3 and material 4. Thus there will be multiple reflections at the difference interfaces and the reflection coefficient can be calculated by summing all these reflections.

As the wave is reflected back and transmitted through the material its magnitude and phase change, thus in other words the magnitude and phase of the wave will decrease as it is reflected back and forth through the material. This makes $\Gamma$ depend on the

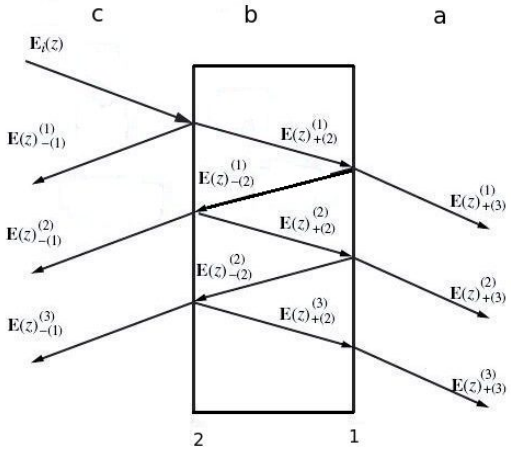


Figure 4.5: Illustration of normal plane wave reflection on a single layer of a dielectric material of thickness $d$, where a, b,c, represent the different medium and 1,2, indicates the interfaces.

magnitude and phase of the wave at the interface. In a homogeneous medium, the voltage reflection coefficients at positions $z_1$ and $z_2$ are related by [92],

$$\Gamma(z_1) = \Gamma(z_2)e^{2\gamma(z_1 - z_2)} \tag{4.22}$$

The voltage reflection coefficient $\Gamma_1$ at interface 1 is given by,

$$\Gamma_1 = \Gamma_{ab} = \frac{(\gamma_b - \gamma_a)}{(\gamma_a + \gamma_b)} \tag{4.23}$$

The interface between two media are characterized by the propagation constant $\gamma_1$ and $\gamma_2$, the voltage reflection coefficients $\Gamma_1$ and $\Gamma_2$ in these media are related by,

$$\Gamma_2 = \frac{(\Gamma_{bc} + \Gamma_1 e^{(2\gamma d)})}{1 + \Gamma_{bc}\Gamma_1 e^{(2\gamma d)}} \tag{4.24}$$

where $d$ is the thickness of the layer.

If anywhere $\Gamma$ is known as a function of material constants, successive application of

equation 4.24 at the interfaces and of equation 4.22 in homogeneous media finally yields the voltage reflection coefficient. If there is a short (in other words when we have a highly conducting layer at the end of structure), i.e., $\Gamma$ = -1 at the last interface , $\Gamma(\sigma)$ is given by,

$$\Gamma(\sigma) = \frac{(\Gamma_1 - e^{-2\gamma_2 d})}{(1 - \Gamma_1 e^{-2\gamma_2 d})} \tag{4.25}$$

The reflection coefficient is calculated as [92],

$$R(\sigma) = \frac{R_{12} + e^{4\alpha_2 d} - 2e^{2\alpha_2 d}(f cos 2\beta_2 d - g sin 2\beta_2 d)}{1 - R_{12} e^{4\alpha_2 d} - 2e^{2\alpha_2 d}(f cos 2\beta_2 d - g sin 2\beta_2 d)} \tag{4.26}$$

where $R_{12} = \Gamma_{12}\Gamma_{12}^*$. The real and imaginary part of $\Gamma$ are denoted by f and g, respectively.

The above discussion is based on a layer of dielectric, but as mentioned above the DSSC has a multilayered structure. Considering this and the above way of summing the reflection coefficient in a single dielectric slab, we show how this idea can be extended to a multilayer system as illustrated on figure 4.6. As discussed above the voltage reflection coefficients at interface 1,2,3, are given by,

$$\Gamma_1 = \Gamma_{ab} = \frac{(\gamma_b - \gamma_a)}{(\gamma_a + \gamma_b)} \tag{4.27a}$$

$$\tag{4.27b}$$

$$\Gamma_2 = \frac{\Gamma_{bc} + \Gamma_1 e^{(2\gamma \Delta z_b)}}{1 + \Gamma_{bc}\Gamma_1 e^{(2\gamma \Delta z_b)}} \tag{4.27c}$$

$$\tag{4.27d}$$

$$\Gamma_3 = \frac{\Gamma_{cd} + \Gamma_2 e^{(2\gamma \Delta z_c)}}{1 + \Gamma_{cd}\Gamma_1 e^{(2\gamma \Delta z_c)}} \tag{4.27e}$$

$$\tag{4.27f}$$

$$\Gamma_4 = \frac{\Gamma_{de} + \Gamma_3 e^{(2\gamma \Delta z_d)}}{1 + \Gamma_{de}\Gamma_1 e^{(2\gamma \Delta z_d)}} \tag{4.27g}$$

The same theory can be used for all $n$ layers, since the total voltage reflection coefficient can be obtained by summing all the different reflections on the interfaces. Based on this argument a one dimensional model was developed as a starting point to solve the problem. The results and limitations of the one dimensional model are discussed below in section 4.5.2.1.

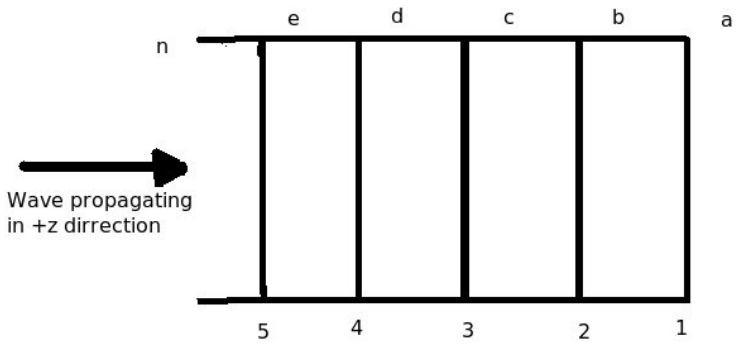


Figure 4.6: Multilayered structure of different material $a, b, c, d$, which can be extended to any number of layers as indicated by $n$, where 1,2,3,4,5 represent different interface.

### 4.4.4 Propagation and reflection in a waveguide

The waveguide is in essence a device for transporting electromagnetic energy from one region to another. It can support multiple modes. Each mode is characterized by a cutoff frequency, below which the wave will be attenuated. The waveguide can be forced to operate in a low single mode if an appropriate frequency is used.

The rectangular waveguide has a width $a$ in the x-direction, and a height $b$ in the y-direction. The z-axis is the direction in which the waveguide is to carry power. Simulations were performed using a rectangular waveguide, following the experimental setup and the choice of a rectangular waveguide used with the dimension of height, $b$= 7mm, the width, $a$= 3.5mm and the microwave frequency of 33 GHz. The rectangular waveguide supports the use of the $TE_{10}$ mode. The $TE_{10}$ mode is the dominant mode of a rectangular waveguide, since it has the lowest attenuation of all modes. The other advantage of this waveguide is that it support only one dominant mode in the frequency range between 26.4 to 40.1 GHz [110]. The speed of the wave in a waveguide is lower than the speed of wave in the free space and the propagation constant is given as [92],

$$\gamma = \sqrt{\frac{\pi^2}{a^2} - \omega^2 \mu_0 \epsilon_0 \epsilon_r + j\omega\mu_0\sigma} \tag{4.28}$$

where $a$ is the width of the waveguide. As discussed above we can replace $\gamma$ given by equation 4.7 with the adjusted value of $\gamma$ given be equation 4.28 to calculate the reflection.

### 4.4.5 Data normalization and presentation

As described above the experimental measurements were performed so that from the data we can extract the conductivity of the $TiO_2$ semiconductor. The experimental data are presented in terms of the normalized reflection coefficient (R($\sigma$)) given by [96],

$$R(\sigma) = \frac{\Delta P(\sigma)}{P(\sigma)} \tag{4.29}$$

where P($\sigma$) is the reflected microwave power and $\Delta$P($\sigma$) the change in the reflected microwave power due to the change in conductivity of the cell on illumination.

The reflection coefficient $R'(\sigma)$ is also defined as the ratio between change in the reflected microwave power $\Delta P(\sigma)$ and incident power $P_{in}$ as [92],

$$R'(\sigma) = \frac{\Delta P(\sigma)}{P_{in}} \tag{4.30}$$

The numerical calculation yields R($\sigma$), $\Delta R(\sigma)$, $\frac{\Delta R(\sigma_{light})}{R(\sigma_{dark})}$ for uniform $\Delta\sigma$ [93], where

$$\Delta R(\sigma) = R(\sigma_{light}) - R(\sigma_{dark}) \tag{4.31}$$

and

The photomodulated reflectivity is given by,

$$\frac{\Delta R(\sigma_{light})}{R(\sigma_{dark})} = \frac{[R(\sigma_{light}) - R(\sigma_{dark})]}{R(\sigma_{dark})} = A\Delta\sigma \tag{4.32}$$

where $A$ is a proportionality constant, R($\sigma_{dark}$) is the reflection coefficient at the dark conductivity and R($\sigma_{light}$) is the reflection coefficient under illumination. Following the experimental measurements the dark conductivity value was estimated as $\sigma_{dark}$ = $10^{-13}\Omega^{-1}\mathrm{m}^{-1}$ and the illumination conductivity ($\sigma_{light}$) range was defined between $10^{-3}$ and 10 $\Omega^{-1}\mathrm{m}^{-1}$. The proportionality constant $A$ can be calculated from the slope of the photomodulated reflectivity as a function of photoconductivity [93]. The

proportionality constant is one of the most important calculations in this chapter as it is used later to deduce the photoconductivity of the $TiO_2$ using the experimental results.

To quantify the charge carrier kinetics two types of measurements were performed: measurements of dark reflection coefficient ($R(\sigma_{dark})$) as a function of device structure and material properties and the photomodulated measurements [108].

### 4.4.6 General case

As discussed above in section 4.4, it is possible to calculate the reflection coefficient for a single layer and multilayered structure. The problem encountered is that there will be different modes involved during the reflection and it is not easy to determine the number of the propagating modes. We calculate the reflection coefficient for the single mode propagated by the waveguide.

## 4.5 Calculations

A good way of dealing with a complex problem is to start from a simple approximation. As described in the experimental setup and measurements section the procedure used to attach the solar cell at the end of the waveguide makes it more complicated than the simple model described in the previous section. Nevertheless, we first tried to account for the data using such an approach. It is worth mentioning that comparison between the simple one dimensional (1D) model and experimental results was performed and it was unable to reproduce any experimental observations. Since this did not work, we concluded that the way that a sample was mounted necessitated a full Finite Element Methods (FEM) calculation as described here. Looking at the experimental setup, our understanding of the problem is that the microwaves travel in the waveguide until they interact with the different layers of the photocell. Some of the microwave power will be absorbed by the $TiO_2$ semiconductor layer, while some will be reflected and some will radiate from the structure. This result shows the limitation of the 1D model to explain the experimental results as it does not take into account the power escaping from sides of the structure. This is clearly illustrated by a three dimensional (3D) waveguide with a dielectric slab as described in section 4.5.2.1 below.

### 4.5.1 Model software and theory

As defined in the dye uptake in DSSCs chapter the Comsol Multiphysics software is a numerical package for finding approximate solutions of partial differential equations (PDE) as well as of integral equations, using FEM. Comsol can also be used to find the approximate solution of partial differential equations (PDE) that involves complex geometries and boundaries, such as waveguides with arbitrary cross-sections. The field volume is divided into a mesh of 3D figures such as pyramids, cylinder or rectangular boxes. The problem can be reduced from 3D to a 2D problem in which a mesh of two dimensional (2D) figures such as triangles, etc are employed. In the context of optical waveguides, the Comsol software can be used for mode solving and propagation problems. In this work the use of Comsol was appropriate to mimic the experimental geometries as illustrated above in section 4.3. The other advantage of using Comsol in this chapter is that as we will have multiple reflections from different layers, it will be simpler to use Comsol as it automatically computes the reflection coefficient.

The walls of manufactured waveguides are usually good conductors. The model approximates them as perfect electric conductors. This implies a boundary condition which sets the tangential component of the electric field to zero [50, 115], that is,

$$\mathbf{n} \times \mathbf{E} = \mathbf{0} \ , \tag{4.33}$$

where $\mathbf{E}$ is the electric field and $\mathbf{n}$ is the surface normal vector.

At the interface between the materials, for example between glass and $TiO_2$ layers we have a boundary condition that ensures the continuity of the tangential component of the electric field [50, 116], i.e.,

$$\mathbf{n} \times ( \ \mathbf{E}_1 - \mathbf{E}_2) = 0 \tag{4.34}$$

where $\mathbf{E}_1$ and $\mathbf{E}_2$ is the electric field vector for different material.

Finally the absorbing boundary condition is applied to parts of the structure which are expected to radiate microwaves. All our structures are excited by a single mode $TE_{10}$ rectangular waveguide. The waveguide is excited by the transverse electric (TE) wave, which is a wave that has no electric field components in the direction of propagation. In this work 33 GHz microwaves were used with a rectangular waveguide of 3.5 $\times$ 7 mm internal dimension. Comsol computes the scattering parameter ($S_{11}$) of the active port automatically and we can calculate the reflection coefficient (R) in terms of power. These parameters described the amplitude and phase of the waves passing through the

ports. For our purpose only the magnitude is needed to the calculate the reflected power, so the reflection coefficient was calculated as [50, 117],

$$R = S_{11}^2 \tag{4.35}$$

The 3D RF Module of Comsol version 3.5a was run on a Linux computer with 8 CPUs, speed of 3 GHz and memory of 64 GB.

### 4.5.2 Model validation

As a way of validating our Comsol calculations, several steps were followed. Firstly, the results of the analytical 1D model described in section 4.4.3 were reproduced. In addition a variety of 2D and 3D calculations were performed on more complex structures to confirm that the physical valid results were obtained.

#### 4.5.2.1 The one dimensional model and its limitation

A simple Matlab program which implements the analytical 1D theory of section 4.4.3 was written by Stephen Bingham. This model considers a rectangular waveguide filled with a slab of dielectric material. The results where compared with Comsol calculations in two cases, with and without a short as shown in figure 4.7. As illustrated in figure 4.8, it can be seen that there is good agreement between the two approaches, especially at low conductivity. The discrepancy of the 3D Comsol calculation at high conductivity can be related to the meshing which was found to be a problem during the simulation as discussed in detail in Appendix A, section A.3.2.

#### 4.5.2.2 Calculations of waveguide modes in 2D and 3D

The failure of the simple 1D model implies that microwave radiation by the structure is important as illustrated in figure 4.9. We decided to try and quantify the effects using a waveguide T-Junction that approximate the dimensions of the solar cells structure. 2D calculations are much faster than a full 3D calculations. A number of simulations were performed to verify the effect of the dielectric constant on the waveguide T-Junction structure. The T-Junction waveguide walls are all metallic, so we understand that for a symmetric structure, the wave will be distributed evenly in the parallel arms of the

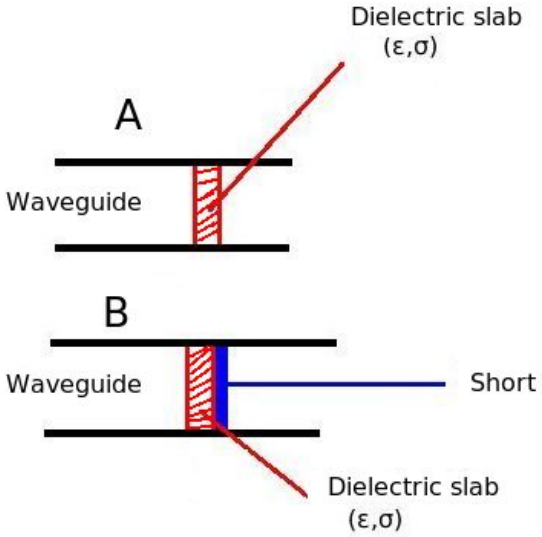


Figure 4.7: A side view of the 3D continuous waveguide with a dielectric slab inside for a case without (A) and with (B) a short.

"tee". The reflection will depend on the dimension of the waveguide structure. Figure 4.10, (B), illustrates the effects of the change in the dielectric value in parallel arm of the T-Junction waveguide. The modes are more complex than the air filled case, figure (A). A similar analysis was also carried out using a full 3D calculations illustrated in figure 4.11.

#### 4.5.2.3 Reflection calculations for simplified structure using 3D calculations

After understanding the mode distribution in a waveguide T-Junction structure in 2D and 3D, we then developed a compromise 3D geometry to calculate the reflection coefficient by varying the conductivity of the $TiO_2$ layer. This structure lacks the metal surfaces of the waveguide to which the solar cell structure is attached. It also limits the photocell structure to a simplified three layered stack. These approximations can be expected to be valid because the microwave reflection should be dominated by the highly conducting $TiO_2$ layer. The three layered structure allows this layer to be positioned at different distance from the end of the waveguide.

Apart from using the Comsol to demonstrate the limitations of the 1D model in the current work and after understanding the results and behaviour of modes in the waveguide T-Junction in 2D and 3D, there was a need to further validate the full 3D model before doing all the simulations. This was done to check that continuity between the different layers was achieved and that the model gives meaningful results. The conti-

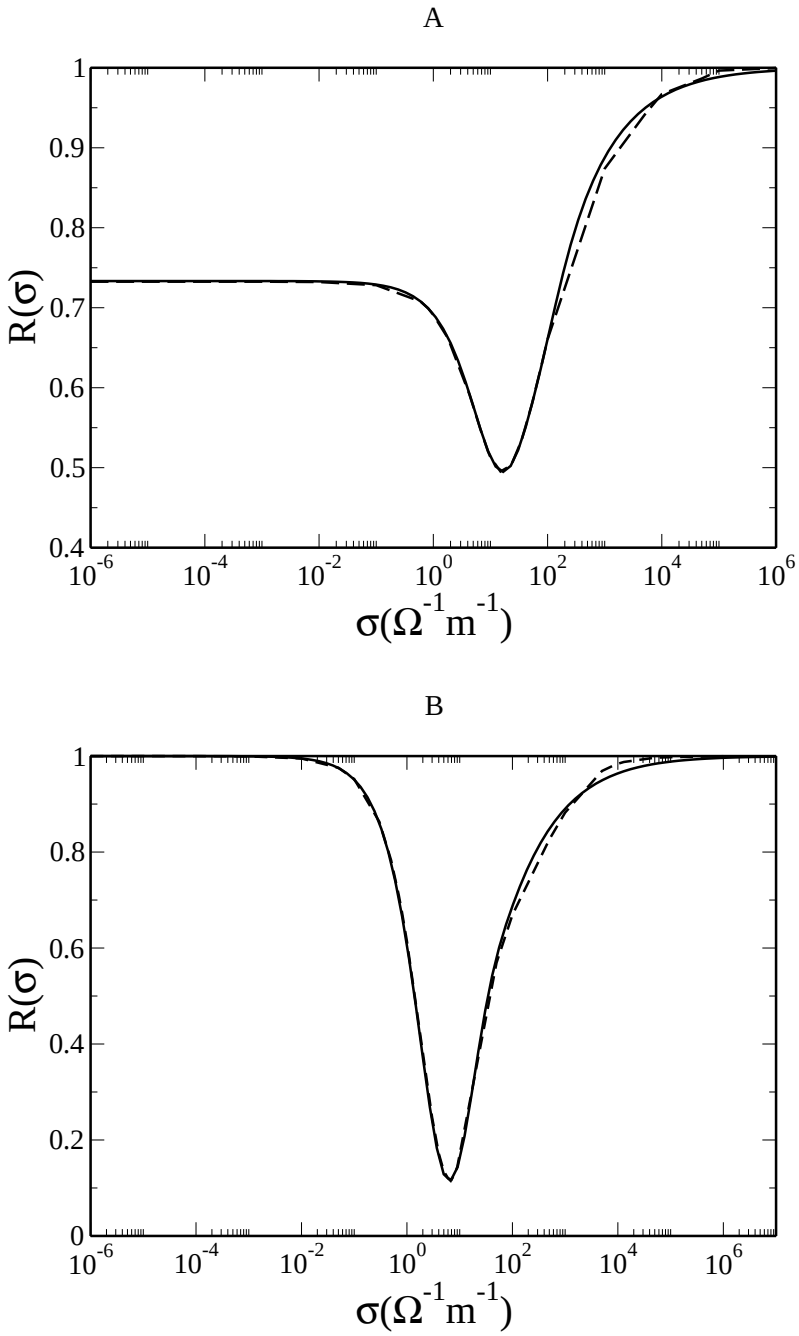


Figure 4.8: Comparison between a 1D Matlab simulations (solid line) and a 3D continuous waveguide with a slab of dielectric material inside (dashed line), for a case without a short (A) and with a short (B).

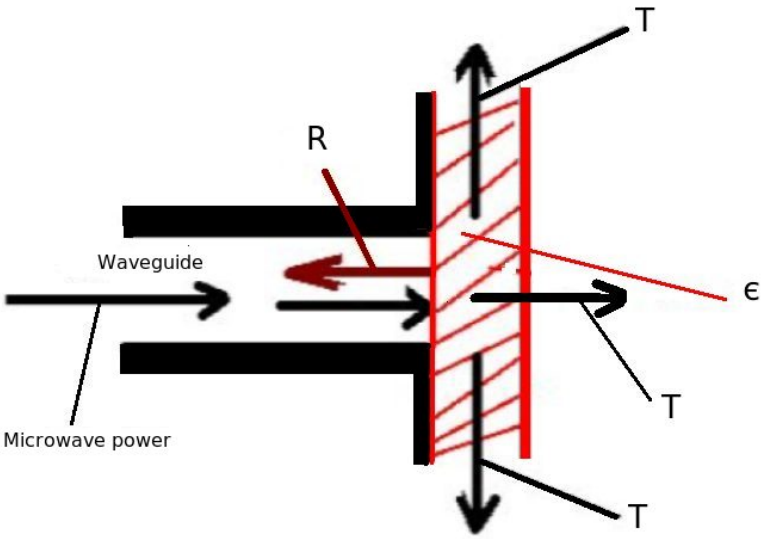


Figure 4.9: Side view of a T-Junction illustrating the reflection (R) and transmission (T) of microwave power when interacting with a dielectric constant,$\epsilon$, solar cell structure.

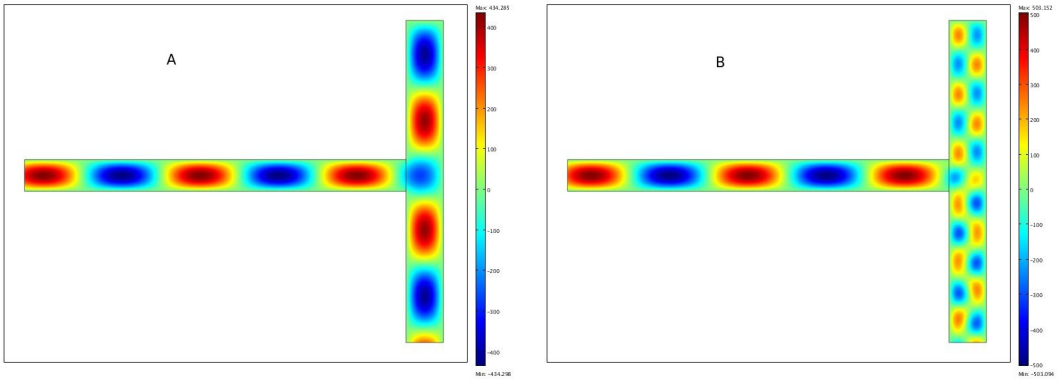


Figure 4.10: The variation of the microwave electric fields inside the waveguide T-Junction structure, for the T-Junction parallel arm filled with air (A) and for dielectric constant $\epsilon = 4$ (B).

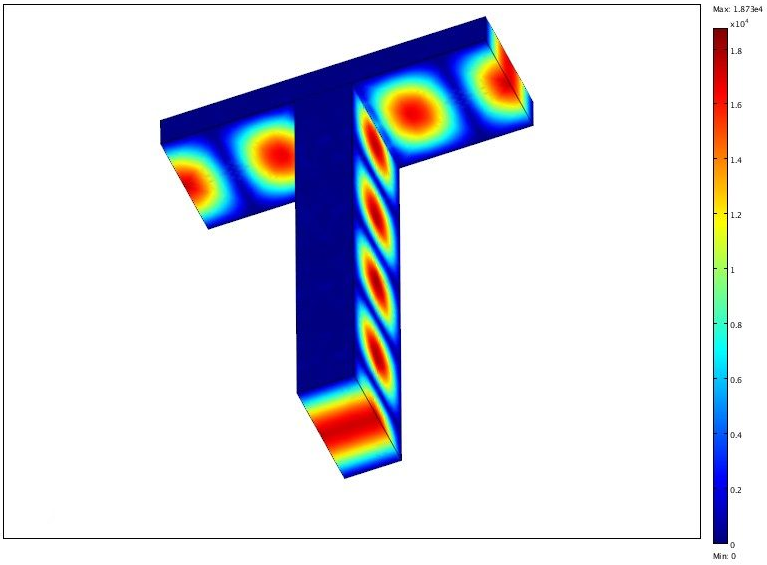


Figure 4.11: A 3D T-Junction air filled waveguide illustrating mode distribution.

nuity between the layers was one of the problems encountered during the setting up of the model as described in Appendix A.

During the calculations of reflection coefficients in the 3D model, special attention was paid to the meshing generated by Comsol, since it was found that incorrect meshing could occur. This problem results in invalid boundary conditions and hence the incorrect reflectance values. For this purpose various structures were tested with variety of material parameters such as conductivity and dielectric constant. The boundary condition on the parallel arm (glass slab and photocell) allows the microwaves to radiate through. A waveguide T-Junction with a parallel arm of a single slab glass figure 4.12, was used to calculate the reflection coefficient for comparison with the reflection coefficient of the photocell, figure 4.13. The reflection coefficient was calculated for a case when the distance $L$ of the photocell is 1mm or 2mm. The width $w$ of the glass was also varied so that it is equal to the width of the photocell.

The dielectric constant $\epsilon = 7$ was used during the simulations for comparisons. For the model structure figure 4.13, a test was made on the thinner layer for a low ($\sigma_L$) and high ($\sigma_H$) conductivity. The value of conductivity was chosen from the fact that at low conductivity we know that the reflection coefficient will be a function of the structure and at high conductivity the photocell behaves as though it only consist of one layer and the reflection coefficient will be a function of structure again. Table 4.1 show the results for the two cases. It can be observed that there is good agreement between the two geometries and this demonstrates that the continuity between the different layers was achieved.

| Width of photocell $w$ | 2.013mm | 3.013mm | 1mm | 2mm |
|---|---|---|---|---|
| Glass | 0.6832442 | 0.70053685 | 0.365502 | 0.8097474 |
| Photocell ($\sigma_L$) | 0.66018766 | 0.70282906 | | |
| Photocell ($\sigma_H$) | | | 0.3772502 | 0.8134665 |

Table 4.1: Reflection coefficient calculated from a single glass slab, figure 4.12 and photocell figure 4.13 , for $\sigma_L = 1\times\ 10^{-13}\Omega^{-1}\mathrm{m}^{-1}$ and $\sigma_H = 1\times\ 10^{9}\Omega^{-1}\mathrm{m}^{-1}$ in the middle layer of the photocell.

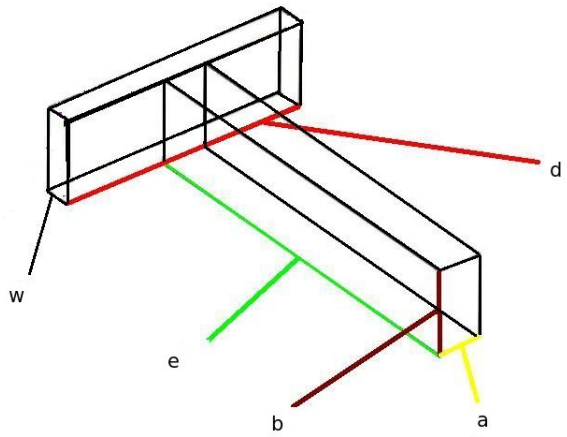


Figure 4.12: A waveguide T-Junction where the parallel arm length is a slab of a glass. The height of the waveguide $b$=7mm, the width $a$ = 3.5mm, parallel arm length $d$ = 2 cm, exciting waveguide length $e$ = 3 cm.

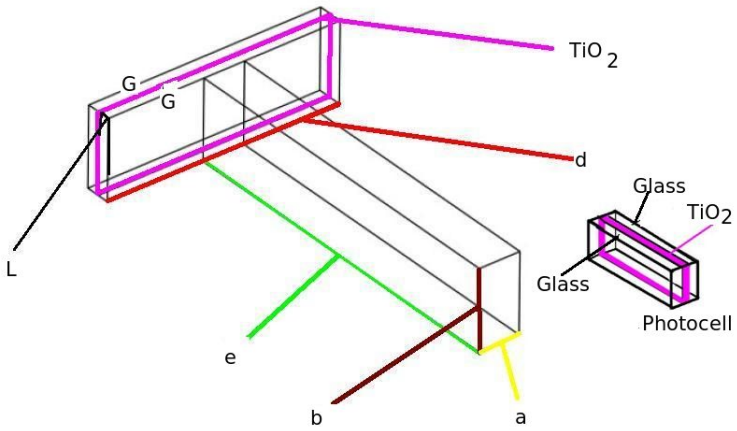


Figure 4.13: The modeling geometry structure with an inserted view of the photocell used. The height of the waveguide ($b$)= 7mm, the width ($a$)= 3.5mm, $L$ is the distance varying between 1mm and 2mm for device1 and device2 respectively, $G$ represents a glass layer of 1mm thickness, parallel arm length $d$ = 2cm, exciting waveguide length $e$ = 3cm and the $TiO_2$ = 13 $\mu$m.

### 4.5.3 Results

#### 4.5.3.1 Unmodulated reflectivity

Although our primary goal is to simulate the photomodulated reflectivity experiments of Dunn *et .al* [108], the simulations have to be based upon the simpler unmodulated case. Our first task therefore was to calculate the reflectivity as a function of geometry and material parameters. The results below are based on the approximate 3D geometry, where we have a waveguide and photocell with three layers, 1mm glass, 13 $\mu$m $TiO_2$ and 1mm glass with a optional layer which acts as a short (high conductivity layer behind the photocell) as illustrated in figure 4.13. The glass dielectric constant is $\epsilon$ = 7, and we assume that the glass does not absorb any microwave power. The boundary conditions employed in these calculations were the same as in section 4.5.2.3 above.

**4.5.3.1.1 Geometry dependence** Experimental measurements of the dark reflection coefficient (R($\sigma$)) for different geometries of the solar cells were carried out, by inserting a variable number of 1mm glass layers between the waveguide end and the basic structure of figure 4.2, (B). To mimic the experimental measurements simulations were therefore performed by varying distance $L$ in figure 4.13 by 1mm to study the geometry dependence. As illustrated in figure 4.14 varying the distance $L$ causes

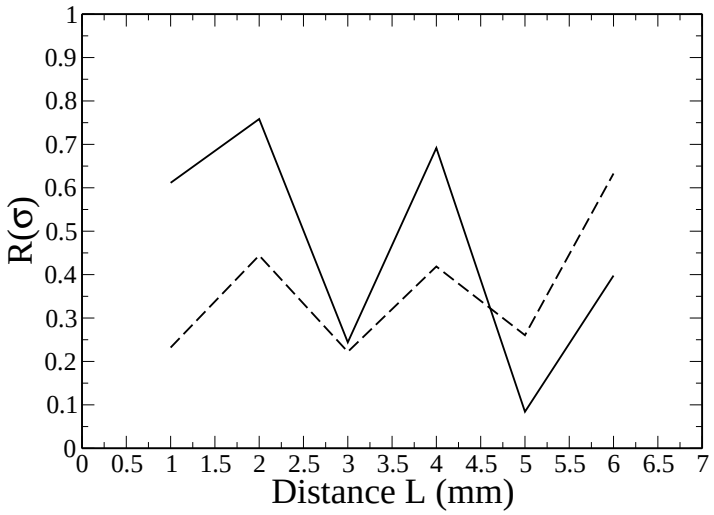


Figure 4.14: The effect of changing the geometry on the reflection coefficient, calculated with a short (solid line) and without a short (dashed line), with experimental results (filled circle) for a case without a short. The value used are $\epsilon = 20$ and $\sigma = 1\times 10^{-13}\Omega^{-1}\mathrm{m}^{-1}$.

oscillations in R($\sigma$). Placing a conducting short behind the structure increases the magnitude of this variation. The probable cause of these oscillations is interference effects within the structure similar to those described in section 4.4.3 above. It is evident from figure 4.13 that the reflection coefficient depends on the structure.

**4.5.3.1.2 Material property dependence in specific device structure** After studying the geometry dependence of the reflection coefficient by looking at the dark conductivity, simulations were performed to study the effect of varying material parameter, such as conductivity and dielectric constant to a few specific device geometries. Only two geometries were used: Device1 has a 1mm glass layer between the active $TiO_2$ semiconductor layer and the waveguide. In device2 this distance is 2mm. For both devices, calculations with and without a short behind the photocell were performed.

The simulation results of reflection coefficient in figures 4.16 (A) and (B), show that it is convenient to divide the results into three conductivity ranges for discussion, low conductivity range,transition range and high conductivity range. The low conductivity range is defined as the range where the reflection coefficient is independent of the change in conductivity because all microwaves pass straight through the $TiO_2$ layer. The high conductivity range is defined as the range where the reflection coefficient also becomes

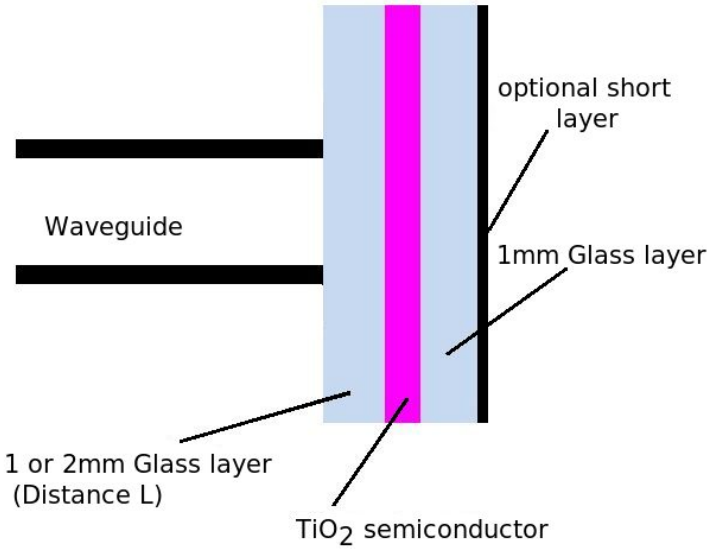


Figure 4.15: A side view of the modeling structure, illustrating how the two devices are achieved by varying the distance $L$ between 1mm and 2mm as illustrated and also the optional layer which acts as a short

independent of conductivity as the active $TiO_2$ layer reflects all the microwaves. The transition range is defined as the intermediate range where the reflection coefficient has a complex dependence on the conductivity. Figures 4.16, illustrates how the reflection coefficient varies with the conductivity for device1, (A), and device2, (B), clearly showing the different ranges. In this work we are most interested in the low conductivity range as is the experimental relevant range. All the discussion of the results are based on an experimental light conductivity range of $1\times\ 10^{-3}$ and 10 $\Omega^{-1}$ $m^{-1}$.

Figure 4.16 shows calculated reflection coefficient ($R(\sigma)$), for different dielectric constants for the sample, with and without a short. The results are illustrated for device1, (A) and device2, (B). The figure illustrates that the reflection coefficient is a function of the electrical conductivity and the dielectric constant. It is also clear from the figure that, for a given electrical conductivity and dielectric value, we get different reflection coefficients depending on the geometry of photocell structure. It is relevant to compare this results with those of the simple Kunst and Beck [92] 1D model calculations in figure 4.8. The qualitative difference between our calculations and the Kunst and Beck model are probably due to the complications of radiating microwaves from the structure. The absence of reflection minimum for some dielectric constant is discussed below.

For the case without a short our results illustrate that at low conductivity the photocell become transparent to microwaves. Most microwaves will reach the back of the photocell and escape into the environment. The reflection coefficient is independent

A

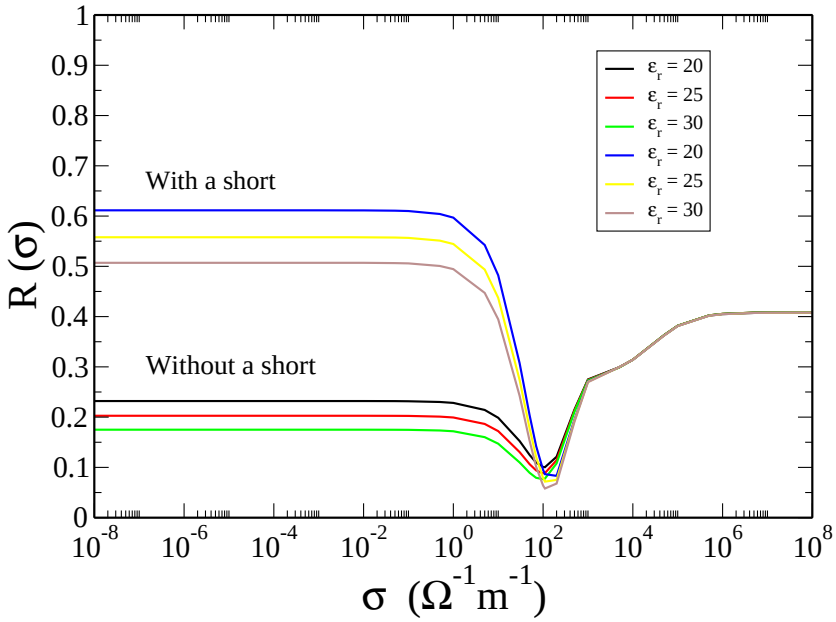


B

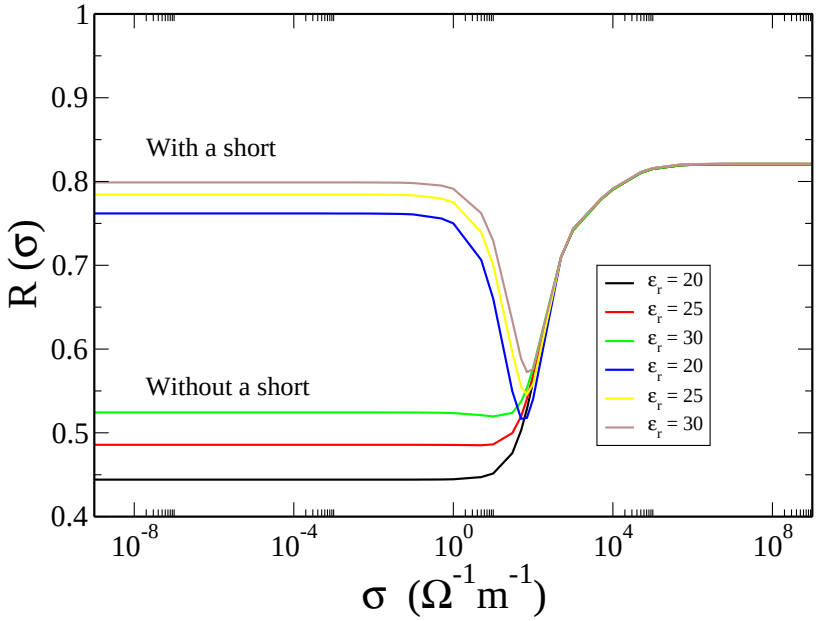


Figure 4.16: Reflection coefficient as a function of conductivity for device1, (A), and device2, (B), without a short and with a short respectively, for different values of dielectric constant ($\epsilon$) as shown.

of the change in $TiO_2$ electrical conductivity at this low range. As the conductivity increases we reach a range where the reflection coefficient decreases. The same effects are observed in the Kunst and Beck case [92] and like that case it is probably due to microwave absorption by the structure. The graph also shows that there is a value of the conductivity where we reach a minimum in the reflection coefficient for both devices for most values of the dielectric constant. This minimum value of the reflection coefficient depends on the photocell geometry as illustrated in figure 4.16. After this value the reflection coefficient increases, until a range where it is again independent of conductivity. At this high conductivity range the active $TiO_2$ semiconductor layer behaves like a metal and all microwave power is reflected back. At this stage the model is effectively reduced to two layers only, i.e., the high conductivity $TiO_2$ layer and glass. The reflection coefficient is now a function of the thickness of the glass layer.

For the case with a conducting short, at low conductivity the photocell is transparent to microwaves and most of the power will reach the back of the photocell and be reflected back. As the conductivity increases we again reach a transition where the sample starts to absorb the microwave power and there is a decrease in the reflection coefficient. The reflection coefficient decreases with increasing conductivity until we reach a stage where we have a minimum which depends on the geometry of the sample. After this minimum value the reflection starts to increase because the photocell starts to reflect more microwave power and the $TiO_2$ layer starts to behave more like a metallic layer. The reflection increases until it reaches a high constant value since all the microwaves are reflected back by the conducting $TiO_2$ layer. At this range of conductivity the reflected power reaches a constant value independent of the change in conductivity. In this range the presence of a short no longer affects the reflection coefficient.

The $TiO_2$ dielectric constant also plays an important role in determining the reflection coefficient as shown in figure 4.17. The reflection coefficient for the case without a short is always less than with a short. For device1 ($L = 1$mm) the reflection coefficient decreases with increasing dielectric constant, while for device2 ($L = 2$mm) it increases. This shows that the reflection coefficient depends on both the structure and the dielectric constant of the $TiO_2$ semiconductor. The same conclusion was reached by Spada *et al.* [118]. The results suggest that microwave reflection techniques can be used to calculate the dielectric constant of the porous $TiO_2$ semiconductor at microwave frequencies.

In summary as shown in figure 4.16 the reflection coefficient ($R(\sigma)$) depends on the structure, electrical conductivity and the dielectric constant. For device1, the reflection coefficient is lower compared to device2 for both cases (with and without a short). The minima in the reflection coefficients differ for the two devices. For device1 the reflectance minima are between 90 and 120 $\Omega^{-1}m^{-1}$ and for device2 the minima are

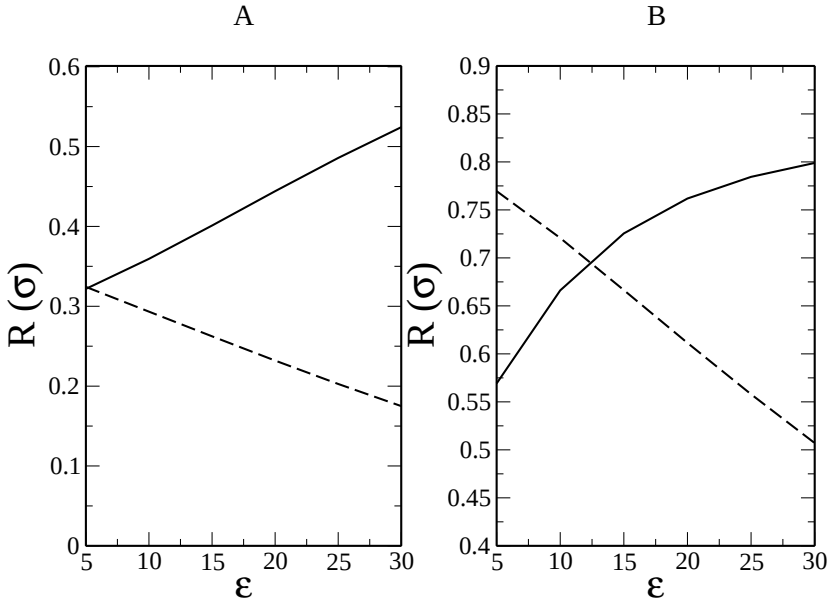


Figure 4.17: The dependence of reflection coefficient (R($\sigma$)) on the dielectric constant ($\epsilon$), for the device1 (dashed line) and device2 (solid line) without a short (A) and with a short (B), the value of the conductivity used $\sigma = 1\times\ 10^{-13}\Omega^{-1}\mathrm{m}^{-1}$.

between 70 and 90 $\Omega^{-1}\mathrm{m}^{-1}$. The dependence of the reflection coefficient on the dielectric constant differs for each device as shown in figure 4.16. For device1 an increase in the dielectric value reduces the reflection coefficient, while for device2 it increases.

#### 4.5.3.2 Photomodulated reflectivity

The normalized photomodulated reflectivity ($\frac{\Delta R(\sigma_{light})}{R(\sigma_{dark})}$) can be determined via the change in the reflection coefficient under illumination compared to the dark [97]. As discussed under the data normalization and presentation section, the proportionality constant ($A$) can be used to relate the experimentally measured reflected microwave power to the conductivity and hence to understand the relation between the conductivity and illumination. In the current work $\frac{\Delta R(\sigma_{light})}{R(\sigma_{dark})}$ is calculated using equation 4.32.

$\frac{\Delta R(\sigma_{light})}{R(\sigma_{dark})}$ also follows similar trend of the three ranges of conductivities, i.e., low light conductivity, transition and high light conductivity ranges discussed above. For experimental relevant conductivities we can assume that the conductivity of $TiO_2$ is in the low range. Our calculations study the effects of varying the $TiO_2$ dielectric constant for the two geometries referred as device1 and device2, above.

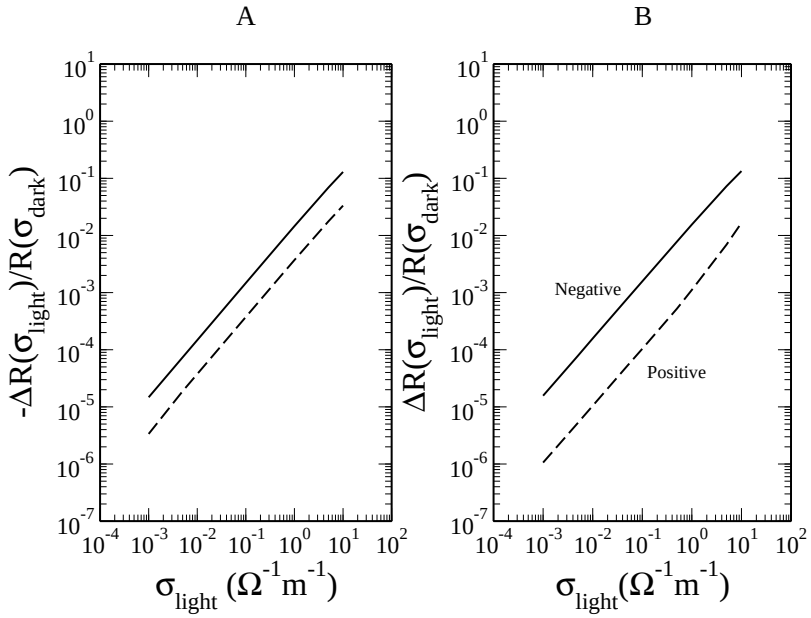


Figure 4.18: -$\frac{\Delta R(\sigma_{light})}{R(\sigma_{dark})}$ as a function of light conductivity for device1, (A) and $\frac{\Delta R(\sigma_{light})}{R(\sigma_{dark})}$ for device2 with different sign, (B), for the case without a short (dashed line) and with a short (solid line). The dielectric constant $\epsilon = 20$.

Figure 4.18, (A), compares $\frac{\Delta R(\sigma_{light})}{R(\sigma_{dark})}$ for device1, with and without a short. It can be observed that for both cases we have a linear relationship between $\frac{\Delta R(\sigma_{light})}{R(\sigma_{dark})}$ and the light conductivity. $\frac{\Delta R(\sigma_{light})}{R(\sigma_{dark})}$ is greater with a short. Figure 4.18, (B), shows the calculations for Device2. Although the calculation with a short is qualitatively similar to that of device1, the behavior of device2 without a short is fundamentally different. $\frac{\Delta R(\sigma_{light})}{R(\sigma_{dark})}$ is positive. The difference can be understood from the unmodulated reflectivity simulations in figure 4.16.

Simulations were performed to study $\frac{\Delta R(\sigma_{light})}{R(\sigma_{dark})}$ for different dielectric constants, figures 4.19 and 4.20. It can be observed that the $\frac{\Delta R(\sigma_{light})}{R(\sigma_{dark})}$ of device1 is less sensitive to $\epsilon$ than device2. Figure 4.19 of device1 shows that in the low conductivity range $\frac{\Delta R(\sigma_{light})}{R(\sigma_{dark})}$ is linearly dependent on the light conductivity ($\sigma_{light}$). But for device2, figure 4.20, it can be further observed that the linear behaviour of $\frac{\Delta R(\sigma_{light})}{R(\sigma_{dark})}$ depends on the dielectric value. For example at a conductivity of 5 $\Omega^{-1}\mathrm{m}^{-1}$ for $\epsilon = 25$ we start to reach the transition range, where $\frac{\Delta R(\sigma)}{R(\sigma)}$ is no longer a linear function of $\sigma_{light}$. For $\epsilon = 30$ this transition occurs at higher $\sigma_{light}$ (10 $\Omega^{-1}\mathrm{m}^{-1}$). Figure 4.21 illustrates the effect of varying the dielectric constant on $\frac{\Delta R(\sigma_{light})}{R(\sigma_{dark})}$ for a fixed $\sigma_{light}$ of $5\Omega^{-1}\mathrm{m}^{-1}$. As discussed above the reflection coefficient is a function of dielectric constant and we expect also that $\frac{\Delta R(\sigma_{light})}{R(\sigma_{dark})}$ is affected by this.

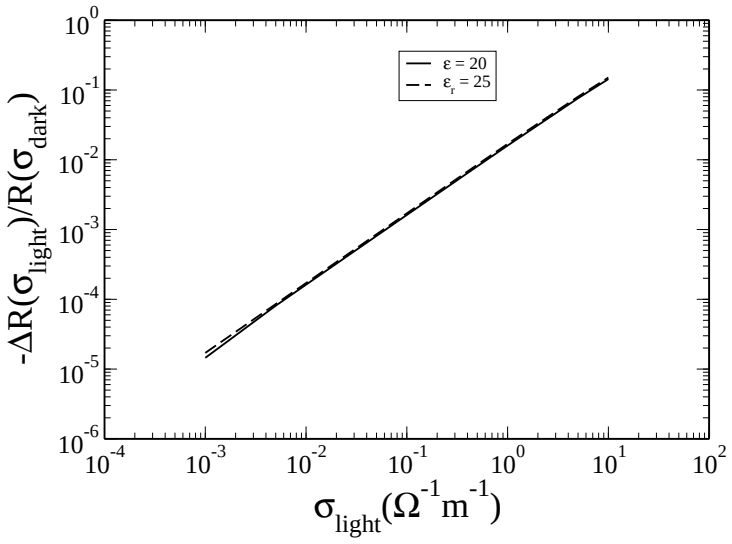


Figure 4.19: $-\frac{\Delta R(\sigma_{light})}{R(\sigma_{dark})}$ as a function of light conductivity for device1 ($L$ = 1mm) without a short, for different values of dielectric constant ($\epsilon_r$) as shown. For $\epsilon = 30$ the $-\frac{\Delta R(\sigma_{light})}{R(\sigma_{dark})}$ lies just above $\epsilon = 25$.

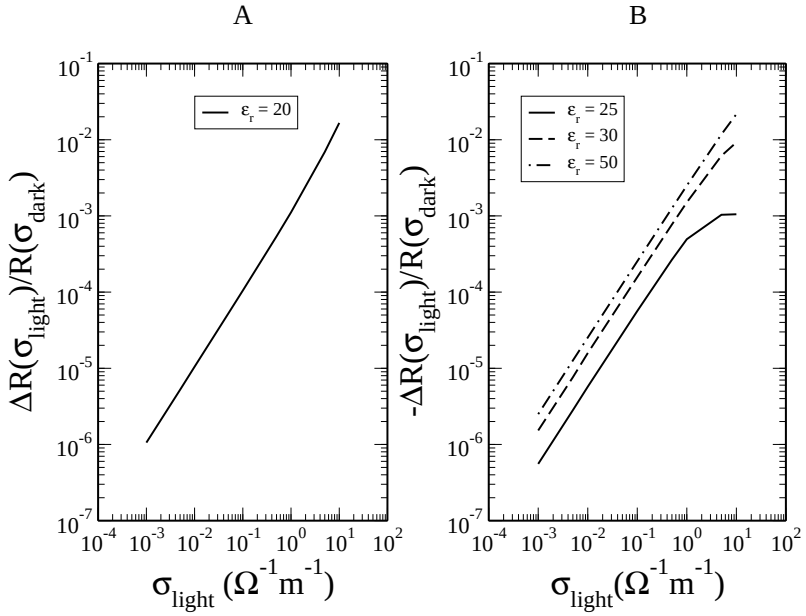


Figure 4.20: $\frac{\Delta R(\sigma_{light})}{R(\sigma_{dark})}$ as a function of light conductivity for device2, without a short for different values of dielectric constant ($\epsilon$), with different sign, that is, positive on (A) and negative (B) as indicated.

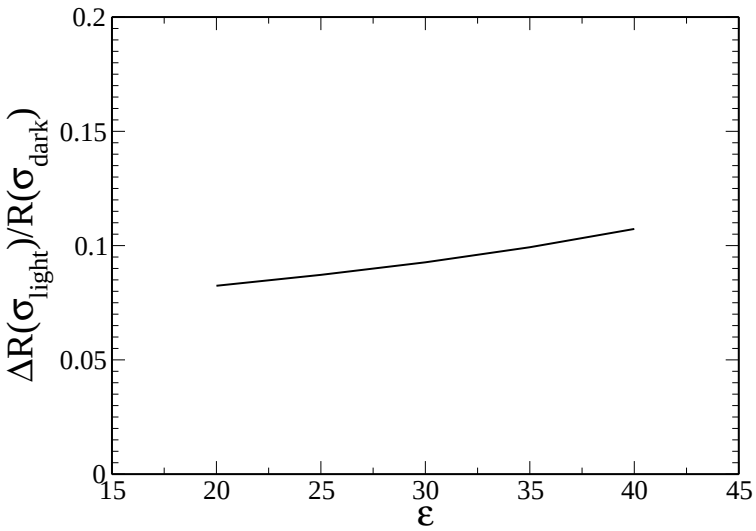


Figure 4.21: $\frac{\Delta R(\sigma_{light})}{R(\sigma_{dark})}$ as a function of dielectric constant ($\epsilon$) for device1, without a short, for a fixed light conductivity value of $5\Omega^{-1}\mathrm{m}^{-1}$.

Our modelling results show a change in sign of $\frac{\Delta R(\sigma_{light})}{R(\sigma_{dark})}$, between the two devices, for $\epsilon = 20$. Using this value we obtain a negative $\frac{\Delta R(\sigma_{light})}{R(\sigma_{dark})}$ for device1 and a positive value for device2. The same change in sign was observed experimentally as will be discussed in section 4.6.1 below. Figure 4.20 shows a change in sign of $\frac{\Delta R(\sigma)}{R(\sigma)}$ for different dielectric values. For $\epsilon = 20$ we get a positive sign and for $\epsilon \geq 25$ is negative. The small magnitude and non-linearity of the $\epsilon = 25$ simulations suggests that it may be close to the value of $\epsilon$ at which the sign changes. In general this results show that there can exist a value of $\epsilon$ between 20 and 25 which can give a zero $\frac{\Delta R(\sigma_{light})}{R(\sigma_{dark})}$ and also a value which will give a nonlinear relation between $\frac{\Delta R(\sigma_{light})}{R(\sigma_{dark})}$ and conductivity. A minimum in $R(\sigma)$ curve leads to a negative $\frac{\Delta R(\sigma_{light})}{R(\sigma_{dark})}$, see figure 4.16 (B). For a large $\epsilon = 30$ the effect is exaggerated further as clearly illustrated in 4.16 (B).

In summary the interesting difference between device1 and device2 is that we were able to observe the change in sign of $\frac{\Delta R(\sigma_{light})}{R(\sigma_{dark})}$ by varying $\epsilon$ for device2 but not for device1. This is an interesting result as we might expect to see a change in sign on $\frac{\Delta R(\sigma_{light})}{R(\sigma_{dark})}$ for different devices rather than single device. The linearity of $\frac{\Delta R(\sigma_{light})}{R(\sigma_{dark})}$ will depend on the device geometry and the dielectric constant.

## 4.6 Comparison with experimental results

Experimental measurements of the microwave reflectivity were made by Halina Dunn [108] on the structure which was very close to that of a normal functioning DSSC. The basic structure is shown in figure 4.2, (B). In this section we compare the modelling described in the previous section to these experimental results.

### 4.6.1 Dependence on device structure and material properties

Figure 4.22 compares the modelling and experimental results of the photomodulated reflectivity ($\frac{\Delta R(\sigma_{light})}{R(\sigma_{dark})}$) for different geometries. Experimentally the different geometries were achieved by inserting a variable number of 1mm glass layers between the waveguide and the basic structure of figure 4.2, (B). The theoretical results were able to demonstrate the change in sign of $\frac{\Delta R(\sigma_{light})}{R(\sigma_{dark})}$ for the different geometries as illustrated in the figure when the dielectric value is 20. The good agreement in the sign change between the simulation and experimental results shows that microwave reflection can be used to measure the dielectric constant of the porous $TiO_2$ semiconductor. When using other values of the dielectric constant (for example $\epsilon$ = 25,30), we were unable to see a change of sign in $\frac{\Delta R(\sigma_{light})}{R(\sigma_{dark})}$. It was tempting to conclude that the dielectric constant of the $TiO_2$ is about 20, but we know that the presence of electrolyte will affect this value.

Table 4.2 compares the experimental and modelling results of the dark reflection coefficient ($R(\sigma_{dark})$) for different value of $L$ (the distance between the waveguide and the $TiO_2$ layer). The experimental $R(\sigma_{dark})$ (0.2408) and the value calculated (0.2320) for L = 1mm (equivalent to device1) is in good agreement. It is likely that the small disagreement in the experimental and modelling results for different values of $L$ is because the modelling does not fully consider all the complications in the experimental arrangement like other layers of the solar cell, positioning of the sample at the waveguide end, etc.

### 4.6.2 Non-ideality in the light intensity dependencies

There has been much discussion recently about non-ideal behaviour of DSCs [21, 29, 75]. In an ideal DSC, the intensity dependence of the DSC photovoltage is given by

$$\frac{\mathrm{d}V_{oc}}{\mathrm{d}\log_{10} I_0} = 2.303m\frac{k_B T}{q} \tag{4.36}$$

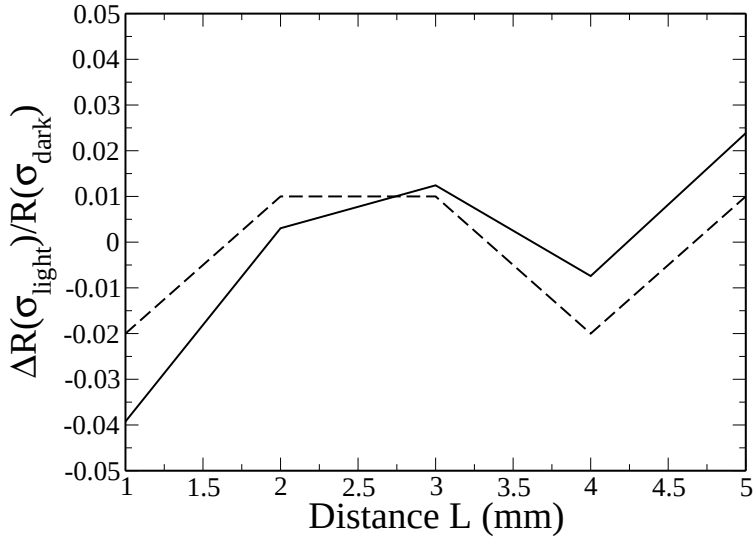


Figure 4.22: Comparison between the modelled (solid line) and experimental (dashed line) $\frac{\Delta R(\sigma_{light})}{R(\sigma_{dark})}$ for different geometries (achieved by varying $L$ (mm) in figure 4.13) without a short. The modelling parameters used are $\epsilon = 20$ and the dark and light conductivity of the $TiO_2$ layer are $10^{-13}$ and 5 $\Omega^{-1}m^{-1}$ respectively.

| Distance ($L$ mm) | Experimental | Modelling |
|---|---|---|
| 1 | 0.2408 | 0.2320 |
| 2 | 0.4870 | 0.4441 |
| 3 | 0.3422 | 0.2923 |
| 4 | 0.4856 | 0.4387 |

Table 4.2: Comparison of experimental dark reflection coefficient ($R(\sigma_{dark})$) and the values calculated for different geometries (achieved by varying $L$ in figure 4.13). The modeling values are calculated using the dielectric value ($\epsilon$) = 20 and the electrical conductivity of the $TiO_2$ layer equal to $10^{-13}\Omega^{-1}m^{-1}$.

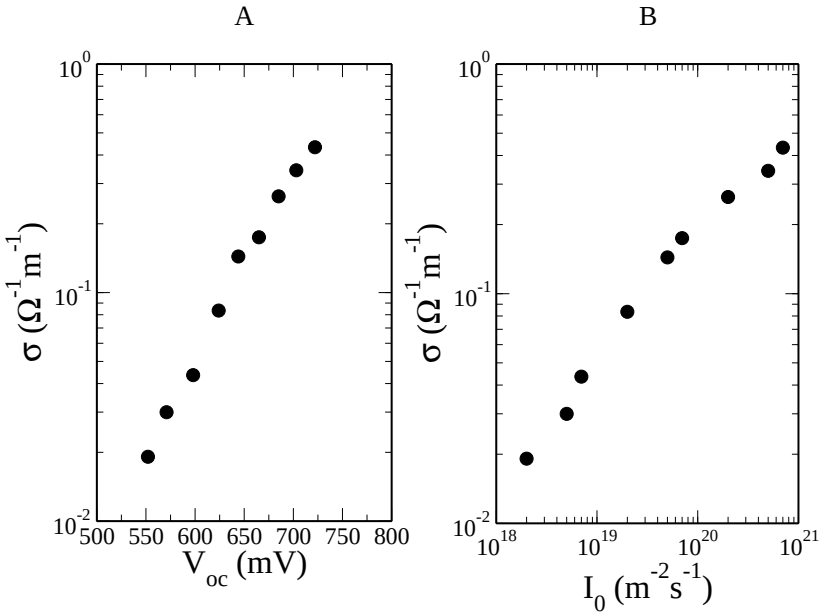


Figure 4.23: Experimental results: Variation of photoconductivity with open circuit voltage (A) and variation of photoconductivity with light intensity (B) [108].

where the factor 2.303 is $\log_{10}(e)$ and the ideality factor $m = 1$. This result can be straightforwardly obtained from equation (3.29). At room temperature, $T$=300K, $k_BT$=0.026 eV so a plot of $V_{oc}$ vs $\log_{10}I_0$ will give a slope of 59 mV/decade. However, most DSCs are not ideal: generally Uphoto increases by more than 59 mV/decade, and values as large as 120 mV/decade are not uncommon. Nonideal behaviour has been shown empirically to correspond to values of $m$ exceeding unity, so that for example, if $m$=2, the slope becomes 118 mV/decade.

As shown in equation 4.1, the photoconductivity $\sigma$ depends on the product $n_c\mu_e$. From equation (3.3), $n_c \propto I_0$ and from the Einstein relationship, $\mu_e \propto D_0$ in the steady state and $\mu_e \propto D_n$ for transient behaviour. The microwave experiments were conducted for steady state illumination, so $\mu_e \propto D_0$. Since $D_0$ is independent of the intensity, $\sigma \propto n_c$ and so measurements of $\sigma$ at different light intensities can be used to deduce how $n_c$ varies with $I_0$ and hence if the solar cell is ideal or not.

Our simulation results show, for a variety of structures and for experimental relevent material parameters that the microwave reflectivity is proportional to the $TiO_2$ conductivity. In other words, the parameter $A$ is a constant (see figure 4.19) that is independent of conductivity. Figure 4.24, open circles, shows plot of conductivity calculated from the proportionality constant $A$ generated by our simulations for device1. However these plots are not fully consistent with the relation between the conductivity and free electron density equation 4.1 and also the assumption made see section 4.2

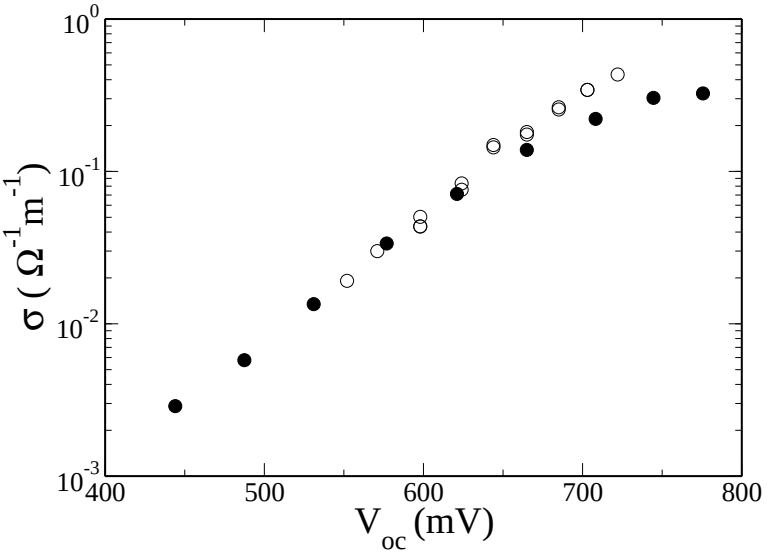


Figure 4.24: Comparison between the experimental conductivity results using cyclic voltammetry measurements (filled circle) and microwave results calculated using proportional constant $A$ (empty circle) as a function of open circuit voltage ($V_{0c}$).

above. These discrepancies are being investigated at present. One possibility is that the assumption made that the trapped or bound charges do not affect the microwave reflection is incorrect. Recent measurements of conductivity using the alternative methods of cyclic voltammetry across a gap in the electrode in contact with the $TiO_2$ suggest that some discrepancy exists with the microwave reflectivity measurements as illustrated in figure 4.24.

Figure 4.24 illustrates the fact that the microwave reflectivity is sensitive to trapped electrons in addition to the conduction electron density. Therefore further work is needed to interpret this data.

## 4.7 Conclusions

Both the unmodulated and modulated reflectivity affects have been calculated by solving a three-dimensional multilayer system using Maxwell's equations. The dependence of the reflection coefficient on the conductivity, the structure geometry and the dielectric constant were discussed. The results show that the reflection coefficient is a function of all these parameters and the microwave frequency used. By comparing the behaviour of the photomodulated reflectivity results for the sample with and without a short we have demonstrated that the photomodulated reflectivity is always higher for a structure with a short. The photomodulated reflectivity simulation and the experimental results for different geometries were compared and show good agreement. Overall our results show that microwave reflectivity can be used to calculate the conductivity and the dielectric value of porous $TiO_2$ semiconductors at microwave frequencies.

Future work

The aspects of the experimental results which cannot be explained by the modelling suggests that further calculations would be worthwhile. As the modelling geometry used is an approximation to the experimental setup, a better geometry needs to be developed which includes all the experimental features such as including all the other layers and taking better consideration of the mounting of the cell, etc. Apart from geometry, the main assumption of this work was that the majority of the reflection is due to conductivity. Consequently we need to also include the effect of the changes in bound charges in the modelling. Apart from the modelling, experiment has to be repeated using a better arrangement rather than the complex arrangement used as described in this work. For example, a simple arrangement of measuring the conductivity of the $TiO_2$ can be done by using the photocell example of the modelling. Further experimental work will be done on a fully working dye sensitized solar cell by a DSSCs reseach group in Uppsala University, Sweden to measure the dielectric constant of the dye sensitized solar cell at different microwave frequency ranges. This will simplify the modelling as we will be able to know the correct dielectric value.

# Chapter 5

# Overall Discusion and Conclusions

## 5.1 Dye uptake in DSSCs

The model presented for dye uptake in DSSCs shows that it can take a few hours for the dye molecules to be adsorbed onto a nanotube $TiO_2$ film, in agreement with experimental results. The comparison between the dye uptake simulations and experimental results give evidence for the fact that during the process of dye uptake, we are changing the surroundings and coverage of the $TiO_2$ film and this lowers the diffusion rate. Thus as described by Nestle and Kimmich the diffusion coefficient can be taken to vary with the change of concentration in the $TiO_2$ film and it can be described as a concentration dependent diffusion coefficient [119]. This is a significant result as it creates a stepping stone of understanding the dye uptake process in dye sensitized solar cells. Currently more attention has been given to understand this process and to achieve a reliable way of optimizing the uptake time. Much work is in progress to develop new light absorbing dyes to try and extend dye absorption to the near infred [120]. Even if an improvement on the efficiency can be achieved by changing the structure of the dye or getting a new type of dye the optimum dye uptake time still needs to be achieved. Here we have shown factors that are important on the dye uptake process and there is a need to understand them further to get a better way of minimizing the dye uptake time.

In general our model of the dye uptake in DSSCs was based on the assumption of dye molecules flowing inside the nanotube as the adsorption and desorption takes place. From the $TiO_2$ nanotube film as illustrated in figure 2.2, it is is clear that the dye molecules can also stick on the outside of the nanotubes. The condition of the dye

molecules to be adsorbed on the outside of the nanotubes are based on two facts of the space between the nanotubes,

1. If the space between the nanotubes is not enough for the dye molecule to diffuse in, there will be no adsorption of the dye molecules on the outside walls
2. If the space is wide enough the dye molecules will diffuse and there will be adsorption of dye molecules on the outside of the nanotubes

In future we need to account for the dye molecules that are adsorbed on the outside of the nanotubes.

## 5.2 Electron diffusion length in DSSCs

The most important conclusion which was reached from this thesis is that in the multiple trapping model the free electron diffusion length ($L_0$) is almost equal to the effective electron diffusion length ($L_n$) and estimated to be significantly greater than the film thickness (d). In fact, the good agreement between the IMPS experimental results and multiple trapping model IMPS solution is good evidence that the multiple trapping model can be used as a tool to explain the electron transport in the dye sensitized solar cells. The only condition needed to be followed for this conclusion is to calculate the effective electron diffusion coefficient and life time at the same quasi Fermi levels or is to adhere to the same conditions and assumptions during experimental measurements.

From the numerical IMPS calculation of electron diffusion length, we were able to show that the electron transition time constant ($\tau_{tr}$) is related to the effective diffusion coefficient as also experimentally described by Jennings *et al.* [29] and Dunn *et al.* [79]. This is a significant result, since the electron transient time in DSSCs is important as it determines the electron diffusion coefficient under short circuit condition. Our results also validate that the experimental methods of measuring the transport times using intensity modulated photocurrent spectroscopy, under short-circuit conditions is correct. Recently Jennings *et al* [66] during their study of different techniques to estimate the value of electron diffusion length, reached the conclusion that the multiple trapping model used to describe the electron transport in DSSCs is correct.

The general problem encountered is the difference in the interpretation of the electron diffusion length by different research groups. Some groups reported that $L_n$ derived from the IMPS and IMVS compared to the electron diffusion length calculated from

other techniques like the ratio of IPCE for electrolyte and substrate side illumination are different [19, 63, 64]. But in agreement with our results Leng *et al.* [65] and Jennings *et al.* [66] demonstrated that if the same assumptions and conditions are taken into consideration during measurements on the different techniques, the results of the electron diffusion length $L_n$ are similar. This results shows that the assumption of the multiple trapping model is correct and hence $L_n$ is almost equal to $L_0$.

As there are differences between the reported results in the literature, there is a need for further work to be done on understanding the meaning of $L_n$, both experimentally and theoretically. More theoretical models need to be established to study electron transport and estimate the electron diffusion length based on the other experimental techniques which are used. This will lead to a better comparison between different techniques using both theoretical simulations and experimental results. In general there is still a need to study and understand the electron transport in terms of the electron diffusion length and hence to understand both the free and effective diffusion coefficient and lifetime respectively.

## 5.3 Study of photo-generated charge carrier density in DSSCs by microwave reflectance

For the experimental conductivity range considered in this work, our main conclusion was of the linear relationship between the photomodulated reflectivity and the conductivity. Our results shows that for the structure without a short the photomodulated reflectivity is lower compared to that with a short and hence that better experimental sensitivity is obtained.

The linear relation between the conductivity and the photomodulated reflectivity does not explain the non-ideality of the experimental results relating the light intensity ($I_0$) and the conductivity. This raised the question of whether the results are affected by the trapped electrons at high intensity or the changes in mobility. Since the modelling assumes that the reflection is due to the conductivity only, there is a need to take into consideration the effects of dielectric changes on the reflection.

More work needs to be done both experimentally and theoretically to establish if a non-ideality in the relation between light intensity and conductivity in DSSCs really exists and in order to establish the physical origin of this non-ideality. In general the electron transport process in DSSCs still needs more attention and more systematic studies need to be done.

# References


[1] Wenham S.R., Grean M.A., Watt M.E., and Corkish R. *Applied Photovoltaics*. TJ International,Cornwall, UK, 2007.

[2] Sze S.M. *Physics of Semiconductor Devices, Second Edition*. John Wiley and Sons, New York, 1981.

[3] Treble F.C. and Sayigh A.A.M. *Generating Electricity from the Sun*. Pergamon Press, Oxford, 1991.

[4] West K. Solar cells beyond silicon. In *Proceedings of Riso National Energy Conference, Denmark*, May 2003.

[5] Nazeerddin M.K., Splivallo R., Liska P., Comte P., and Grätzel M. Swift dye uptake procedure for dye sensitized solar cell. *Chemical Communications*, 2003:1456–1457.

[6] Tesfamichael T., Will G., Bell J., Prince K., and Dytlewski N. Characterization of a commercial dye-sensitised titania solar cell electrode. *Solar Energy Materials and Solar Cells*, 76(1):25–35, 2003.

[7] O'Regan B. and Grätzel M. A low-cost high efficiency solar cell based on dye-sensitized colloidal $TiO_2$ films. *Nature*, 353(737), 1991.

[8] Bignozzi C.A, Argazzi R., and Kleverlaan C.J. Molecular and supramolecular sensitization of nanocrystalline wide band-gap semiconductors with mononuclear and polynucleur metal complexes. *Chemical Society Reviews*, 29:89–96, 2000.

[9] Nelson J. *The Physics of Solar Cells*. Imperial College Press, London, 2003.

[10] Wurfel P. *Physics of Solar Cells,From basic principles to Advanced Concepts, Second, updated and Expanded Edition*. WILEY-VCH, Weinheim, Germany, 2009.

[11] Tsoutos T., Frantzeskaki N., and Gekas V. Environmental impacts from solar energy technologies. *Energy Policy*, 33:289–296, 2005.

[12] Abdel-Dayem A.M. and Mohamad M.A. Pontential of solar energy utlilization in the textile industry- a case study. *Renewable Energy.*, 23:685–694, 2001.

[13] Gunes S., Neugebauer H., and Sariciftci N.S. Conjugated polymer-based organic solar cells. *Chemical Reviews*, 107(4):1324–1338, 2007.

[14] Gregg B.A. Excitonic solar cells. *The Journal of Physical Chemistry B*, 107:4688–4698, 2003.

[15] Walker A.B., Peter L.M., Martinez D., and Lobato K. Transient photocurrents in dye-sensitized nanocrystalline solar cells. *CHIMIA International Journal for Chemistry*, 61(12):792–795, 2007.

[16] Ogomi Y., Sakaguchi S., Kado T., Kono M., Yamaguchi Y., and Hayase S. Ru dye uptake under pressurized $CO_2$ improvement of photovoltaic performances for dye-sensitized solar cells. *Journal of The Electrochemical Society.*, 153(12), 2006.

[17] Buxton H.G.A. and N. Clarke N. Computer simulation of polymer solar cells. *Modelling. Simul.Mater.Sci.Eng.*, 15:13–26, 2007.

[18] J. Williams and A.B. Walker. Two-dimensional simulations of bulk heterojunction solar cell characteristics. *Nanotechnology*, 19:424011, 2008.

[19] Halme J., Miettunen K., and Lund P. Effect of nonuniform generation and inefficient collection of electrons on the dynamic photocurrent and photovoltage response of nanostructured photoelectrodes. *Journal of Physical Chemistry C*, 112:20491–20504, 2008.

[20] Fillinger A. and Parkinson B.A. The adsorption behavior of a ruthenium-based sensitizing dye to nanocrystalline $TiO_2$. coverage effects on the external and internal sensitization quantum yields. *Journal of the Electrochemical Society.*, 146(12):4559–4564, 1999.

[21] Halme J., Vahermaa P., Miettunen K, and Lund P. Device physics of dye solar cells. *Advanced Materials*, 22:E210–E234, 2010.

[22] Yanagida M., Yamaguchi T., Kurashige M., Hara K., Katoh R., Sugihara H., and Arakawa H. Panchromatic sensitization of nanocrystalline $TiO_2$ with cis-bis (4-carboxy-2-[2-(4-carboxypyridyl)] quinoline) bis (thiocyanato-N) ruthenium (II). *Inorganic. Chemistry*, 42(24):7921–7931, 2003.

[23] Wang P., Zakeerudding S.M., Moser J.E., and Grätzel M. A new ionic liquid electrolyte enhances the conversion efficiency of dye-sensitized solar cells. *The Journal of Physical Chemistry B*, 107:13280–13285, 2003.

[24] Kong F., Dai S., and Wang K. Review of recent progress in dye-sensitized solar cells. *Advances in optoElectronics*, pages 1–8, 2007.

[25] Wang P., Zakeerudding S.M., Moser J.E., Zakeerudding M.K., Sekiguchi T., and Grätzel M. A stable quasi-solid-state dye-sensitized solar cell with an amphiphilic ruthenium sensitizer and polymer gel electrolyte. *Nature Materials*, (6):402–407, 2003.

[26] Wang P., Klein C., Moser J.E, Baker R.H, Cevey-Ha N., Charvet R., Comte P., Zakeerudding S.M., and Grätzel M. Amphiphilic ruthenium sensitizer with 4,4'-diphosphonic acid-2,2'-bipyridine as achoring ligand for nanocrystalline dye sensitized solar cells. *The Journal of Physical Chemistry*, 108:17553–17559, 2004.

[27] Longo C. and De Paoli M-.A. Dye sensitized solar cell: A successful combination of material. *Journal of Brazilian Chemical Society*, 14(6):889–901, 2003.

[28] Lenzmann F.O. and Kroon J.M. Recent advances in dye-sensitised solar cells. *Advances in optoElectronics*, 2007.

[29] Jennings J.R., Ghicov A., Peter L.M., Schmuki P, and Walker A.B. Dye-sensitized solar cells based on oriented $TiO_2$ nanotube arrays: Transport, trapping, and transfer of electrons. *Journal of the American Chemical Society.*, 130:13364–13372, 2008.

[30] Paulose M., Shankar K., Varghese O.K., Mor G.K., Hardin B., and Grimes C.A. Backside illuminated dye-sensitized solar cells based on titania nanotube array electrodes. *Nanotechnology.*, 17(5):1446–1448, 2006.

[31] Mor G.K., Shankar K., Paulose M., Varghese O.K., and Grimes C.A. Use of highly-ordered $TiO_2$ nanotube arrays in dye-sensitized solar cells. *Nano Letters.*, 6(2):215–218, 2006.

[32] Kim D., Ghicov A., Albu S.P., and Schmuki P. Bamboo-type $TiO_2$ nanotubes: Improved conversion efficiency in dye-sensitized solar cells. *Journal of the American Chemical Society.*, 130(49):16454–16455, 2008.

[33] Zhu K., Neale N.R., Miedaner A., and Frank A.J. Enhanced charge-collection efficiencies and light scattering in dye-sensitized solar cells using oriented $TiO_2$ nanotubes arrays. *Nano Letters.*, 7(1):69–74, 2006.

[34] Mor G.K., Varghese O.K., Paulose M., Shankar K., and Grimes C.A. A review on highly ordered, vertically oriented $TiO_2$ nanotube arrays: Fabrication, material properties, and solar energy applications. *Solar Energy Materials and Solar Cells*, 90(14):2011 – 2075, 2006.

[35] El-Shishtawy R.M. Functional dyes, and some Hi-Tech applications. *International Journal of Photoenergy*, pages 1–21, 2009.

[36] Tesfamichael T., Will G., Bell J., Prince K., and Dytlewski N. Characterization of a commercial dye-sensitised titania solar cell electrode. *Solar Energy Materials and Solar Cells*, 76(1):25–35, 2003.

[37] Katoh R., Yaguchi K., Murai M., Watanabe S., and Furube A. Differences in adsorption behavior of N3 dye on flat and nanoporous $TiO_2$ surfaces. *Chemical Physics Letters*, 497(1-3):48 – 51, 2010.

[38] Chou T.P., Zhang Q., and Cao G. Effects of dye loading conditions on the energy conversion efficiency of ZnO and $TiO_2$ dye-sensitized solar cells. *Journal of Physical Chemistry C*, 111(50):18804–18811, 2007.

[39] Ghicov A., Albu S.P., Hahn R., Kim D., Stergiopoulos T., Kunze J., Schiller C.A., Falaras P., and Schmuki P. $TiO_2$ nanotubes in dye-sensitized solar cells: Critical factors for the conversion efficiency. *Chemistry-An Asian Journal*, 4(4):520–525, 2009.

[40] Hashimoto K., Irie H., and Fujishima A. $TiO_2$ photocatalysis: A historical overview and future prospects. *Japanese Journal of Applied Physics*, 44(12), 2005.

[41] Paulose M., Prakasam H.E., Varghese O.K., Peng L., Popat K.C., Mor G.K., Desai T.A., and Grimes C.A. $TiO_2$ nanotube arrays of 1000 $\mu$m length by anodization of titanium foil: Phenol red diffusion. *Journal of Physical Chemistry.C*, 111(41):14992–14997, 2007.

[42] Rustomji C.S., Frandsen C.J., Jin S., and Tauber M.J. Dye-sensitized solar cell constructed with titanium mesh and 3-D array of $TiO_2$ nanotubes. *The Journal of Physical Chemistry B*, page 16835, 2010.

[43] Grätzel M. Solar energy conversion by dye-sensitized photovoltaic cells. *Inorganic Chemistry.*, 44:6841–6851, 2005.

[44] Gonzalez-Valls I. and Lira-Cantu M. Dye sensitized solar cells based on vertically-aligned Zno nanorods: effect of UV light on power conversion efficiency and lifetime. *Energy and Environmental Science*, 3(6):789–795, 2010.

[45] Senevirathna M.K.I., Pitigala P., Premalal E.V.A., Tennakone K., Kumara G.R.A, and Konno A. Stability of the $SnO_2$/MgO dye-sensitized photoelectrochemical solar cell. *Solar Energy Materials and Solar Cells*, 91(6):544–547, 2007.

[46] Guo P. and Aegerter M.A. RU(II) sensitized $Nb_2O_5$ solar cell made by the sol-gel process. *Thin Solid Films*, 351(1-2):290 – 294, 1999.

[47] Peter L.M. Sticky electrons transport and interfacial transfer of electrons in the dye-sensitized solar cell. *Accounts of Chemical Research.*, 42(11):1839–1847, 2009.

[48] Kankare J. and Vinokurov I.A. Kinetics of langmuirian adsorption onto planar, spherical, and cylindrical surfaces. *Langmuir*, 15(17):5591–5599, 1999.

[49] Lionello A., Josserand J., Jensen H., and Girault H.H. Protein adsorption in static microsystems: effect of the surface to volume ratio. *Lab on a Chip*, 5(3):254–260, 2005.

[50] Comsol Multiphysics. *Comsol RF Module, Model Library and User Guide, Version 3.3.*

[51] Bhugun I. and Anson F.C. A generalized treatment of the dynamics of the adsorption of langmuirian systems at stationary or rotating disk electrodes. *Journal of Electroanalytical Chemistry.*, 439(1):1 – 6, 1997.

[52] Kuang D., Brillet J., Chen P., Takata M., Uchida S., Miura H., Sumioka K., Zakeeruddin S.M., and Grätzel M. Application of highly ordered $TiO_2$ nanotube arrays in flexible dye-sensitized solar cells. *ACS Nano*, 2(6):1113–1116, 2008.

[53] McKee S. and Swailes D. On the derivation of the langmuir isotherm for adsorption kinetics. *Journal of Physics A: Mathematical and General.*, 24:L207–L209, 1991.

[54] Peter L.M. Department of Chemistry, University of Bath, Private communication with the author.

[55] Holliman P.J., Velasco B.V, Butler I., Wijdekop M., and Worsley D.A. Studies of dye sensitisation kinetics and sorption isotherms of Direct Red 23 on titania. *International. Journal of Photoenergy.*, 2008, 2008.

[56] Kambili A., Walker A.B., Qiua F.L., Fisher A.C., Savin A.D., and Peter L.M. Electron transport in the dye sensitized nanocrystalline cell. *Physica E*, 14:203 209, 2002.

[57] Peter L. M. and Wijayantha K. G. U. Electron transport and back reaction in dye sensitised nanocrystalline photovoltaic cells. *Electrochimica Acta*, 452:4543–4551, 2000.

[58] Peter L. M. Characterization and modeling of dye-sensitized solar cells. *Journal of Physical Chemistry C*, 111:6601– 6612, 2007.

[59] Fisher A. C., Peter L. M., Ponomarev E. A., Walker A. B., and Wijayantha K. G. U. Intensity dependence of the back reaction and transport of electrons in dye-sensitized nanocrystalline $TiO_2$ solar cells. *Journal of Physical Chemistry B*, 104:949–958, 2000.

[60] Dloczik L., Ileperuma O., Lauermann I., Peter L. M., Ponomarev E. A., Redmond G., Shaw N. J., and Uhlendorf I. Dynamic response of dye-sensitized nanocrystalline solar cells: Characterization by intensity-modulated photocurrent spectroscopy. *Journal of Physical Chemistry B*, 101:10281 10289, 1997.

[61] Jennings J. R. and Peter L. M. A reappraisal of the electron diffusion length in solid-state dye-sensitized solar cells. *Journal of Physical Chemistry C*, 111:16100–16104, 2007.

[62] Peter L.M. Transport, trapping and interfacial transfer of electrons in dye-sensitized nanocrystalline solar cells. *Journal of Electroanalytical Chemistry.*, 599:233–240, 2006.

[63] Barnes P.R. F., Anderson A.Y., Koops S.E., Durrant J.R., and O'Regan B.C. Electron injection efficiency and diffusion length in dye-sensitized solar cells derived from incident photon conversion efficiency measurements. *Journal of Physical Chemistry C*, 113:1126–1136, 2008.

[64] Villanueva-Cab J., Wang H., Oskam G., and Peter L.M. Electron diffusion and back reaction in dye-sensitized solar cells: The effect of nonlinear recombination kinetics. *The Journal of Physical Chemistry Letters*, 1(4):748–751, 2010.

[65] Leng WH, Barnes P.R.F., Juozapavicius M., ORegan B.C., and Durrant J.R. Electron diffusion length in mesoporous nanocrystalline $TiO_2$ photoelectrodes during water oxidation. *The Journal of Physical Chemistry Letters*, 1(6):967–972, 2010.

[66] Jennings J.R., Li F., and Wang Q. Reliable determination of electron diffusion length and charge separation efficiency in dye-sensitized solar cells. *Journal of Physical Chemistry C*, 114(34):737–740, 2010.

[67] Franco G., Gehring J., Peter L. M., Ponomarev E. A., and Uhlendorf I. Frequency-resolved optical detection of photoinjected electrons in dye-sensitized nanocrystalline photovoltaic cells. *Journal of Physical Chemistry B*, 103:5100–5107, 1999.

[68] Wang H. and Peter L.M. A comparison of different methods to determine the electron diffusion length in dye-sensitized solar cells. *Journal of Physical Chemistry C*, 113(42):18125–18133, 2009.

[69] Duffy N. W., Peter L. M., and Wijayantha K. G. U. Characterisation of electron transport and back reaction in dye-sensitised nanocrystalline solar cells by small amplitude laser pulse excitation. *Electrochemistry Communications*, 2(4):262 – 266, 2000.

[70] Gómez R. and Salvador P. Photovoltage dependence on film thickness and type of illumination in nanoporous thin film electrodes according to a simple diffusion model. *Solar Energy Materials and Solar Cells*, 88(4):377 – 388, 2005.

[71] Ni M., Leung M.K.H., and Leung D.Y.C. Theoretical modelling of the electrode thickness effect on maximum power point of dye-sensitized solar cell. *The Canadian Journal of Chemical Engineering*, 86(1):35–42, 2008.

[72] Soedergren S., Hagfeldt A., Olsson J., and Lindquist S.E. Theoretical models for the action spectrum and the current-voltage characteristics of microporous semiconductor films in photoelectrochemical cells. *Journal of Physical Chemistry*, 98(221):5552–5556, 1994.

[73] Walker A.B., Peter L. M., Lobato K., and Cameron P.J. Analysis of photovoltage decay transients in dye-sensitized solar cells. *Journal of Physical Chemistry B*, 110(50):25504–25507, 2006.

[74] Nguyen T. T. O., Peter L.M., and Wang H. Characterization of electron trapping in dye-sensitized solar cells by near-IR transmittance measurements. *Journal of Physical Chemistry C*, 113:68532–8536, 2009.

[75] Peter L.M. Dye-sensitized nanocrystalline solar cells. *Physical chemistry chemical physics*, 9(21):2630–2642, 2007.

[76] Bailes M., Cameron P. J., Lobato K., and Peter L. M. Determination of the density and energetic distribution of electron traps in dye-sensitized nanocrystalline solar cells. *Journal of Physical Chemistry B*, 109(32):15429–15435, 2005.

[77] Oekermann T., Yoshida T., Minoura H., Wijayantha K. G. U., and Peter L. M. Electron transport and back reaction in electrochemically self-assembled nanoporous ZnO/dye hybrid films. *Journal of Physical Chemistry B*, 108(24):8364–8370, 2004.

[78] Bisquert J. and Vikhrenko V.S. Interpretation of the time constants measured by kinetic techniques in nanostructured semiconductor electrodes and dye-sensitized solar cells. *Journal of Physical Chemistry B*, 108:23132322, 2004.

[79] Dunn H.K. and Peter L.M. How efficient is electron collection in dye-sensitized solar cells? comparison of different dynamic methods for the determination of the electron diffusion length. *Journal of Physical Chemistry C*, 113:47264731, 2009.

[80] Peter L. M. and Wijayantha K. G. U. Intensity dependence of the electron diffusion length in dye-sensitised nanocrystalline $TiO_2$ photovoltaic cells. *Electrochemistry Communications.*, 1(12):576 – 580, 1999.

[81] Kruger J., Plass R., Grätzel M., Cameron P.J., and Peter L.M. Charge transport and back reaction in solid-state dye-sensitized solar cells: A study using intensity-modulated photovoltage and photocurrent spectroscopy. *Journal of Physical Chemistry B*, 107(31):7536–7539, 2003.

[82] Ponomarev E. A. and Peter L. M. A generalized theory of intensity modulated photocurrent spectroscopy (imps). *Journal of Electroanalytical Chemistry.*, 396(1-2):219 – 226, 1995.

[83] Fabregat-Santiago F., Bisquert J., Palomares E., Haque S.A., and Durrant J.R. Impedance spectroscopy study of dye-sensitized solar cells with undoped spiro-OMeTAD as hole conductor. *Journal of Applied Physics*, 100:034510, 2006.

[84] Duffy N. W., Peter L. M., Rajapakse R. M. G., and Wijayantha K. G. U. A novel charge extraction method for the study of electron transport and interfacial transfer in dye sensitised nanocrystalline solar cells. *Electrochemistry Communications*, 2(9):658 – 662, 2000.

[85] Walker A.B. Department of Physics, University of Bath. Private communication with the author.

[86] Hara K., Horiguchi T., Kinoshita T., Sayama K., Sugihara H., and Arakawa H. Highly efficient photon-to-electron conversion with mercurochrome-sensitized nanoporous oxide semiconductor solar cells. *Solar Energy Materials and Solar Cells*, 64(2):115 – 134, 2000.

[87] Ito S., Zakeeruddin S.M., Comte P., Liska P., Kuang D., and Grätzel M. Bifacial dye-sensitized solar cells based on an ionic liquid electrolyte. *Nature photonics*, 2(11):693–698, 2008.

[88] Wei M., Konishi Y., Zhou H., Yanagida M., Sugihara H., and Arakawab H. Highly efficient dye-sensitized solar cells composed of mesoporous titanium dioxide. *Journal of Materials Chemistry*, 16(11):1287–1293, 2006.

[89] Kang M.G., Ryu K.S., Chang S.H., Park N.G., Hong J.S., and Kim K.J. Dependence of $TiO_2$ film thickness on photocurrent-voltage characteristics of dye-sensitized solar cells. *Notes*, 25(5):743, 2004.

[90] Nakade S., Kubo W., Saito Y., Kanzaki T., Kitamura T., Wada Y., and Yanagida S. Influence of measurement conditions on electron diffusion in nanoporous $TiO_2$ films: Effects of bias light and dye adsorption. *Journal of Physical Chemistry B*, 107(51):14244–14248, 2003.

[91] Park N.G., Van de Lagemaat J., and Frank AJ. Comparison of dye-sensitized rutile-and anatase-based $TiO_2$ solar cells. *Journal of Physical Chemistry B*, 104(38):8989–8994, 2000.

[92] Kunst M. and G. Beck. The study of charge carrier kinetics in semiconductors by microwave conductivity measurements. *Journal of Applied Physics.*, 60(3558), 1986.

[93] Swiatkowski C., Sanders A., Buhre K.D., and Kunst M. Charge-carrier kinetics in semiconductors by microwave conductivity measurements. *Journal of Applied Physics*, 78(3), 1995.

[94] Schofthaler M. and Brendel R. Sensitivity and transient response of microwave reflection measurements. *Journal of Applied Physics.*, 77, 1995.

[95] Subramanian V. and Sobhanadri J. Study of microwave transient photo conductivity on single and polysilicon using cavity perturbation technique. *Japanese Journal of Applied Physics*, 35(Part 1, No. 5A):2839–2844, 1996.

[96] Kunst M., Wunsch F., and Jokisch D. Lateral scanning of Si based systems by measurements of the microwave photoconductance. *Materials Science and Engineering B*, 102(1-3):173 – 178, 2003.

[97] Citarella G., von Aichberger S., and Kunst M. Microwave photoconductivity techniques for the characterization of semiconductors. *Materials Science and Engineering B*, 91-92:224 – 228, 2002.

[98] Duzhko V., Koch F., and Dittrich T. Transient photovoltage and dielectric relaxation time in porous silicon. *Journal of Applied Physics*, 91:9432, 2002.

[99] Eikelboom J. A., Leguijt C., Frumau C. F. A., and Burgers A. R. Microwave detection of minority carriers in solar cell silicon wafers. *Solar Energy Materials and Solar Cells*, 36(2), 1995.

[100] Chen F.X., Cui R.Q., and Xu L. A theoretical analysis of sensitivity in semiconductor measurement by microwave photoconductance decay. *Materials Science and Engineering B*, 116(2):161 – 167, 2005.

[101] Schieck R. and Kunst M. Frequency modulated microwave photoconductivity measurements for characterization of silicon wafers. *Solid-State Electronics*, 41(11):1755 – 1760, 1997.

[102] Kunst M. and Beck G. The study of charge carrier kinetics in semiconductors by microwave conductivity measurements. ii. *Journal of Applied Physics*, 63:1093, 1988.

[103] Lubberhuizen W.H., Vanmaekelbergh D., and Van Faassen E. Recombination of photogenerated charge carriers in nanoporous gallium phosphide. *Journal of Porous Materials*, 7(1):147–152, 2000.

[104] Konstantinova E.A., Timoshenko V.Y., Kashkarov P.K., Kytin V.G., Gaivoronskii V.Y., Porteanu H., Dittrich T., and Koch F. Microwave photoconductivity in nanocrystalline porous titanium oxide subjected to pulsed laser excitation. *Semiconductors*, 36(3):319–324, 2002.

[105] Germeau A.E.A., Faassen E.E.H., and van Vanmaekelbergh D.A.M. Contactless measurement of short-range electron motion in semiconducting macroporous GaP. *Physical review. B, condensed matter*, 65:165331–1 – 165331–7, 2002.

[106] Porteanu H.E., Timoshenko V.Y., Dittrich T., and Koch F. Microwave conductivity and raman spectroscopy of porous $TiO_2$. *physica status solidi (a)*, 182(1):201–206, 2000.

[107] Duzhko V., Timoshenko V.Y., Koch F., and Dittrich T. Photovoltage in nanocrystalline porous $TiO_2$. *Physical Review B*, 64(7):75204–1 – 75204–7, 2001.

[108] Dunn H. *Probing the free electron density and diffusion length in dye-sensitized solar cells.* PhD thesis published at the University of Bath, 2009.

[109] Wang H.F., Chen L.Y., Su W.N., Chung J.C., and Hwang B.J. Effect of the compact $TiO_2$ layer on charge transfer between N3 dyes and $TiO_2$ investigated by raman spectroscopy. *The Journal of Physical Chemistry C*, 114(7):3185–3189, 2010.

[110] Mooijwear H. *Microwave Techniques.* The Macmillan Press LTD, 1971.

[111] Dobbs R.J. *Electromagnetic waves.* Routledge and Kegan Paul plc, 1985.

[112] Feynman R.P., Leighton R.B., and Sands M. *The Feynman Lectures on Physics of Solar Cells*, volume III. Calfornia Institute of Technology, 1964.

[113] Pozar.D.M. *Microwave Engineering.* John Wiley and Sons, INC., 1998.

[114] Osepchuk J.M. Sources and basic characteristics of microwave/RF radiation. *Bulletin of the New York Academy of Medicine*, 55(11):976, 1979.

[115] Graf M., Ruchle E., Urban H., Kaiser M., Alberts L., Emmerich R., and Elsner P. Numerical simulation of microwave field distribution for bifocal plasma sources. *Surface and Coatings Technology*, 200(1-4):904 – 908, 2005.

[116] Ratanadecho P., Aoki K., and Akahori M. A numerical and experimental investigation of the modelling of microwave melting of frozen packed beds using a rectangular wave guide. *International Communications in Heat and Mass Transfer*, 28(6):751 – 762, 2001.

[117] Williams J.H.T. *Finite Element simulation of Dye sensitized and Polymer Solar cells.* PhD thesis published at the University of Bath, 2008.

[118] Spada E.J., Rao V.R, Bhat I., and Borregot J.M. Non-destructive characterization of HgCdTe using photoinduced microwave reflection. *Semiconductor Science and Technology*, 8:936–940, 1993.

[119] Nestle N. and Kimmich R. Concentration-dependent diffusion coefficients and sorption isotherms. application to ion exchange processes as an example. *Journal of Physical Chemistry.*, 100(30):12569–12573, 1996.

[120] Wei D. Dye sensitized solar cells. *International Journal of Molecular Sciences*, 11(3):1103–1113, 2010.

[121] Reinmuth W. H. Diffusion to a plane with langmuirian adsorption. *Journal of Physical Chemistry.*, 65(3):473–476, 2002.

[122] G. Franco, L. M. Peter, and E. A. Ponomarev. Detection of inhomogeneous dye distribution in dye sensitised nanocrystalline solar cells by intensity modulated photocurrent spectroscopy (imps). *Electrochemistry Communications*, 1(2):61 – 64, 1999.

# Appendix A

# Calculation employing COMSOL Multiphysics

## A.1 Introduction

Comsol Multiphysics is a commercially available software and a powerful interactive environment for modeling and solving all kinds of scientific and engineering problems based on partial differential equations (PDE's). With this software one can easily extend conventional models for one type of physics into multiphysics models that solve coupled physics phenomena and do so simultaneously. When solving the PDE's, Comsol Multiphysics uses the finite element method (FEM). The software runs the finite element analysis together with adaptive meshing and error control using a variety of numerical solvers. It is possible to build models by defining the relevant physical quantities such as material properties, loads, constraints, sources, and fluxes rather than by defining the underlying equations. One can always apply these variables, expressions, or numbers directly to solid domains, boundaries, edges and points independently of the computational mesh. A simplified version of the manual of Finite Element Method has been developed by Jonny Williams in our group (Device modelling group, University of Bath) [117]. Currently, our modelling group has access to two Comsol Multiphysics modules:

1. Comsol Multiphysics (General comsol module) and
2. Radio frequency (RF) Module.

For creating a new model, the software allows us to choose the dimension of the problem, which can be 1,2 and 3. Depending on the dimension of the model you want to follow, the first step is to choose the related Comsol package to the problem. In this work two different models were considered with different application, a 2D Axial symmetry model simulation was considered in the chapter of the dye uptake in DSSCs and in the chapter of the study of photo-generated charge carriers density in DSSCs by microwave reflectance a 3D RF module simulation was considered.

COMSOL Multiphysics support two ways of specifying the mathematical model for expressing our physical phenomena:

1. A free-form entry of custom partial differential equations, or
2. Use a specialized physics application mode.

## A.2 Implementation of dye uptake in DSSCs model

The problem of dye uptake in $TiO_2$ nanotube film is based on the Langmuir isotherm, where the concentration of dye diffuses into the film as adsorption and desorption of dye takes place on the surface and we assume that a monolayer of dye molecules is formed. The model can be simulated as a 3D cylindrical geometry. But due to axial symmetry in Comsol, it is easy to model the 3D geometry in 2D axial symmetry. One of the reasons for this is to limit the computing time, as it easier to run a 2D rather than 3D model. The other reason is that as the boundary conditions of the two ends (sides) of the nanotubes (cylinder) are the same, we can only look at half view of the cylinder. The model can now be set as a 2D axial symmetry slab as followed in this work.

Now we consider the implementation of the dye uptake in 2D axial symmetry diffusion equation. The 2D-axial means we have our cylindrical symmetry cases along a (work) plane of dimension by default r (radial or horizontal) and z (height parallel to the axis). When we define our cut view of the object, we work only in the positive r (or $r \geq 0$) quadrants (z might be negative or positive) [50].

Many models have been done following the same procedure of modeling the 3D geometry as a 2D axial symmetry geometry provided the boundary condition of the two other sides are the same, one example is on Comsol model library of the version 3.5a as *Terminal falling velocity of a sand grain* [50].

The first thing to consider when using Comsol Multiphysics is to understanding the problem and then choose the module you need to use. The next step will be to draw the geometry needed for the problem and implement the boundary conditions. As discussed above in this work we use a 2D Axial Symmetry together with the transient diffusion analysis. This was done because we are varying the time as the adsorption and desorption of the dye molecules takes place during the diffusion processes. After drawing the geometry we need to set the boundary conditions and specify the correct dimensions of the structure. For our nanotube we have to set the radius and the length as 10nm and 20$\mu$m respectively. However our size of the nanotube is in order of nanometer for the radius and micrometer for the thickness (length) of the nanotube, so we need to set this, so that it will be easier to view the geometry.

### A.2.1 Boundary conditions

We now consider the implementation of the subdomain diffusion coefficient and boundary conditions of the model. In this case we only have one subdomain, so we set the diffusion (D) value on the subdomain and the next step will be to set the boundary conditions. The initial boundary condition used in this model was,

$$C_{dint} = c_d \times \left(\frac{1 - r^2}{R_0^2}\right) \times (z > d - w) \tag{A.1}$$

where $C_{dint}$ is the initial concentration, $c_d$ is the initial dye concentration, $R_0$ is the radius of the nanotube, $r$ is the distance from the center of the nanotube, $z$ is the distance along the pore from the first end of the pore, $d$ is the length of the $TiO_2$ nanotube and $w$ is the width of the pore over which have a non-zero concentration ($w = 0.01d$). The above equation A.1 was used as the initial condition in this work where we assume that at the beginning of the simulation the pore is empty except at distance $d - w$. It was also compared to the zero initial condition and the results were the same. The advantage of using the initial boundary conditions defined by equation A.1, was that we know what the initial condition will look like.

At the surface of the $TiO_2$ nanotube we expect the adsorption and desorption process to take place and the dye molecules to stick or to be adsorbed, so we need to set these boundary conditions at the surface of the $TiO_2$ nanotube which is given by equation A.2. As our nanotube view is given by a 2D axial symmetry as a rectangle, we have 4 sides which we have to consider for the boundary conditions. We set each boundary segment from 1-4, where 1 is set as an axial symmetry, 2 as initial bulk concentration ($c_d$), 3 as flux zero boundary condition and 4 adsorption-desorption boundary condition as shown in figure 2.3 bottom panel on page 22.

At boundary (2), the initial dye concentration $c_d$ does not change throughout the simulations and at boundary (3) a zero flux boundary condition, illustrate that there will be no diffusion of dye concentration after this point. As we are working with a 2D axial symmetry, the boundary condition on one side of the surface is the axial symmetry (1) boundary condition and on the other side we have the Langmuir boundary (4) condition given by,

$$-J(z,t) = \frac{\partial \Gamma(z,t)}{\partial t} = k_{ads} l_{mol} c(r,z,t) \left(1 - \frac{\Gamma(z,t)}{\Gamma_{max}}\right) - k_{des}\Gamma(z,t) \tag{A.2}$$

where $J(z,t)$ is the flux of dye moving towards the pore surface, $\Gamma(z,t)$ is the surface pore coverage of dye molecules at time t, $\Gamma_{max}$ is the initial maximum pore surface coverage, $k_{ads}$ is the adsorption coefficient, $k_{des}$ is the desorption coefficient.

The cross-section area of the pore can be calculated as

$$A_{pore} = 2\pi R_0 d \tag{A.3}$$

and the volume of the pore

$$V_{pore} = \pi R_0^2 d \tag{A.4}$$

where $R_0$ is the radius of the nanotube and $d$ is the length of the nanotube.

At a longer time the total number of dye molecules is constant given by,

$$N = N_{sol} + N_{surf} \tag{A.5}$$

where

$$N_{sol}(t) = 2\pi \int_0^d dz \int_0^{R_0} c(r,z,t) r dr \tag{A.6}$$

and

$$N_{surf} = 2\pi R_0 \Gamma_{max} \int_0^d \theta(z,t) dz \tag{A.7}$$

### A.2.2 Meshing

Meshing is dividing the geometry of the system into small elements. The finite element methods approximates the solution within each element, using some elementary shape function that can be constant, linear or higher order. Depending on the element order in the model, a finer or coarser mesh is required to resolve the solution. There are many ways of meshing in Comsol like,

1. Meshing the geometry directly (automatic mesh) or
2. Meshing using each subdomain on the geometry, this method is used to control the number of elements in certain parts of the geometry, like boundaries and interfaces.

In this work we have only one subdomain and it was easier to follow the automatic mesh, while meshing the whole geometry. In many cases we need a finer mesh near the boundary and so we need to mesh the edge accordingly to achieve a uniform mesh. In this work a finer automatic mesh was used, where mesh was refined two times.

The last step is to run the model and as discussed under the boundary conditions we have to get the initial value first to make sure that there are no other numerical results before the start of the simulations. There are two solver parameters, which can be used in Comsol, we can use solve the problem using the initial solution or using the last solution in the model. For the case of this work, we have only solve the model after getting the initial value, to make sure that at the beginning of the simulation there is no other solution involved.

### A.2.3 Concentration dependent diffusion coefficient

The model discussed above, as implemented in Comsol assume that the diffusion coefficient (D) obeys Fick's law [121]. The simulation results of this model show good agreement with experimental results at lower concentration and at higher concentration there is a discrepancy between the predicted and experimental data discussed in chapter 2. To understand the Comsol based model a step further was taken by looking at diffusion coefficient which vary with the concentration. The reason for the effective diffusion coefficient is based on the argument that during the dye uptake process, the surroundings and the coverage on the surface changes, and this makes the diffusion coefficient to vary with the change of the concentration inside the $TiO_2$ film. The main

problem with this model is that it only uses few boundary condition as it looks only at the diffusion of the concentration, without taking into account the adsorption and desorption of the dye molecules on the surface of the film.

As a way of validating and understanding the Comsol model based results, a 1D diffusion model was developed by Dan Staff in our group, based on the reported concentration dependent diffusion coefficient by Nestle and Kimmich [119]. The difference between the current model (the Comsol model followed in this work) and the concentration diffusion coefficient model is that this model uses an effective diffusion coefficient ($D_{eff}$), which varies with the change in the concentration on the film. The model is based on the assumption that the concentration $c_b$ of bound molecules in the sorbent material is proportional to the concentration c of the unbound sorbate in the same material [119],

$$c_b = kc \tag{A.8}$$

where k is a material constant.

In this case, the diffusion of unbound sorbate obeys

$$\frac{\partial c}{\partial t} = D\nabla^2 c - \frac{\partial c_b}{\partial t} = D\nabla^2 c - k\frac{\partial c}{\partial t} \tag{A.9}$$

This modified diffusion equation can be simplified to

$$\frac{\partial c}{\partial t} = \frac{D}{1+k}\nabla^2 c \tag{A.10}$$

Thus the diffusion coefficient has been modified to

$$D_{eff} = \frac{D}{1+k} \tag{A.11}$$

where D is the diffusion coefficient in the absence of any absorption reactions and $D_{eff}$ is the effective diffusion coefficient or the concentration dependent diffusion coefficient.

Figure A.1 illustrate the results of the 1D model. It can be observed from the figure that there is a good agreement between the experimental and modeling results. The results also validate the fact that when the process of diffusion and adsorption is taking place in the $TiO_2$ film, we are changing other parameters involved, like the arrangement of the dye molecules on the surface of the film, movement of the dye molecules, etc.

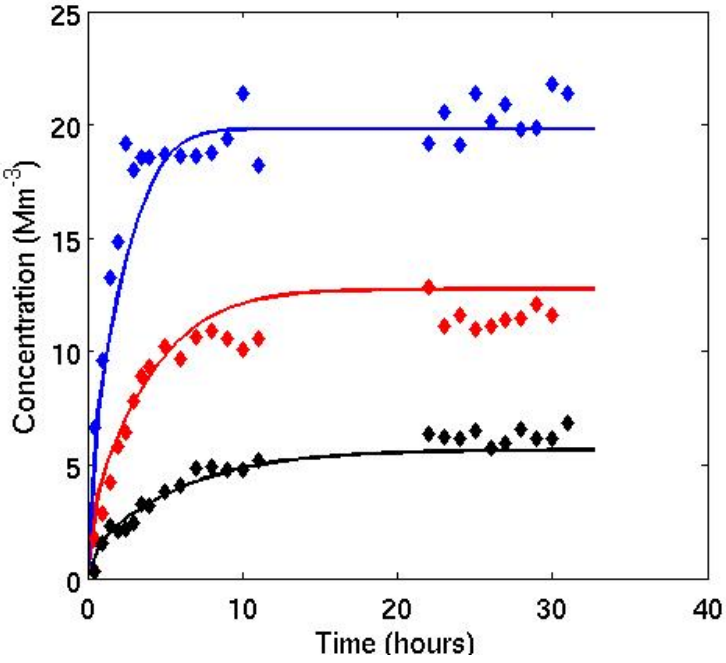


Figure A.1: Comparison between the experimental (diamond) and modelling (solid line) results for dye uptake on a 20 $\mu$m nanotube, for the different dye concentration, i.e, 0.01mM (black), 0.03mM (red) and 0.07mM (blue), The values used for calculation are D = $4 \times 10^{-10}$ $m^2s^{-1}$, $\Gamma_{max} = 8.5 \times 10^{19}$ $m^{-2}$ and $\kappa = 1.65 \times 10^4$.

## A.3 Study of photo-generated charge carrier density in DSSCs by microwave reflectance

### A.3.1 Model implementation

We now consider the implementation of the microwave reflectance simulations in DSSCs. The radio frequency (RF) Module of Comsol Multiphysics was used. The models were built in both 2 dimensions (2D) to 3 dimensions (3D). As described in chapter 4, the current work was started in 1D, then 2D and finally in 3D. In this section most of the discussions will be of the implementation of the 3D model which was finally used. The model setup, together with the boundary conditions and calculations of the reflection coefficient, will be discussed in detail.

The understanding of the problem was that, the experimental measurements can be explained by modelling microwaves emitted from a waveguide and then interacting with a multilayer structure representing a photocell. As the results of the interaction some of the microwave power will be reflected, absorbed and some will escape at the boundaries of the photocell depending on the dielectric constant and conductivity values

of the $TiO_2$ semiconductor. As shown in figure 4.13 the setup was approximated as a T-Junction structure in 3D.

A well defined user friendly Comsol manual has been compiled by Jonny Williams in our group [117]. As discussed above, the understanding was to have a T-Junction structure, where we have a waveguide irradiating a 13 $\mu$m $TiO_2$ semiconductor layer sandwiched between two glass layers of variable thickness and an optional final layer representing a high conductivity short. The main challenge when drawing the different layers is to make sure that there is continuity between them, for example between the waveguide and the first glass layer. As the $TiO_2$ is a very thin layer (microns) between two thick glass layers it is not easy to draw it correctly to maintain the continuity between the layers. More details are discussed in section A.3.2 below. Due to this continuity problem, there was a need to first perform our simulations in 2D. The main aim was to understand the setting up of the problem and also to get idea of the expected results before working in 3D.

For RF module subdomain settings, all we need to specify is the dielectric constant, $\epsilon$,(or relative permittivity), electric conductivity ($\sigma$) and the relative permeability ($\mu_r$). In our case we have two glass layers with the same value of $\epsilon$ and $TiO_2$ with a high $\epsilon$ which act as the active semiconductor layer. This is the only layer where we are changing conductivity and we set the $\mu_r = 1$ as we are considering a nonmagnetic material. The Comsol software also allows us to use the refractive indexes of the material, but in this work we were interested on the change in conductivity on the $TiO_2$ semiconductor layer, so there was no need to use the refractive indexes.

At the surface of the photocell there are several properties of the boundary conditions which we need to consider. The model uses ports to set wave excitation and radiation by the structure. Only one port is considered as a wave excitation port and at this port we need to set the properties of the wave. For example, we need to set the type of wave, transverse electric rectangular wave to a $TE_{10}$ mode.

### A.3.2 Problems encountered with Comsol

It was found that Comsol does not converge to the correct values due to continuity problem in setting up the model. The main problem arises from the fact that there is very large difference between the thicknesses of the layers of the photocell, as we have a $TiO_2$ layer of few micrometers between glass layers of thickness in millimeters. This made it difficult for comsol to create an appropriate mesh. There are two ways to deal with this problem. Changing the mesh parameter or by setting the mesh parameters

manually.

The computing time was also a problem when using 3D simulations. For the simple case of a 2D model there was no problem of the computing time and it was easy to get results for a range of conductivities in few hours using automatic meshing. For the 3D model the computing time was a problem as the computing time was several hours, especially when using automatic meshing. This is an inherent problem of 3D calculations. It appears to be due to inappropriate meshing. A more efficient and flexible meshing algorithm is needed that allows the parameter to be individually set for each domain. During the simulations changing from automatic meshing to coarse meshing improved the computing time.

As discussed on section A.3.1 above, the other problem encountered was the continuity between the photocell layers, as it was very difficult to have a small thickness layer of few micrometers between the two thick glass layers and achieve the continuity boundary conditions. This leads to convergence problems in the model until a better way of setting the layer thickness was achieved by drawing the layers, and setting their dimensions and boundary conditions at the same time rather than drawing the complete geometry and then setting the dimension and boundary conditions. This leads to a better way of maintaining the smooth continuity between the layers and hence solves this convergence problem.

# Appendix B

# Electron Diffusion Length in DSSCs

## B.1 Average quasi Fermi level

The main assumption on this work was based on the fact that if the difference between average short and open circuit quasi Fermi level can be taken into consideration, then $L_0 \approx L_n$. As discussed by Jennings *et al.* [29] the mean or average quasi Fermi level at short circuit can be obtained in three different ways, that is, it can be obtained as an average value of the short circuit quasi Fermi level or by integrating the free and trapped electron concentration and then calculate the value of average short circuit quasi Fermi level. Figure B.1 shows the short circuit $E_{Fn}$ profile calculated from the continuity equation with the mean short circuit $E_{Fn}$ values calculated by averaging the short circuit $E_{Fn}$ and the integrated free electron density. It can be observed from the figure that there is good agreement between the average $E_{Fn}$ calculated by averaging the short circuit $E_{Fn}$ and by integrating the free electron density.

## B.2 Zeta factor

As the numerical factor was used to extract the effective diffusion length, it was also important to validate the value of the numerical factor ($\zeta$) obtained experimentally using the theoretical calculations. Simulations were done using the quasi static assumption to calculate the value of $D_n$ and use its IMPS response to extract the minimum angular frequency. After getting the two values, that is the $D_n$ and the corresponding IMPS

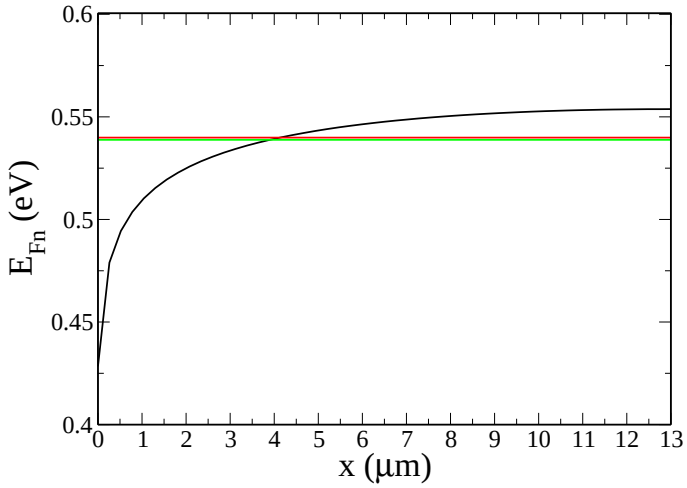


Figure B.1: Short circuit $E_{Fn}$ (black line), average short circuit $E_{Fn}$ (red line) and average short circuit $E_{Fn}$ from $n_c$ (green line) for substrate side illumination. The values used for the calculation are d = 13 $\mu$m, $\alpha = 5.3\times10^4$ m$^{-1}$, $I_0 = 3.08 \times 10^{20}$ m$^{-2}$s$^{-1}$, T = 293K, $T_c = 1090$K, $D_0 = 0.4 \times 10^{-4}$m$^2$ s$^{-1}$, $k_t = 1 \times 10^{10}$ s$^{-1}$, $N_{t0} = 1 \times 10^{26}$m$^{-3}$, $N_c = 1 \times 10^{27}$ m$^{-3}$, $\tau_0 = 4 \times 10^{-5}$ s and $k_{ext} = 1 \times 10^3$ m s$^{-1}$.

response $\omega_{min}$, equation 3.38 was used to calculate the value of $\zeta$. The calculations were done using $D_n$ values calculated for substrate (SE) and electrolyte (EE) side illumination. Our results shows that $\zeta$ depends on the thickness of the film and the illumination side in the DSSCs as also reported by Jennings *et al.* [29]. Figure B.2 illustrate the dependence of $\zeta$ on the optical density of the film ($\alpha d$), where $\alpha$ is the absorption coefficient and $d$ is the thickness of the film.

For substrate side illumination the value of $\zeta$ becomes very large for higher values of $\alpha$d, this may be because $\omega_{min}$ increases as the value of the optical density increase. For electrolyte side illumination the value of $\zeta$ becomes almost constant at higher values of $\alpha$d. This two observations for SE and EE side illumination illustrate that $\zeta$ depends on the illumination side. For the EE side illumination the same results were reported by Jennings *et al.* [29].

## B.3 IMPS analytical expression

The analytical solution to the continuity equations can be obtained for substrate and electrolyte side illumination as described by Dloczik *et al.* For the substrate and electrolyte side illumination and diffusion controlled electron collection, the normalized

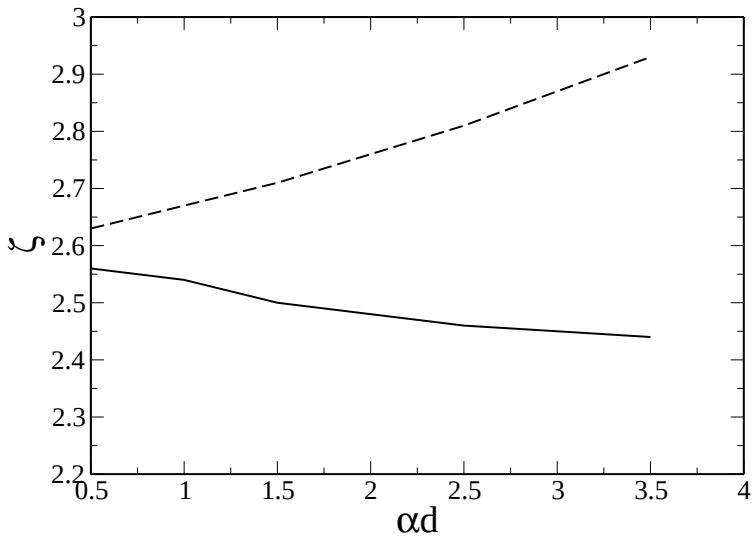


Figure B.2: Numerical factor $\zeta$ calculated for different values of the optical density ($\alpha$d), for substrate (dashed line) and electrolyte (solid line) side illumination, $D_n = 1.47 \times 10^{-9}$ $m^2s^{-1}$ and $D_n = 2.73 \times 10^{-9} m^2s^{-1}$ respectively, $I_0 = 1 \times 10^{20} m^2s^{-1}$.

solution is given by [60],

$$\Phi(\omega) = \frac{j_{photo}}{q\delta I_0} = \frac{\alpha}{\alpha+\gamma} \frac{\exp(\gamma d) - \exp(-\gamma d) + \frac{2\alpha \exp(-\alpha d) - \exp(-\gamma d)}{\gamma - \alpha}}{\exp(\gamma d) + \exp(-\gamma d)} \tag{B.1}$$

where

$$\gamma = \sqrt{\frac{1}{D_n \tau_n} + i\frac{\omega}{D_n}} \tag{B.2}$$

and the electrolyte

$$\Phi(\omega) = \frac{j_{photo}}{q\delta I_0} = \frac{\alpha}{\alpha+\gamma} \frac{\exp((\gamma-\alpha)d) - \exp -((\alpha+\gamma)d) + \frac{2\alpha \exp((\gamma-\alpha)d) - \exp(-\gamma d)}{\gamma - \alpha}}{\exp(\gamma d) + \exp(-\gamma d)} \tag{B.3}$$

where $\alpha$ is the absorption coefficient, $D_n$ is the effective diffusion coefficient, $\tau_n$ is the effective electron life time, $j_{photo}$ is the photocurrent density, $I_0$ is the illumination intensity, q is the electron charge and d is the film thickness.

### B.3.1 Attenuation

As discussed on the chapter under comparison to the experimental results, there is a deviation between the IMPS numerical solution and experimental results. At higher frequency the experimental IMPS response are affected by the attenuation, which is related to the resistance (R) and capacitance (C) of the solar cell electrode [67, 77, 81, 82, 122]. To obtain the attenuation responses the IMPS response ($\Phi(\omega)$) is multiplied by the complex attenuation function

$$A(\omega) = \frac{1}{1 + i\omega RC} \tag{B.4}$$

where R is the series resistance and C is the capacitance of the electrode. It have been found that under short circuit conditions, R and C are due to the $SnO_2/TiO_2$ interface.